

University of Nevada

Reno

Seismic Refraction Surveys of Alluvium-Filled Washes,  
Yucca Mountain, Nevada

A thesis submitted in partial fulfillment of the requirements  
for the degree of Master of Science

by

Carolyn Ruth Kneibler

August 1985

The thesis of Carolyn Ruth Kneibler is approved:

\_\_\_\_\_  
Thesis Advisor

\_\_\_\_\_  
Department Chairman

\_\_\_\_\_  
Dean, Graduate School

University of Nevada

Reno

August 1985

## ACKNOWLEDGMENTS

The author thanks the individuals who comprise the U.S. Geological Survey, Nuclear Hydrology Program, and the members of her thesis committee, Dr. John Bird, Dr. Clinton Case, and Dr. Jonathan Davis, for their academic, professional, and personal support. Special appreciation is extended to Dr. Dale Hammermeister who, as U.S. Geological Survey supervisor, initiated this project and generously gave daily guidance and assistance. Special thanks are extended to Dr. John Bird who provided academic counseling and thesis support. The author wishes to thank Messrs. Hans Ackerman, Peter Haeni, and James Scott for their technical advise. Finally, recognition and much gratitude is due to Mr. Eric Eshom, formerly of Fenix & Scisson, Inc., who was the "survey crew." His good humor, persistence, and quality work were always over and above that required. His work greatly contributed to the success of this project, and very special thanks are extended.

## ABSTRACT

Seismic refraction surveys were conducted in washes near Yucca Mountain, Nevada, to determine if depths to the interface between unsaturated alluvium and unsaturated bedrock could be obtained. Alluvial deposits consisted of intermixed and interbedded silt, sand, gravel, and boulders. The bedrock refractor was a moderately to densely welded ash-flow tuff. Degree of welding and fracture density varied. Borehole data from which depths to bedrock were determined directly were compatible with depths estimated from seismic data. Analysis of seismic data from 11 locations in three washes indicated that the thickness of alluvium ranged from 3.3 to 51.9 feet. Seismic velocities ranged from 1,251 to 3,876 feet per second in the alluvial deposits, with velocities less than 2,000 feet per second corresponding to surface layers. Seismic velocities in the bedrock ranged from 4,138 to 8,836 feet per second and could be attributed to differences in the degree of weathering, fracturing, and(or) welding.

## CONTENTS

	Page
Abstract.....	iii
→ Introduction.....	1
Seismic refraction theory.....	4
Fundamentals of seismic refraction theory.....	4
Seismic wave types.....	8
Seismic wave paths.....	10
Seismic wave velocities in geologic media.....	12
Interpretation of seismic refraction data.....	14
First arrivals and time-distance graphs.....	14
Interpretation methods.....	17
Critical distance method.....	19
Delay time method.....	25
SIPT seismic refraction interpretation model.....	32
Errors in seismic data interpretation.....	34
Hidden layers.....	34
Velocity inversion.....	35
Progressive increase in velocity.....	37
Types and characteristics of seismic sources.....	37
Explosives.....	38
Weight drop.....	38
Sledgehammer.....	40
Signal enhancement seismograph with respect to energy source.....	41
→ Study area.....	41
Geographic and geologic setting.....	41
Local study areas.....	47
→ Previous work.....	50
Sledgehammer seismic refraction method.....	50
Shallow seismic refraction surveys in hydrologic investigations.....	51
Seismic studies in the Yucca Mountain area.....	53
→ Materials and methods.....	58
Seismic refraction survey equipment.....	58
Seismograph.....	58
Cables and geophones.....	59
Seismic energy source.....	61
Miscellaneous equipment.....	61
Field vehicle and survey crew.....	61
Equipment setup.....	62
Geophone cable and geophones.....	62
Seismograph.....	63
Preliminary survey.....	63
Results and discussion.....	64
Pagany Wash.....	66
Qac Canyon.....	79
WT2 Wash.....	94
Summary and conclusions.....	103
References.....	107

## ILLUSTRATIONS

	Page
Figure 1. Diagram showing reflection and refraction of a ray at an interface.....	5
2. Schematic of Fermat's Principle.....	8
3. Diagram showing the four types of seismic waves.....	9
4. Diagram showing seismic ray paths from a source to a detector.....	11
5. Seismic data records showing background noise.....	15
6. Seismic data records showing first arrivals.....	16
7. Seismic line and corresponding time-distance graph.....	18
8. Time-distance graph showing intercept time and critical distance.....	22
9. Diagram of seismic line above two geologic layers.....	22
10. Schematic definition of delay time.....	28
11. Diagram of reversed seismic line.....	30
12. Diagram showing velocity reversal and corresponding time-distance graph.....	36
13. Map showing location of Yucca Mountain.....	42
14. Field subdivisions of the Tiva Canyon Member.....	44
15. Map showing location of study areas.....	46
16. Map showing location of lines surveyed by Pankratz.....	55
17. Map showing location of line surveyed by Ackerman.....	57
18. Seismic data records showing available trace forms.....	60
19. Diagram of seismic line.....	66
20. Map showing location of seismic lines in Pagany Wash.....	67
21. Time-distance graph for seismic line NDW1.....	68
22. Depth plot, seismic line NDW1, model #1.....	70
23. Depth plot, seismic line NDW1, model #2.....	70
24. Depth plot, seismic line NDW1, model #3.....	71
25. Time-distance graph for seismic line NDW3.....	73
26. Depth plot, seismic line NDW3.....	73
27. Time-distance graph for seismic line NDW2.....	77
28. Depth plot, seismic line NDW2.....	77
29. Map showing location of seismic line in Qac Canyon.....	80
30. Time-distance graph for seismic line Qac14.....	81
31. Depth plot, seismic line Qac14.....	81
32. Time-distance graph for seismic line Qac15.....	83
33. Depth plot, seismic line Qac15.....	85
34. Time-distance graph for seismic lines Qac1 and Qac40.....	87
35. Depth plot, seismic lines Qac1 and Qac40.....	89
36. Time-distance graph for seismic line Qac2.....	90
37. Depth plot, seismic line Qac2.....	92
38. Time-distance graph for seismic line Qac10.....	93
39. Depth plot, seismic line Qac10.....	93
40. Map showing location of seismic line in WT2 Wash.....	95
41. Time-distance graph for seismic line WT2X.....	96
42. Depth plot, seismic line WT2X.....	98
43. Time-distance graph for seismic line WT2STH.....	99
44. Depth plot, seismic line WT2STH.....	101
45. Histogram of observed velocities.....	104

## TABLES

Page

Table 1.	Reported velocity values for geologic materials similar to those encountered in the study areas.....	13
2.	Velocities obtained from seismic line NDW1.....	69
3.	Seismic depths beneath line NDW1.....	72
4.	Seismic velocities and depths beneath line NDW3.....	74
5.	Seismic velocities and depths beneath NDW1 and NDW3.....	75
6.	Seismic velocities and depths beneath line NDW2.....	78
7.	Seismic velocities and depths beneath line Qac14.....	82
8.	Seismic velocities and depths beneath line Qac15.....	84
9.	Seismic velocities and depths beneath lines Qac1 and Qac40.....	88
10.	Seismic velocities and depths beneath line Qac2.....	91
11.	Seismic velocities and depths beneath line Qac10.....	94
12.	Seismic velocities and depths beneath line WTX2X.....	97
13.	Seismic velocities and depths beneath line WT25TH.....	100

## CONVERSION FACTORS

<u>Multiply</u>	<u>By</u>	<u>To obtain</u>
inch (in)	25.40	millimeter (mm)
foot (ft)	0.3048	meter (m)
foot <sup>3</sup> (ft <sup>3</sup> )	0.02832	meter <sup>3</sup> (m <sup>3</sup> )
mile (mi)	1.609	kilometer (km)
acre	4,047	square meter (m <sup>2</sup> )
pound (lb)	0.4536	kilogram (kg)

## INTRODUCTION

The U.S. Geological Survey is conducting onsite investigations to characterize the hydrology of the unsaturated zone at Yucca Mountain, Nevada. Knowledge of spatial and temporal distribution of infiltration into the upper part of the unsaturated zone is needed to help evaluate the suitability of the Yucca Mountain site as a potential high-level radioactive-waste repository. Unsaturated alluvial deposits underlie about 35 percent of the Yucca Mountain area; these deposits occur along washes that form the major drainage system at the site. Understanding of the three-dimensional configuration of the alluvial deposits is needed to help guide drilling programs, and to enable extrapolation of infiltration and recharge data throughout the site. These studies are a part of the Nevada Nuclear Waste Storage Investigations project of the U.S. Department of Energy (Interagency Agreement DE-AI08-78ET44802).

To obtain information on present infiltration and recharge in the shallow unsaturated zone, a drilling program for neutron-access holes has been established. (Hammermeister, D., U.S. Geological Survey, written commun., 1984). The majority of access holes are located in alluvium-filled washes; drilled to a depth sufficient to penetrate five feet of bedrock. As each hole is drilled, cuttings and drive cores are collected at specified depth intervals and later analyzed for lithology, density, porosity, and moisture content. Upon completion of each hole, neutron moisture logs are run, followed by a continuing program of density, porosity, and moisture logging. A limited number of boreholes can be drilled in the relatively large number of washes at Yucca Moun-

tain, therefore, the majority of holes are located in easily accessible, well-defined geohydrologic environments. Detailed recharge data from these washes will be used to make recharge estimates in similar washes that contain fewer, or in some cases no boreholes. One of the first steps in identifying similar washes and(or) portions of washes is to determine alluvium thickness and layering sequences. [Seismic surveys are an indirect method of obtaining such information. The high cost of geophysical services and the uncertain results from preliminary large scale work influenced the decision to conduct shallow seismic refraction surveys of the washes at Yucca Mountain.]

The seismic refraction method consists of measuring travel times of compressional waves to known points along the ground surface. Compressional waves generated by an impulsive energy source are detected, amplified, and then recorded by equipment that is collectively referred to as a seismograph system. The instant of energy impulse, or zero time, is recorded on the seismic record. Raw data consists of travel times and distances between shotpoints and geophones. This time-distance information is graphically and mathematically manipulated to derive velocity variations with depth. All measurements are made at the ground surface, and subsurface structure is inferred from interpretation based on the laws of energy propagation. Seismic surveys are commonly used in hydrologic investigations to obtain information such as depth to ground water, location of buried stream channels, and thickness of unconsolidated overburden. In areas with a shallow water table, the interface between saturated and unsaturated unconsolidated materials is often the first horizon of interest. Although individual stratified

layers of unconsolidated material may not be distinguishable within the unsaturated overburden, the depth to saturated sediments and bedrock is usually definable. In this study, depth of interest is the boundary between unsaturated alluvium and unsaturated bedrock. The velocity contrast between these units is variable and often low because of fractures and weathering in the bedrock unit.

A preliminary literature review suggested that the refraction method of seismic surveying should be used rather than the seismic reflection method. Reflection methods require prior knowledge of seismic velocities and velocity distributions. This information is not well known in the study areas. Further, a sledgehammer would be used as the source for seismic waves for the following reasons: (1) Shallow depth of investigation; (2) lack of explosives training for personnel; and (3) difficulties in augering the surface sediments of the study area for emplacement of explosives. (Hammermeister, D., written commun., 1984).

The objectives of this study were: (1) To determine if shallow seismic refraction surveys could be used to determine thicknesses of alluvium by performing surveys near boreholes that determined thicknesses directly; (2) if the seismic refraction method proved to be successful, perform preliminary surveys in washes that did not contain boreholes; and (3) to define conditions under which shallow seismic surveys could be successfully carried out in washes at Yucca Mountain.

## SEISMIC REFRACTION THEORY

Fundamentals of Seismic Refraction Theory

The principles of seismic refraction surveying are based on the knowledge that elastic waves travel at particular, and in some cases, well defined velocities through different materials. In general, the more dense the material, the faster the wave travels through the medium. Propagation of seismic energy through subsurface layers is described by the laws of physical optics. The refraction that a light ray or seismic wave undergoes when passing from one material into another depends upon the ratio of the transmission velocities of the two media.

Physical laws that apply to seismic refraction surveys are Huygen's Principle, Snell's Law, and Fermat's Principle. Huygen's Principle states that every point on a wave front is the source of a new wave that travels out from that point in spherical shells (Halliday and Resnick, 1974, p. 672). When the wave generated according to Huygen's Principle strikes an interface at a critical angle, part of the wave is reflected back into the first medium and part is refracted into the second medium (fig. 1). The direction of the reflected ray is governed by the law of reflection which states that the angle of reflection is equal to the angle of incidence and the reflected and incident rays lie in the same plane (Mason and Berry, 1968, p. 106). The relationship between the paths of the incident and refracted rays is known as the Law of Refraction and as Snell's Law. It states that the ratio of the sine of the angle of incidence,  $i$ , to the sine of the angle of refraction,  $r$ , is

constant, that is:

$$\frac{\sin i}{\sin r} = n ; \quad (1)$$

where  $n$  is the index of refraction (Mason and Berry, 1968, p. 106). For optical purposes, the value of  $n$  is the ratio of the velocity of light in air,  $V$ , to the velocity of light in solid,  $v$ :

$$n = \frac{V}{v} . \quad (2)$$

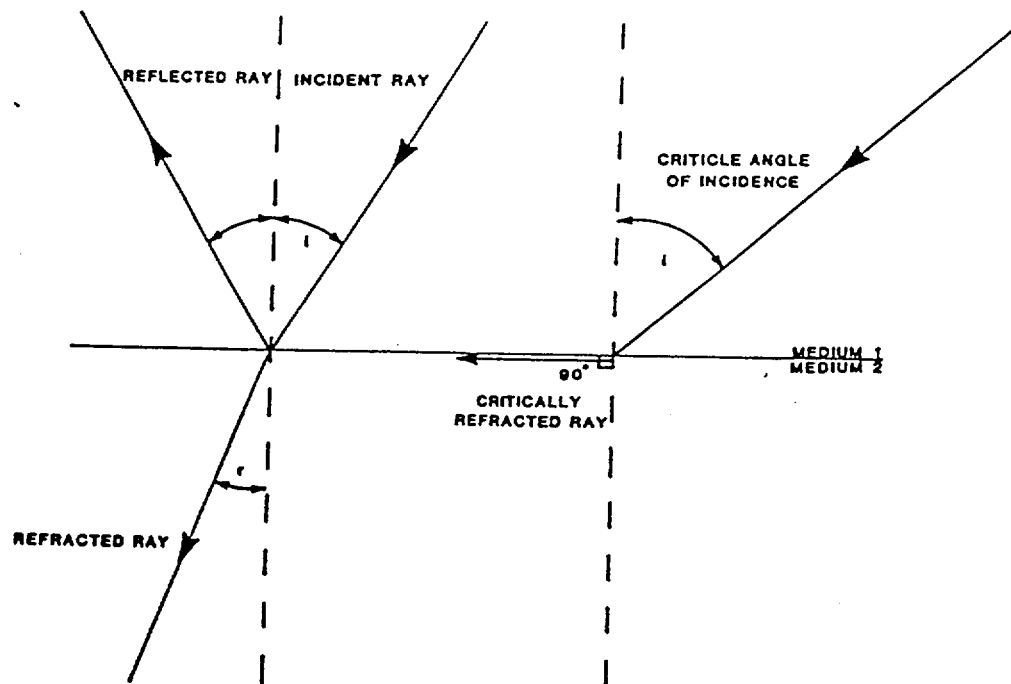


Figure 1.--Reflection and refraction of a ray transmitted across the boundary between two media (modified from Redpath, 1973).

In seismic studies, refraction occurs at the interface between two subsurface stratigraphic units. The value of  $n$  in equation (1) is replaced with the ratio between the elastic wave velocities in the two units,

$$\frac{\sin i}{\sin r} = \frac{V_1}{V_2} ; \quad (3)$$

where  $V_1$  is the velocity of the upper layer,  $V_2$  is the velocity of the lower layer, and  $V_2 > V_1$ . For the case where  $V_1 > V_2$ , the incident ray is deflected downward toward the vertical and will not return to the surface until it has encountered a layer with a velocity greater than any velocity encountered on its downward travel.

The critical angle of incidence is defined as the angle of the incident ray that results in a refracted angle equal to 90 degrees (Jakosky, 1950,p. 665). At angles less than the critical angle of incidence, almost all compressional energy is refracted into the higher velocity medium. When the critical angle is exceeded, energy is almost totally reflected. When  $r$  is 90 degrees,  $\sin r$  is 1, therefore, the critical angle of incidence, is:

$$\sin i = \frac{V_1}{V_2} . \quad (4)$$

Reflection and refraction of a ray or seismic wave follow Fermat's Principle of least time, which states that the travel path between two points is the path of minimum time (Gary and others, 1974, p. 257). The travel time from point B to D in figure 2 is:

$$\begin{aligned}
 T &= \frac{BO}{V_1} + \frac{OD}{V_2} \\
 &= \frac{\sqrt{Y_1^2 + X^2}}{V_1} + \frac{\sqrt{Y_2^2 + (L-X)^2}}{V_2} .
 \end{aligned} \tag{5}$$

If this time is a minimum, then  $dT/dX = 0$  and

$$\begin{aligned}
 0 &= \frac{X}{V_1 \sqrt{Y_1^2 + X^2}} - \frac{(L-X)}{V_2 \sqrt{Y_2^2 + (L-X)^2}} \\
 &= \frac{\sin i}{V_1} - \frac{\sin r}{V_2} .
 \end{aligned} \tag{6}$$

Therefore,

$$\frac{\sin i}{\sin r} = \frac{V_1}{V_2} = \text{constant} , \tag{7}$$

which also illustrates Snell's Law and evaluates the index of refraction as the ratio of the velocities in the two media. For other wave paths, the travel time predicted to be a minimum may be a maximum or a stationary value (Martin and others, 1967, p. 74).

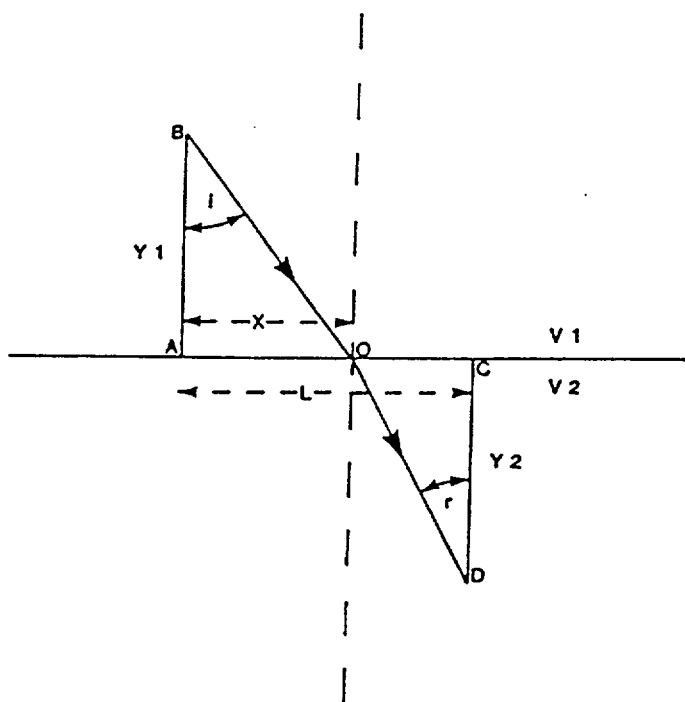


Figure 2.--Schematic illustrating Fermat's Principle (modified from Martin and others, 1967).

### Seismic Wave Types

Four types of elastic waves may be transmitted through a homogeneous, isotropic, elastic solid. They are compressional (P), shear (S), Rayleigh, and Love waves (fig. 3). Only P, S, and Rayleigh waves can be observed in shallow seismology. Each of these waves causes a slight, momentary, vertical displacement of material as it passes through the earth.

P and S waves are body waves that are transmitted through the interior of a solid. They return to the surface by reflection or refraction. P waves cause compressional motion that is parallel to the

direction in which the wave is traveling. S waves cause transverse motion that is perpendicular to the direction in which the wave is traveling. Rayleigh and Love waves are near surface waves whose amplitude dies out rapidly with depth. Rayleigh waves are elliptical in motion and retrograde with respect to the direction of propagation. Part of the motion is parallel to the surface of the earth along which the wave is traveling and part is perpendicular to the surface. Love waves are generated when there is a surface layer with an elastic constant different from that of the rest of the solid (Dobrin, 1976, p. 38-39; Zohdy and others, 1980, p. 68). Wave motion is horizontal and transverse and therefore, is not recorded by geophones that are designed to respond to vertical ground motion only.

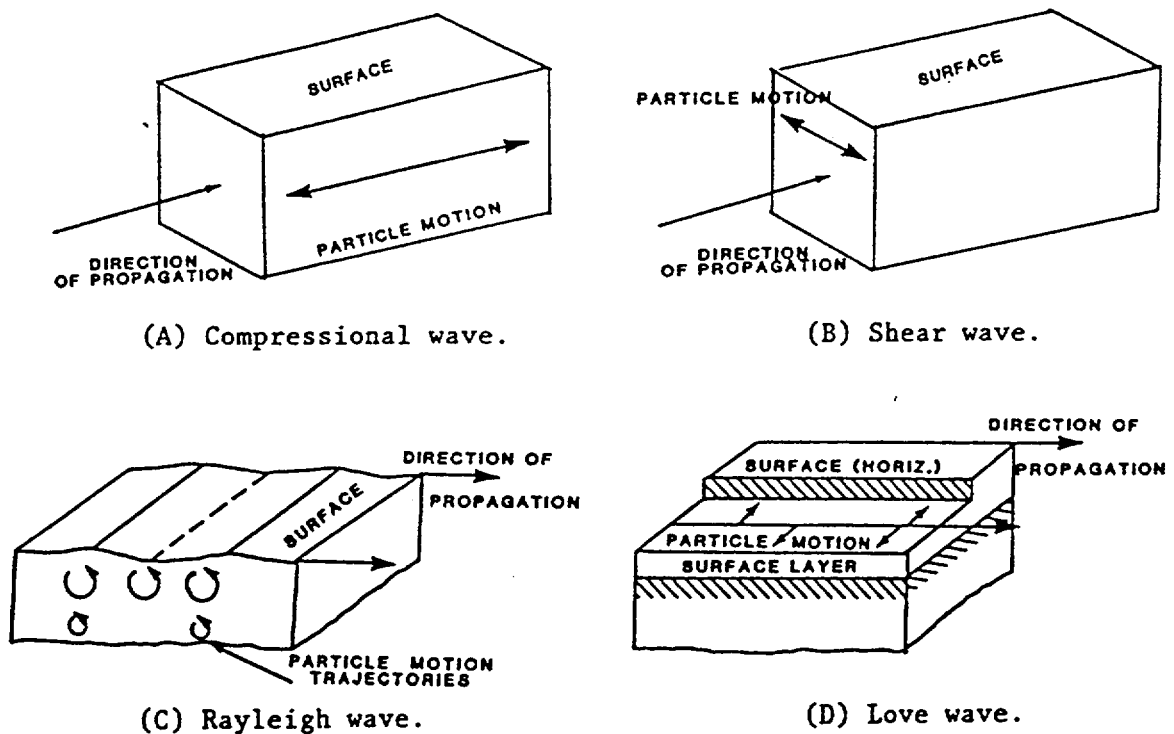


Figure 3.--Seismic wave types and particle displacements during passage through a medium (modified from Mooney, 1977 and Dobrin, 1976).

Each of the three wave types recorded by geophones travels at a characteristic velocity. P waves travel at the greatest velocity. The S wave travels at approximately one-half of the P wave velocity ( $S = 0.577P$  for well-consolidated rock;  $S = 0.45P$  in soils) (Mooney, 1977, p. 3-3). Rayleigh waves travel at approximately 0.9 the velocity of the S wave (ibid).

In shallow seismology, nearly all work is based on the P wave because of two factors. First, the distances involved are very short and the P and S waves arrive so closely together that the S wave is lost in the train of motion following the first arrival of the P wave. Secondly, because the vertical component of vibration is sensed by geophones, the shear component of the waves is greatly minimized (Jakosky, 1957, p. 651). All further discussion of elastic waves and seismic waveforms will be concerned with compressional (P) waves only.

#### Seismic Wave Paths

A record of seismic waveforms shows ground motion at a geophone (or series of geophones) as a function of time. A complete seismic waveform may show several distinct arrivals. These arrivals are produced not only by the different wave types but also by different wave paths through the earth.

Seismic waves generated from a point source at the surface of a two layer medium are shown in figure 4. The paths are illustrated as four

rays and are: (1) The direct ray that follows a horizontal path from the source point to the detector; (2) the totally reflected ray that strikes the boundary between two layers at an angle greater than the critical angle of incidence; (3) a ray that strikes the boundary at exactly the critical angle of incidence, part of the energy being reflected and part of it being refracted along the interface; and (4) the refracted ray that strikes the interface at an angle less than the critical angle of incidence.

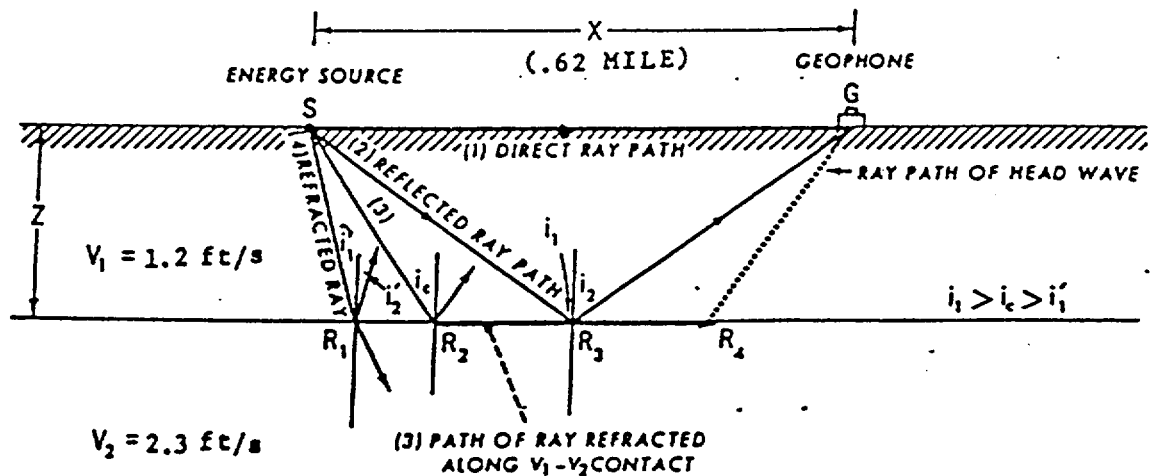


Figure 4.--Ray-path diagram of seismic energy generated at source S and detected at geophone G (modified from Zohdy and others, 1974).

First arrivals on a seismic data record may be produced by either the direct or the refracted ray. The direct ray travels the shortest distance from shotpoint to geophone; first arrivals at the geophones closest to the shotpoint are often the direct ray. The refracted ray travels through the higher velocity medium and therefore arrives at the geophones before the reflected portion of the wave that must travel through the lower velocity medium.

### Seismic Wave Velocities in Geologic Media

Seismic wave velocity in a geologic medium is dependent on density and factors that affect density such as mineralogical composition, grain size, lithification, direction with respect to bedding or foliation, fluid content, pressure, and temperature (Grant and West, 1965; Clark, 1966). Velocity tables for geologic materials report values based on material type, age, depth of burial, and degree of water saturation. Reported values are most often obtained from laboratory measurements of core samples. Example values are shown in table 1. Velocity tables are used to obtain a general range of velocities that may be expected in a particular study area. These ranges are often wide and field measurements are usually necessary to obtain more specific information on velocities. Preliminary velocity information can also be obtained from borehole acoustic-velocity logs. These logs are run in a water or mud-filled borehole however, and information regarding seismic velocities in the unsaturated zone cannot be obtained from dry-drilled boreholes.

Table 1.--Reported velocity values for geologic materials similar to those found in the Yucca Mountain area, Nevada Test Site  
[ft/s, foot per second]

Material	Velocity in ft/s	Reference
Water (fresh)	4,800	(Mercer, 1970)
Water (saline)	4,860	(ibid.)
Volcanic tuff		
New Zealand	7,090	(Clark, 1966)
Weathered and fractured rock	1,500 to 10,000	(Redpath, 1973)
Alluvium, near surface	1,640 to 6,560	(Clark, 1966)
Weathered surface material	1,000 to 2,000	(Redpath, 1973)
Gravel, rubble, or sand (dry)	1,500 to 3,000	(ibid.)
Quaternary sediments		
various degrees of consolidation	1,000 to 7,500	(Jakosky, 1950)
Tertiary sediments		
consolidated	5,000 to 14,000	(ibid.)

\*  
Seismic wave velocity in a porous media is effected by the amount of pore or void space and the type of fluid(s) that occupy the space. Gas-filled pores decrease velocities; liquid-filled pores increase velocity. Low porosity igneous rocks have the highest velocities for geologic materials: often, the velocity is greater than 16,000 ft/s. Since porosity tends to decrease with depth because of compression, porosity effects are most pronounced in upper geologic units. Laboratory measurements on sandstone cores indicate that the velocity of compressional waves is roughly inversely proportional to porosity over a broad range (Wyllie and others, 1958).

In general, velocity values are greater for: mafic igneous rocks than felsic igneous rocks; igneous rocks than sedimentary rocks; consolidated sediments than unconsolidated sediments; water-saturated unconsolidated sediments than dry unconsolidated sediments; wet soils

than dry soils; carbonates than sandstones; sandstones than shales; solid rocks than fractured rocks; unweathered rocks than weathered rocks; dense rocks than light rocks; and finally, older rocks than younger rocks (Mooney, 1977).

### Interpretation of Seismic Refraction Data

#### First Arrivals and Time-Distance Graphs

Interpretation of seismic refraction data depends on the precise identification of first arrivals on a seismic data record. The "first arrival" or "first break" is defined as the first noticeable departure of the seismic pulse from a background signal (Hatherly, 1982, p. 1431). There are several problems associated with the selection of first arrivals: (1) Background noise may over-shadow the early part of the seismic signal and delay its appearance (fig. 5A and 5B); (2) amplitudes of both the signal and noise vary from trace to trace, and a phase picked as a first arrival on one trace may not be identical to the phase picked on another; and (3) the recording equipment may not be able to detect weak signals and therefore first arrivals may not be recorded.

The first arrival of a P wave is a small amplitude, sharp break, upward or downward on the seismic record. First waves recorded in figure 6A are Rayleigh waves and later arriving P waves. These signals have large amplitudes and are easily sensed by geophones. A record with distinct, downward breaking, first arrivals is shown as figure 6B.

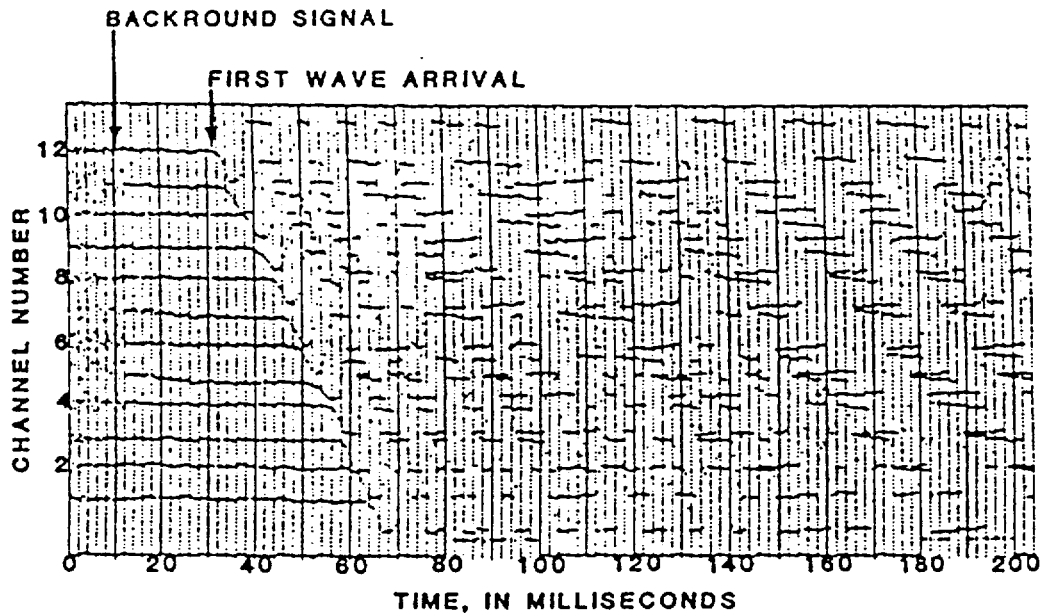


Figure 5A.--ES-1210 seismic data record with little background noise.

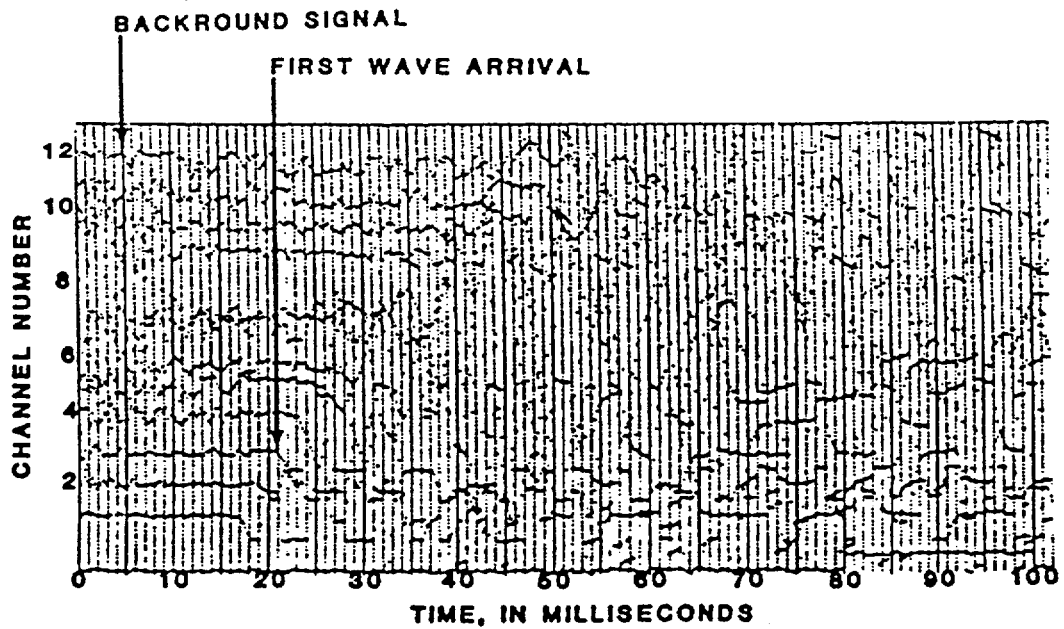


Figure 5B.--ES-1210 seismic data record with background noise.

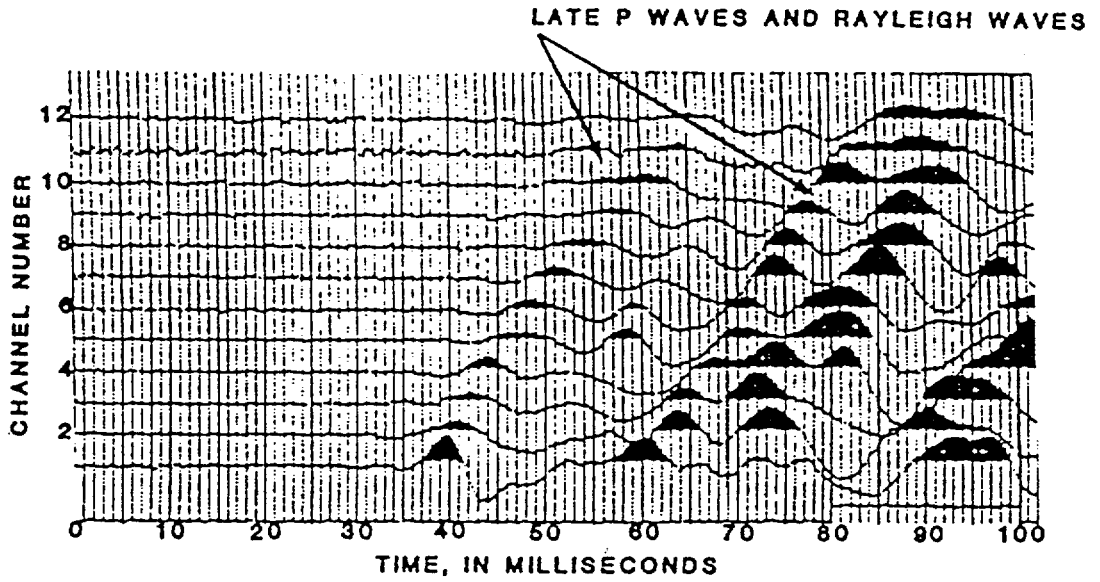


Figure 6A.-- ES-1210 seismic data record showing late wave arrivals.

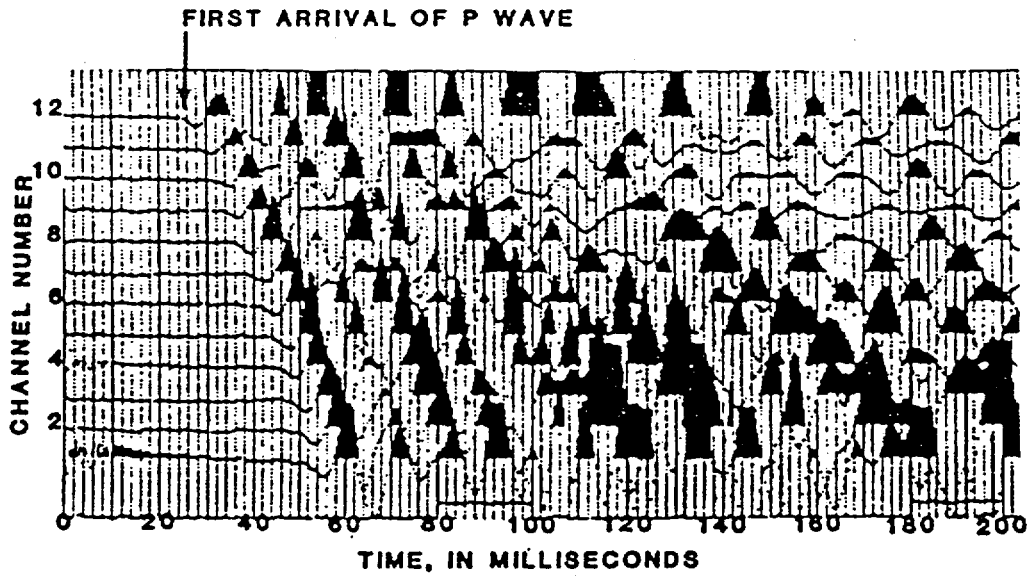


Figure 6B.--ES-1210 seismic data record showing first arrivals.

Arrival times are plotted on a graph as milliseconds verses distance (fig. 7). The distance axis represents geophone locations as well as the closest offset shotpoints that are usually equal to the geophone spacing. A reference point is selected. Zero on the x-axis represents geophone #1 in this report. All shotpoints for a particular line are plotted on a single graph, each shotpoint having its own curve. Every point for a particular shotpoint is connected. Curves generated by different shotpoints are then compared. Existence of parallel line segments generated from different shotpoints indicates arrivals from the same refractor. The number of line segments with different slopes indicates the probable number of geologic layers present beneath the seismic line. The slope of each straight-line segment on the time-distance graph is in units of time per distance. The inverse slope is in units of distance per time and represents the velocity of the medium through which the compressional wave travelled.

#### Interpretation Methods

Two methods of seismic data interpretation were used in this study. For a discussion of the other interpretation methods that are available, the reader is referred to Musgrave (1967) and Dobrin (1976).

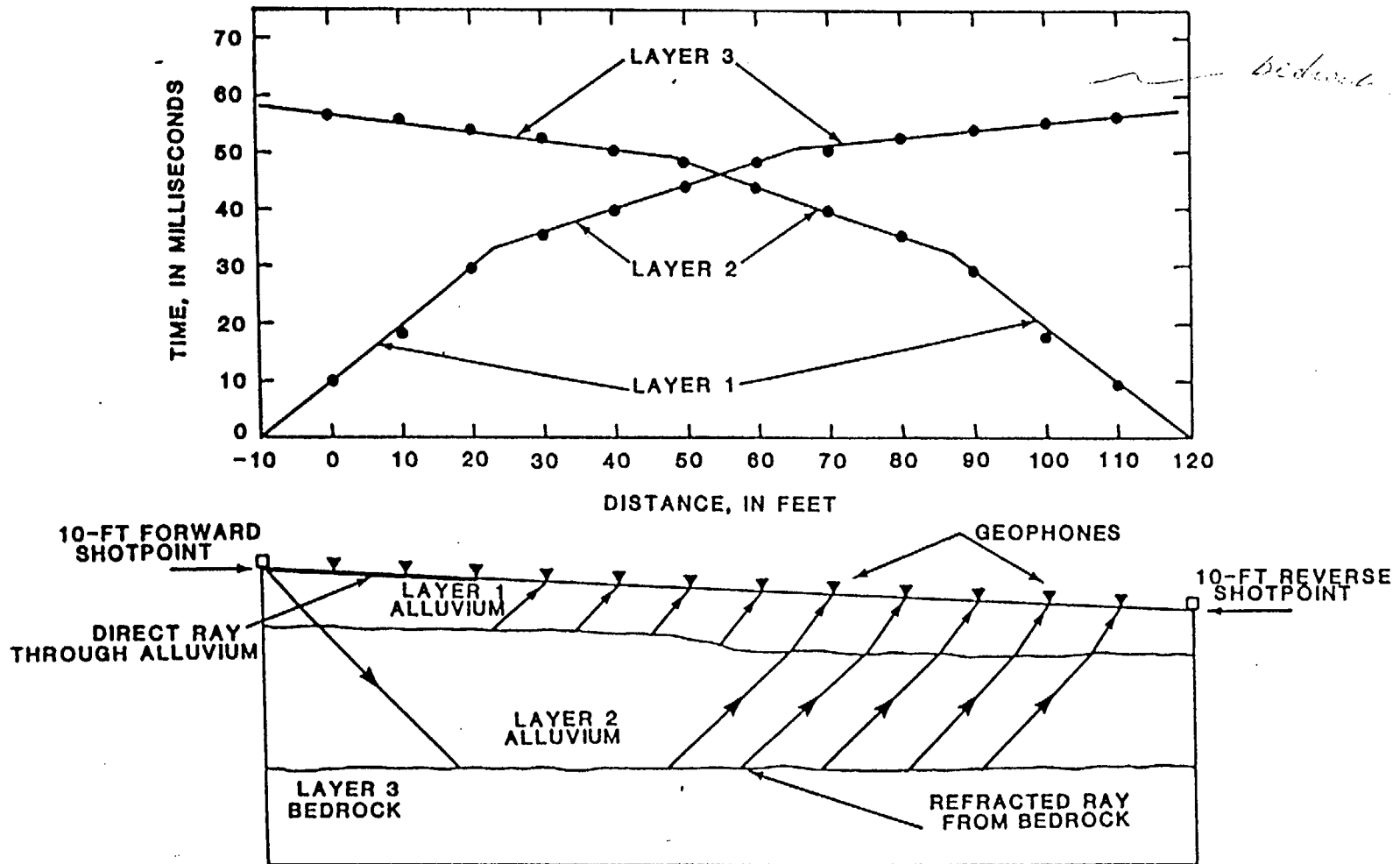


Figure 7.--Time-distance graph and corresponding seismic line

(modified from Redpath, 1973).

### Critical distance method

The critical distance method of data interpretation was used in the field to determine the arrangement of shotpoints and geophones required to record first arrivals from bedrock. Velocity values were calculated for a single shotpoint and the resultant depths represented the average depth to the refracting layer beneath the middle of the seismic line (Mooney, 1977).

The simplest case for seismic data interpretation is that of two geologic layers with plane and parallel boundaries. Compressional waves are detected by a series of geophones laid out in a straight line along the ground surface. Arrival times of the wave are plotted against corresponding shotpoint-to-detector distances (fig. 8). The first few arrival times are those of direct arrivals through the first layer. The slope of the line through these points is the reciprocal of the velocity for that layer, i.e.  $1/V_1$ . A line drawn through these points will pass through the origin of the time-distance graph. At some distance from the shotpoint, a distance called the "critical distance" exists. At this point, the refracted wave arrives at the same time as the direct wave. Refracted arrivals that are recorded beyond the critical distance will plot along a line with a slope of  $1/V_2$ . A line drawn through these refracted arrivals will project back to the time (Y) axis and intercept it at a time called the intercept time. The critical distance,  $X_c$ , is the breakpoint in the slope between the two line segments. Both intercept time and critical distance are dependent upon the velocity of each

of the layers and thickness of layer #1, and may therefore be used to determine the depth to the top of layer #2.

The total travel time,  $T$ , for a compressional wave along the path ABCD in figure 9 is:

$$T = T_{AB} + T_{BC} + T_{CD} , \quad (8)$$

where  $T_{AB}$  is the travel time from A to B,  $T_{BC}$  is the travel time from B to C, and  $T_{CD}$  is the travel time from C to D.

From figure 9:

$$AB = CD = \frac{Z_1}{\cos i} ; \quad (9)$$

and

$$BC = X - 2Z_1 \tan i ; \quad (10)$$

where  $Z_1$  is the thickness of layer 1 and  $i$  is the critical angle of incidence.

Substituting equations (9) and (10) into equation (8):

$$\begin{aligned} T &= \frac{AB + CD}{V_1} + \frac{BC}{V_2} \\ &= \frac{2Z_1}{V_1 \cos i} + \frac{X - 2Z_1 \tan i}{V_2} \\ &= 2Z_1 \left( \frac{1}{V_1 \cos i} - \frac{\sin i}{V_2 \cos i} \right) + \frac{X}{V_2} \\ &= 2Z_1 \left( \frac{V_2 - V_1 \sin i}{V_1 V_2 \cos i} \right) + \frac{X}{V_2}. \end{aligned} \tag{11}$$

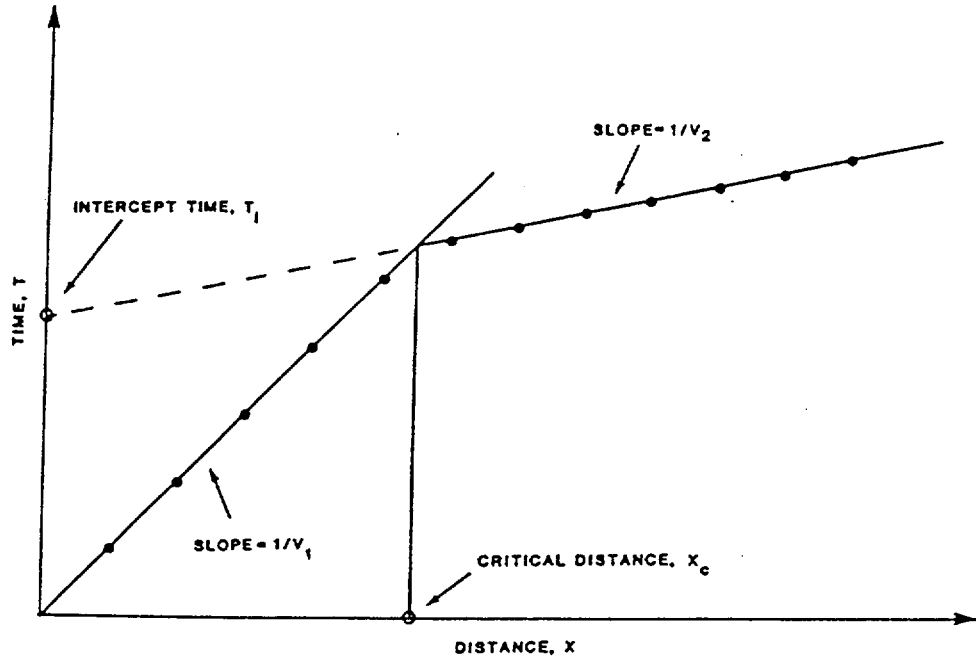


Figure 8.--Time-distance graph illustrating intercept time and critical distance.

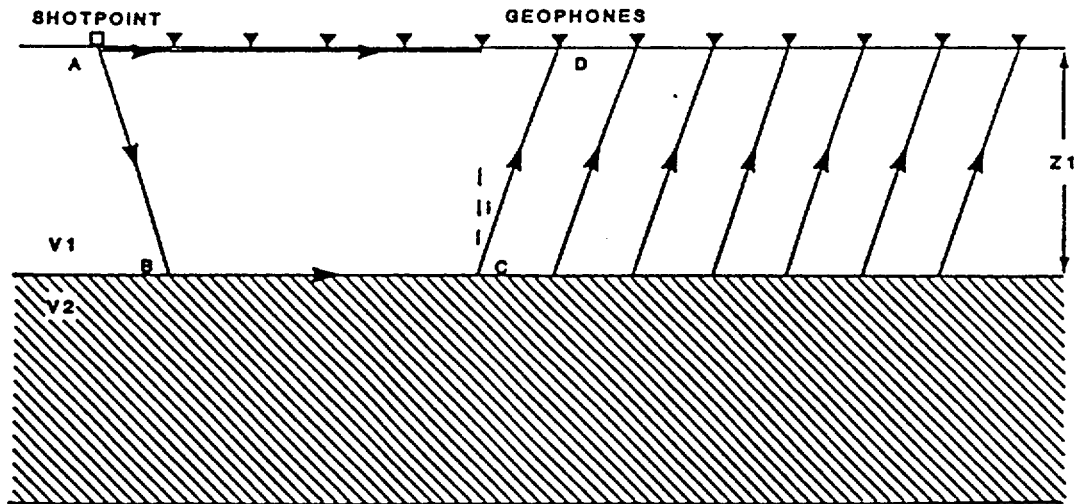


Figure 9.--Refraction line above two layers with plane, parallel boundaries (modified from Redpath, 1973).

From Snell's Law, the critical angle of incidence,  $i$ , is:

$$\sin i = \frac{V_1}{V_2},$$

therefore,

$$i = \sin^{-1} \frac{V_1}{V_2}. \quad (12)$$

Substituting equation (12) into equation (11):

$$\begin{aligned} T &= 2Z_1 V_1 \left( \frac{1/\sin i - \sin i}{V_1 V_2 \cos i} \right) + \frac{X}{V_2} \\ &= 2Z_1 V_1 \left( \frac{1 - \sin^2 i}{V_1 V_2 \cos i \sin i} \right) + \frac{X}{V_2} \\ &= 2Z_1 \left( \frac{1 - \sin^2 i}{V_2 \cos i \sin i} \right) + \frac{X}{V_2} \\ &= 2Z_1 \left( \frac{\cos i}{V_2 \sin i} \right) + \frac{X}{V_2}. \end{aligned} \quad (13)$$

Substituting  $V_1 = V_2 \sin i$  into equation (13),

$$T = 2Z_1 \left( \frac{\cos i}{V_1} \right) + \frac{X}{V_2}. \quad (14)$$

When the value of  $X$  on the time-distance graph is equal to zero,  $T$  is equal to the intercept time  $T_i$ , and equation (14) can be rewritten as:

$$T_i = 2Z_1 \left( \frac{\cos i}{V_1} \right). \quad (15)$$

Rewriting equation (15) in terms of the unknown thickness of layer 1 yields:

$$2Z_1 = \frac{T_i V_1}{\cos i} ;$$

and

$$\begin{aligned} Z_1 &= \frac{T_i V_1}{2 \cos i} \\ &= \frac{T_i V_1}{2 \cos (\sin^{-1} V_1/V_2)} . \end{aligned} \quad (16)$$

Written in terms of velocities and times, equation (16) is;

$$Z_1 = \frac{T_i}{2} \left( \frac{V_1 V_2}{\sqrt{V_2^2 - V_1^2}} \right) . \quad (17)$$

To express the depth to the top of layer 2 in terms of the critical distance, two relationships are used. The direct wave travels from the shotpoint to the geophones at a velocity of  $V_1$  such that:

$$T_1 = \frac{X}{V_1} . \quad (18)$$

Equation (14) can be written in terms of  $T_2$  as:

$$T_2 = \frac{X}{V_2} + 2Z_1 \left( \frac{\sqrt{V_2^2 - V_1^2}}{V_2 V_1} \right) . \quad (19)$$

At the critical distance,  $X_c$ ,  $T_1$  and  $T_2$  are equal, therefore:

$$\frac{X_c}{V_1} = \frac{X_c}{V_2} + \frac{2Z_1 \sqrt{V_2^2 - V_1^2}}{V_2 V_1}$$

and,

$$Z_1 = \frac{1}{2} \left( \frac{V_1 V_2 X_c}{\sqrt{V_2^2 - V_1^2}} \right) \left( \frac{1}{V_1} - \frac{1}{V_2} \right),$$

which simplifies to the equation for determining the thickness of layer 1 in terms of critical distance and two velocities;

$$Z_1 = \frac{X_c}{2} \sqrt{\frac{V_2 - V_1}{V_2 + V_1}} \quad (20)$$

This calculation is easily performed in the field with a programmable calculator.

#### Delay time method

Where boundaries between stratigraphic units are nonparallel, a plot of arrival time verses distance will produce apparent velocities for the refracting layers; velocity values will be less than the true velocity if down-dip and greater if up-dip. Use of these apparent velocities will result in erroneous depth calculations.

The delay time of a seismic wave is the difference between time actually spent traveling upward or downward through the upper layer, and the time it would have spent traveling at the refractor velocity, along the normal projection of this path on the interface (Redpath, 1973, p. 10; Dobrin, 1976, p. 314). Delay time is defined at the shotpoint and geophones. Referring to figure 10, the delay time at the geophone is defined as:

$$\begin{aligned}
 DT_G &= \frac{CD}{V_1} - \frac{CD'}{V_2} , \\
 &= \frac{Z_G}{V_1 \cos i} - \frac{Z_G \tan i}{V_2} \\
 &= Z_G \left( \frac{1}{V_1 \cos i} - \frac{\sin i}{V_2 \cos i} \right) , \tag{21}
 \end{aligned}$$

where  $DT_G$  is the delay time at the geophone and  $Z_G$  is the depth to layer 2 beneath the geophone.

From Snell's Law,

$$\sin i = \frac{V_1}{V_2} ,$$

therefore

$$V_2 = \frac{V_1}{\sin i} ,$$

and,

$$DT_G = Z_G \left( \frac{1}{V_1 \cos i} - \frac{\sin^2 i}{V_1 \cos i} \right) .$$

$$\frac{\sin i}{V_2 \cos i} = \frac{\frac{\sin i}{V_1}}{\sin i} \quad (\text{as } i)$$

Because  $\sin^2 i + \cos^2 i = 1$ ,

$$DT_G = \frac{Z_G \cos i}{V_1},$$

so that the delay time beneath the geophone is;

$$DT_G = \frac{Z_G \cos (\sin^{-1} V_1/V_2)}{V_1}. \quad (22)$$

The delay time beneath the shotpoint is obtained in a similar manner and is:

$$DT_S = \frac{Z_S \cos (\sin^{-1} V_1/V_2)}{V_1} \quad (23)$$

where  $DT_S$  is the delay time beneath the shotpoint and  $Z_S$  is the depth to layer 2 beneath the shotpoint.

Total delay time ( $DT_T$ ) is, by definition:

$$DT_T = T_t - \frac{S}{V_2}; \quad (24)$$

where  $T_t$  is the observed total travel time from shotpoint to geophone;  
 $S$  is the distance along the interface between the normal projections beneath the shotpoint and geophone calculated from the dip of the beds; and

$V_2$  is the velocity of the refracting layer (Layat, 1967).

Dip of the refractor bed must be small (less than 10 degrees) such that  $S$  is approximately equal to  $A'E$  in figure 10. With this condition, Fermat's principle is valid within the accuracy limitations of other factors (Gardner, 1967, p. 339).

Because delay time is defined at both the shotpoint and the geophone, the total delay time may be expressed as the sum of delay times at the shotpoint and at the geophone as:

$$DT_T = DT_S + DT_G \quad (\text{Dobrin, 1976, p. 313}). \quad (25)$$

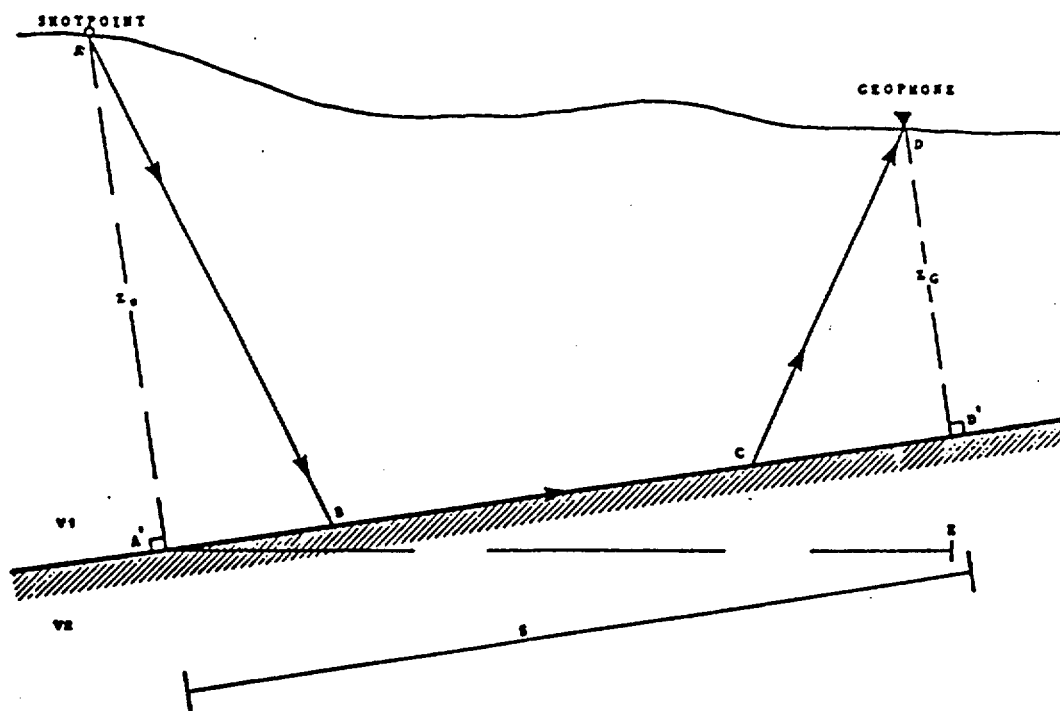


Figure 10.--Schematic definition of delay time.

By combining equations (24) and (25), an expression for delay time beneath the shotpoint or the geophone is obtained. For example:

$$DT_G = T_t - \frac{S}{V_2} - DT_S . \quad (26)$$

If depth to the refractor beneath the shotpoint and velocities of the layers are known, then  $DT_S$  can be calculated, and the only unknown value would be the delay time beneath the geophone; the arrival time from one end of the line would be sufficient to determine the delay time beneath the geophone (Redpath, 1973, p. 11). Because velocity and depth information are not often known prior to surveying an area, shotpoints at both ends of the line are required to determine true layer velocities and depths. This method of seismic surveying is known as a "reversed profile" or "reversing the line." Reversed profiles are seismic lines surveyed using common geophone locations with shotpoints recorded from opposite (reversed) directions (fig. 11). Because minimum-time travel paths are independent of direction, the total travel time ( $T_t$ ) from each shotpoint must be equal; that is,  $T_t$  from shotpoint 1 must equal  $T_t$  from shotpoint 2. A range of about three milliseconds is generally considered to be acceptable. Furthermore, the same number of velocity layers must be identifiable on the reversed time-distance graphs (Ackerman and others, 1982, p. 13).

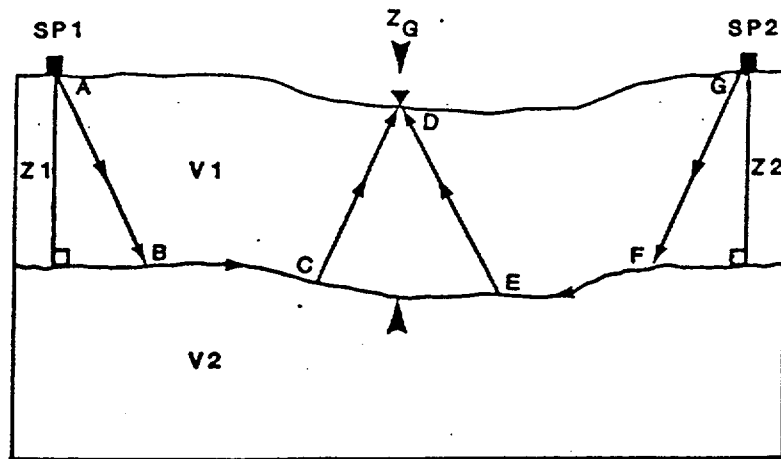
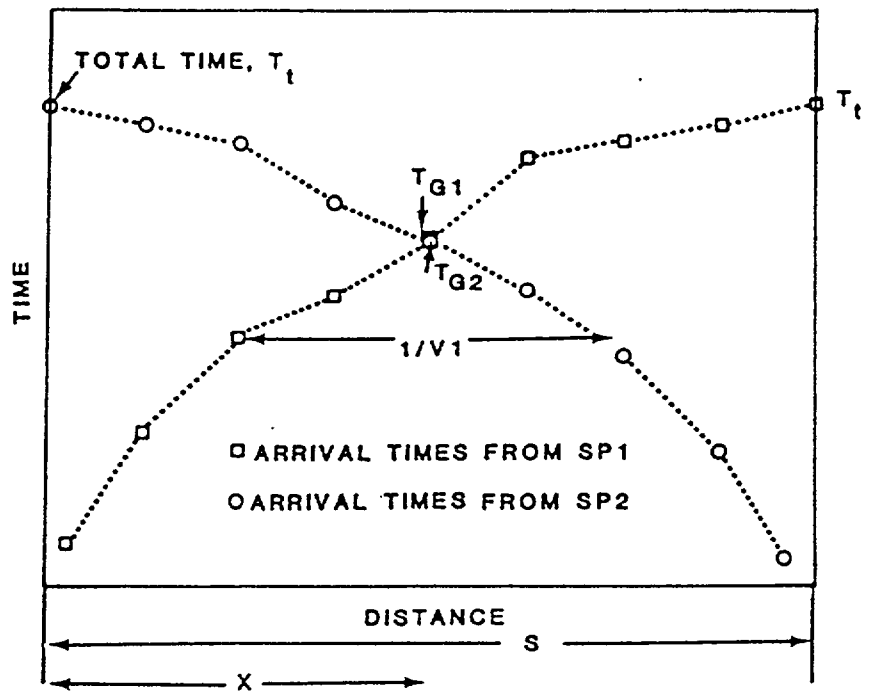


Figure 11.-- Diagram of reversed seismic line and delay-time method of depth determination (modified from Redpath, 1973).

The arrival times at one geophone of a reversed profile have been designated as  $T_{G_1}$  and  $T_{G_2}$  in figure 11. Each arrival time can be expressed in terms of component delay times by rewriting equation (26) as:

$$T_{G_1} = DT_{S_1} + DT_G + \frac{X}{V_2} ,$$

and

$$T_{G_2} = DT_{S_2} + DT_G + \frac{S - X}{V_2} ,$$

so that

$$T_{G_1} + T_{G_2} = DT_{S_1} + DT_{S_2} + 2DT_G + \frac{S}{V_2} . \quad (27)$$

In a similar manner, the total travel time can be written as:

$$T_t = DT_{S_1} + DT_{S_2} + \frac{S}{V_2} ;$$

so that

$$T_{G_1} + T_{G_2} = 2DT_G + T_t$$

and therefore,

$$DT_G = \frac{1}{2} (T_{G_1} + T_{G_2} - T_t) . \quad (28)$$

The depth to the top of the refractor beneath the geophone may then be calculated by rewriting equation (22) as,

$$Z_G = \frac{DT_G V_1}{\cos (\sin^{-1} V_1/V_2)} . \quad (29)$$

#### SIPT seismic data interpretation model

Seismic data were interpreted with the SIPT (Seismic Interpretation Program Timeshare) Fortran-IV computer program developed by J. H. Scott (Scott and others, 1972, Scott, J. H., 1973, Scott, J. H., 1977). The program was revised on 22 February 1984 for the Prime 850 computer and updated on 25 April 1984. The program was run on a Prime 850 and Prime 9950 computer. A batch-mode program, SIPB, is also available (Scott, J. H., 1977). For seismic refraction spreads of great length and depth of investigation, the reader is referred to Ackerman and others (1982). This computer program will account for horizontal (lateral velocity variations).

A data input file is created for each seismic spread. Data may be formatted in card or free field format. Shotpoint and geophone locations, travel times, and layer designations are supplied as input. Layer velocities may be calculated from time-distance graphs and entered as input data or they may be calculated by the program. A first approximation of each refraction horizon is obtained by a computer adaptation of the delay time method. The approximation is then

tested and improved through use of a ray-tracing procedure in which computed ray travel times are compared against field-measured travel times. The model is then adjusted in an iterative manner so as to minimize discrepancies between computed and measured travel times. Output of the program is presented in tables and as a plotted cross section that represents velocity layering beneath a seismic spread.

\*

Assumptions applied to the SIPT model are: (1) Layers are continuous and extend from one end of the refraction spread to the other; (2) layer velocity increases with layer depth; (3) horizontal velocity is equal to or greater than vertical velocity for any given layer; (4) although vertical and horizontal velocity for a given layer may be different from one another, both velocities are constant from one end of a spread to the other; (5) refracted rays represent minimum-time travel paths; and (6) the deepest layer extends to an infinite depth.

Computer program data requirements are: (1) The program user determines and specifies the refraction layer that is represented by each arrival time entered as input data; if a refraction layer is not specified (input value of zero), that arrival time is not used in computing the depth model; and (2) the program user determines and specifies the position (in 3-D space) of each shotpoint and geophone for which arrival times are entered as input data.

The limits of input data are: (1) Number of layers in a problem, 2 to 5; (2) number of geophone spreads in a problem, 1 to 5; (3) number

of shotpoints per spread, 1 to 7; and (4) number of geophones per spread, 2 to 25.

### Errors in Seismic Data Interpretation

Errors in interpretation of seismic refraction data have been extensively studied and reported (Domzalski, 1956; Soske, 1959; Green, 1962; Berry, 1971; Greenhalgh, 1977; Whitely and Greenhalgh, 1979). Sources of error common to shallow seismic refraction studies in arid, alluvial, and fractured sediments are hidden layers and velocity inversions which are collectively known as "masked layers" (Schmoller, 1982).

#### Hidden layers

A "hidden layer" is a subsurface layer that cannot be identified by first arrivals because of insufficient thickness or velocity contrast with the underlying layer (Soske, 1959). The term "blind zone" is used in conjunction with the hidden layer problem and it refers to the maximum theoretical thickness of a hidden layer. Blind zones are hypothetical spaces that exist at every recorded refractor. Any hidden layers, if present, will occur within this space (Merrick and others, 1978; Greenhalgh, 1977). In most cases, the blind zone will lie between the surface low-velocity layer and a high-velocity layer at depth. If time-distance graphs show a very large velocity contrast (i.e. 4,500

ft/sec to 16,000 ft/sec) between the first and second layer, existence of an intermediate velocity, hidden layer may be suspected. In practice, a blind zone can be empty or contain one or more hidden layers. Thickness of a hidden layer will be between zero and a maximum value that is a function of the velocity contrasts with adjacent layers. Presence of a hidden layer results in underestimation of depth to the refracting layer. If the presence of a hidden layer is suspected, there are methods available to estimate its maximum possible thickness (Redpath, 1973; Merrick and others, 1978; and Schmoller, 1982). These methods are based on prior knowledge of the study area and may not be applicable in unexplored areas.

#### Velocity inversion

Velocity inversion can occur wherever a geologic layer has a lower seismic velocity than that of the overlying layer. According to Snell's Law, critical refraction at the top of a low velocity layer is not possible, therefore, it cannot be directly detected in the course of a normal seismic refraction survey. In arid alluvial sediments, velocity inversions could result from caliche layers, sand or gravel beds, lateral changes in weathering of bedrock surfaces, fault and breccia zones, large vertical differences in moisture content, buried animal dwellings, or boulders buried at some depth. In any case, velocities do not always increase progressively with depth, and at some point in the stratigraphy there may be a downward transition to a relatively lower velocity (fig. 12). This has the effect of refracting the seismic

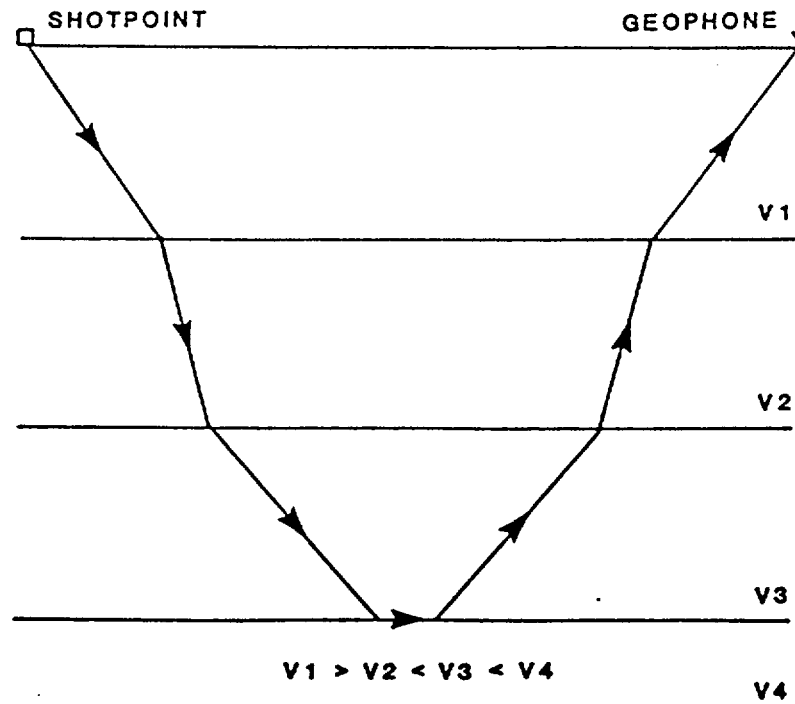
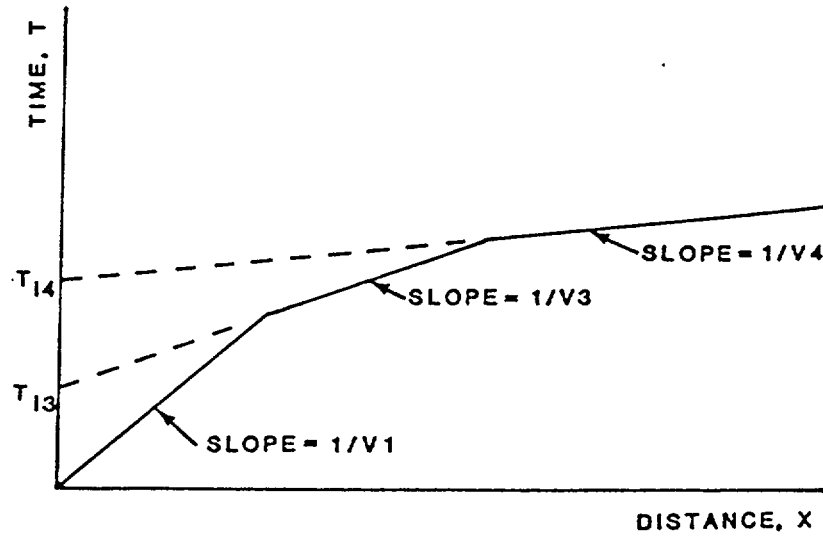


Figure 12.--Velocity reversal and corresponding time-distance graph (modified from Redpath, 1973).

ray downward toward the vertical. Refractions from a low velocity layer cannot be detected at the surface, therefore first arrivals are not recorded. The effect of a velocity reversal is to make computed depths greater than actual depths.

#### Progressive increase in velocity

A third type of velocity-depth problem is a continuous increase in velocity with depth; the bedrock surface will act as a zone of transition rather than a well-defined boundary. Example causes are: (1) Finely stratified layering that increases in density with depth due to compaction; and (2) progressive decrease in weathering with depth. A continuous increase in velocity with depth will appear on a time-distance graph as a curve rather than as a series of distinct line segments.

#### Types and characteristics of seismic sources

Several types of sources have been used to generate seismic waves for shallow refraction studies. The primary objective is to transfer energy into the ground. Secondly, a wavefront that has a sharp rise time, rather than a gradual beginning, must be produced.

## Explosives

An explosion is the most common seismic source. Signal strength is dependent on the amount and type of explosive used. Coupling to the ground is achieved by burying the explosive and then saturating the hole with water or drilling mud. The resulting wavefront will be sharp. Charge weight required depends upon local geology, length of the seismic line, and amount of background noise. Charge weight may vary from a blasting cap for a 100 ft line to several pounds of explosives for a long line under adverse conditions.

Use of explosives is limited by concerns of safety and speed. Explosives may only be handled by trained individuals who must operate under legal restrictions. In most seismic operations, the charge is planted in the earth at depths ranging from a few to several hundreds of feet (less than 25 ft is common for shallow refraction work). This requires drilling or augering of access holes.

## Weight Drop

A weight drop from some height is most often used as a seismic source for reflection surveys. The amount of energy transferred to the ground is proportional to the mass of the weight and the change in velocity at the instant of impact (Mooney, 1977, p. 21-1). By doubling the mass of a weight, the amplitude of a seismic wave will be doubled, however, the horizontal and vertical range of investigation will not

double proportionately. A seismic wave signal will decrease with approximately the square of the distance, therefore, increasing the mass of the weight by a factor of two, will increase the range of investigation by a factor of about  $2^{\frac{1}{2}} = 1.4$ . Terminal velocity of a falling object is proportional to  $MH^{\frac{1}{2}}$ . To double the signal amplitude from a given weight drop, the mass (M) would need to be increased by a factor of 2 or the height (H) by a factor of 4.

If the weight penetrates the ground surface upon impact, the wavefront will build more slowly and fail to produce a sharp rise. Because a heavier weight will tend to penetrate the ground, effectiveness of increasing the mass of the weight may be lost. To lessen the effects of this phenomenon, the weight should be dropped on a hard surface whenever possible. Weight bounce should be avoided because this energy is transferred to the ground. An ideal drop would stop the weight instantly upon impact.

Shape of the weight should be such as to avoid horizontal motion upon impact. A flat or oval-bottomed weight will usually impact one edge before the other, dissipating energy into horizontal signals. A sphere is an excellent shape, provided it is not dropped into a hole so that it makes first contact along the side.

## Sledgehammer

Effectiveness of a sledgehammer strike as a seismic source is governed by the same considerations as a weight drop. Two additional factors need also be considered. The first regards increased impact velocity provided by swinging the hammer. A study by Mooney (1977) indicates that a hard swing can increase signal amplitude by a factor of 2. The second factor to consider arises from use of a strike (or impact) plate. A strike plate serves to stop the hammer upon impact. Without a plate, the head of the hammer can sink into the ground and produce the same negative result as mentioned with the weight drop.

Size of the strike plate required is determined by the nature of the ground surface. If the plate is too small, it can be driven into the ground by successive blows. If it is too large, much of the energy from the impact can be dissipated through vibration. In this study, it was experimentally determined that a 0.9 by 1.25 ft aluminum plate was most effective.

The sledgehammer must strike the plate perpendicularly to impart maximum energy. It should also strike near the center of the plate to avoid driving one corner of the plate into the ground. Number of strikes per seismic record varied from three for 55-ft interior shots to more than twenty for 110-ft offset shots. The only criteria for determining the number of sledgehammer strikes required for a particular seismic record is the quality of the "first breaks" obtained.

## Signal Enhancement Seismograph With Respect To Energy Source

The signal enhancement seismograph has expanded the utility of non-explosive sources. The basic function of the signal enhancer is to stack successive seismic signals. This allows the true seismic signal to "grow" and become more distinct while background noise is limited or drowned out. The seismic signal increases in definition because refraction will occur at the same point on the record. Reduction of noise is achieved because it is a random signal that will not occur at the same time on successive seismic records.

### STUDY AREA

#### Geographic and Geologic Setting

Yucca Mountain is located on the U.S. Department of Energy's Nevada Test Site (NTS), Nye County, Nevada. It lies on the western boundary of the NTS, between Bureau of Land Management and U.S. Air Force lands (fig. 13). The NTS is located within the most arid region of the United States. Average annual precipitation at Yucca Mountain is estimated to be 4 to 6 inches. Depth to ground water ranges from about 1,500 to 2,300 ft (Waddell and others, 1984).

Yucca Mountain is an eastward-tilted volcanic plateau composed of ash-flow tuffs and related rocks of Miocene age (Scott and Castellanos, 1984). Most exposures on Yucca Mountain are the Tiva Canyon Member of

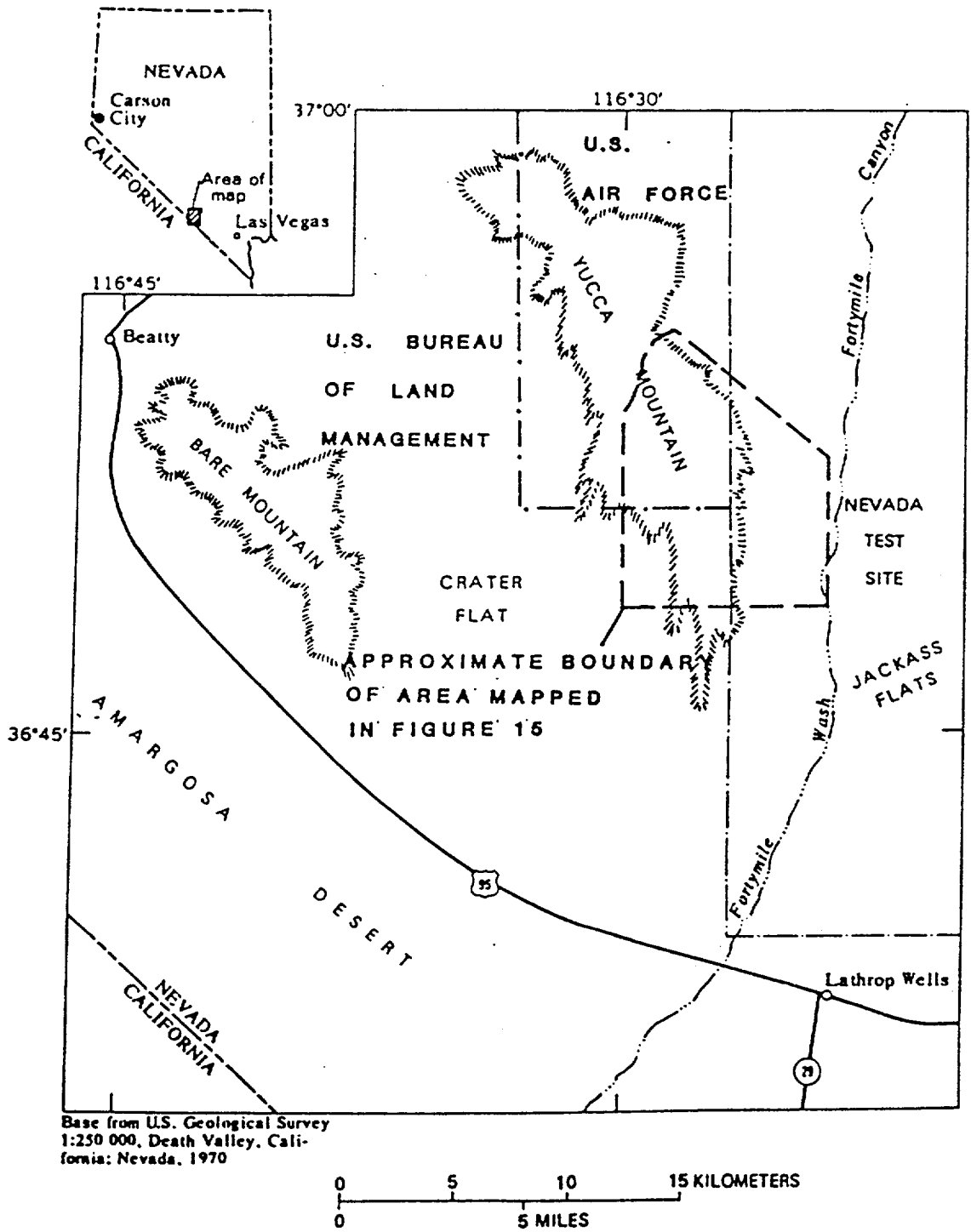


Figure 13.--Location of Yucca Mountain.

the Paintbrush Tuff. East-west trending alluvium-filled washes occur on both sides of the mountain and form the major drainage system. Bedrock underlying the alluvium is generally the Tiva Canyon Member.

Alluvium is used as a general term to describe any deposit that involves water transport. It includes debris flows and stream deposits. Particle sizes range from silt to boulders (Hoover and others, 1981). In the washes surveyed, the surface unit is a fluvial deposit of Holocene age. It consists of gravel, sand, and silt, intermixed and interbedded, poorly to moderately well-sorted. Gravel is angular to subrounded. Boulder patches and trains are common. No pavement has developed. The lower alluvial unit is of Pleistocene age and consists of gravel, sand, and silt, poorly to moderately well-sorted, nonbedded to well-bedded. Sand and silt occur as a matrix for gravel, as sand and gravelly sand beds, and as lenses interbedded with gravel (Swadley, 1983).

The Tiva Canyon Member is a multiple-flow compound cooling unit of moderately to densely welded ash-flow tuff. The unit is petrographically distinguished by a mafic-rich caprock, a sanidine-rich and hornblende-rich lower section, and the presence of sphene throughout the unit. Scott and Castellanos (1984) have created field subdivisions based on mineralogical, degassing, weathering, jointing, and welding features (fig. 14). These subdivisions, in descending order, are: (1) Light-brown caprock; (2) gray caprock; (3) upper cliff; (4) upper lithophysal; (5) lower cliff; (6) gray clinkstone; (7) red clinkstone; (8) lower lithophysal; (9) hackly; (10) columnar; (11) and basal.

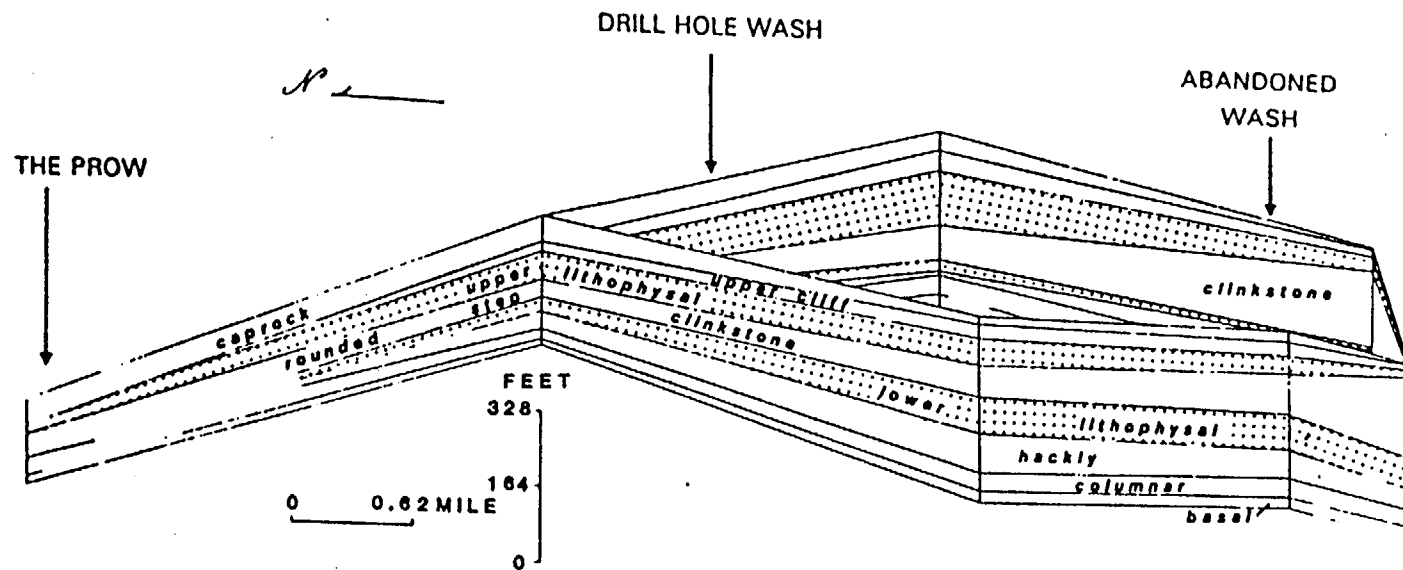


Figure 14.--Fence diagram of field subdivisions of the Tiva Canyon Member (modified from Scott and others, 1983).

It has been shown that a correlation exists between the degree of welding and rock mass properties such as porosity and fracture density (Scott and others, 1983). Densely welded tuff fractures readily; non-welded tuff does not. Columnar jointing characterizes zones of dense and partial welding. Joints are formed as a response to tensional forces that are active during cooling of the flow (Winograd and Thordarson, 1975). Joint spacings range from a few tenths of an inch to many feet (ibid). More closely spaced joints occur in the zone of most intense welding. Degree and extent of bedrock weathering is variable. Petrographic studies indicate that differences in weathering characteristics are related to differences in devitrification textures (Scott and others, 1983). Weathered surfaces composed of small (2 to 3 inches), irregular fragments, have small, finely fibrous devitrification textures. Weathered surfaces with 3-ft-long, smooth, conchoidally fractured blocks, have long, coarsely fibrous devitrification textures. The columnar zone has an almost unaltered glass shard texture.

Geologic units encountered in test hole USW H-4 (fig. 15) are representative of the stratigraphy expected beneath most seismic lines. The first bedrock unit penetrated by the drill hole is the Lower Lithophysal Subunit of the Tiva Canyon Member (Whitfield and others, 1984). This subunit is densely welded and devitrified. Calculated fracture density is 6.23 fractures/unit ft<sup>3</sup> (Scott and others, 1983).

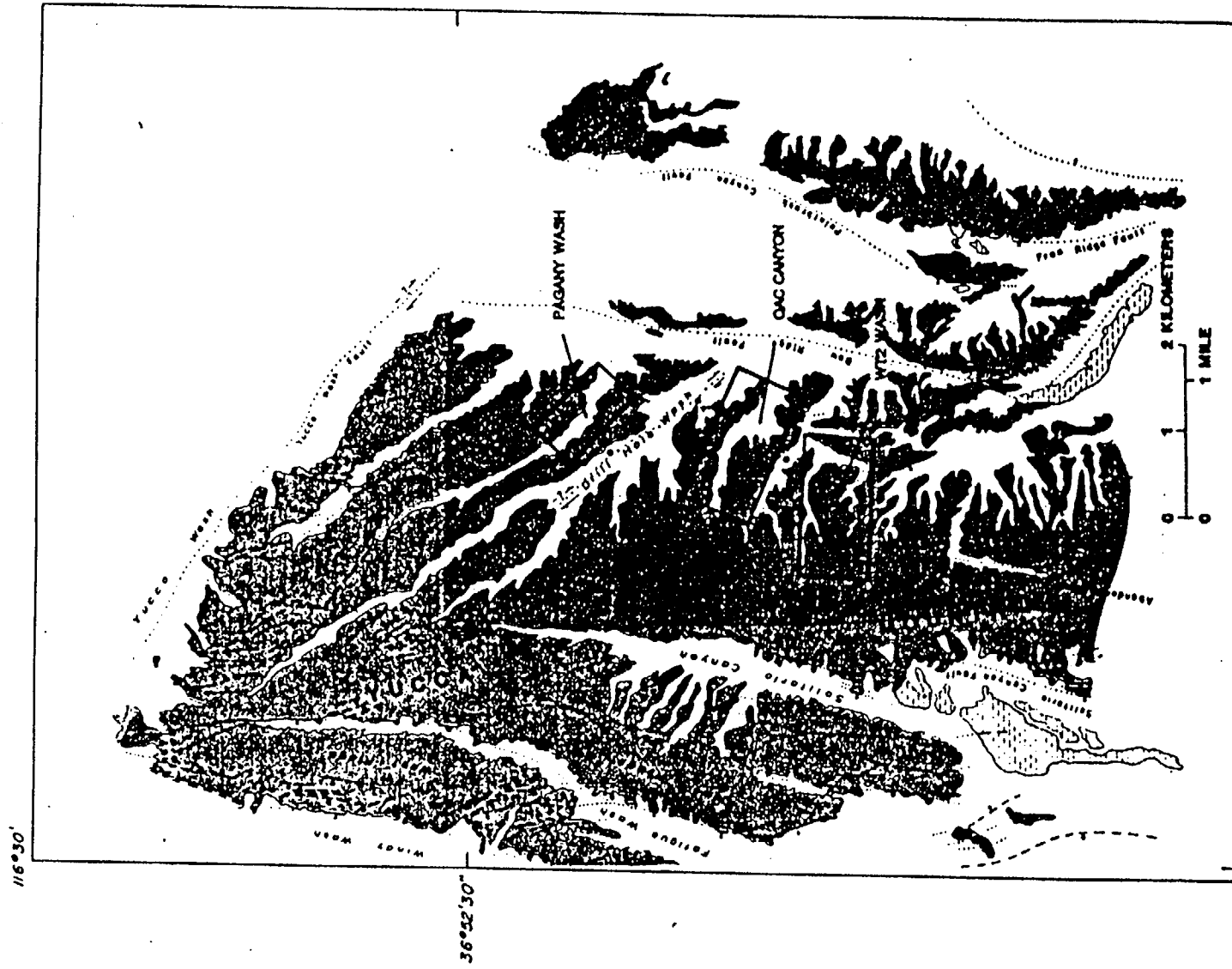


Figure 15.--Map showing location of study areas

### Local Study Areas

The study areas (fig. 15) were selected because: (1) Neutron-access holes were sited for future drilling in these washes and borehole data could be used to verify seismic results, and (2) they did not contain boreholes and information regarding depth to bedrock was not available.

Vegetation in the washes is sparse. Varieties include creosote bush (Larrea divaricata), sagebrush (Artemesia tridentata), Mormon tea (Ephedra nevadensis), and various grasses. The washes contain compacted road beds, stream channels (surface and buried), debris piles, and animal burrows which can adversely affect seismic records through signal dispersion due to decreased grain-to-grain contact and increased gas-filled void space. Road beds had been established to drilling sites and are made of compacted, local materials. Stream channels are present in all study areas and vary in width and depth of cut below land surface. Debris piles are composed of weathered ashflow tuff and gravel. Buried and partially-buried debris piles are commonly inhabited by burrowing animals. These conditions controlled the location and number of seismic lines that could be surveyed in an area. In general, selected sites were clear of stream channels and road beds, relatively level, and free of obviously loose, disturbed surface sediments. Lines were set parallel to the length of the washes because of the narrow width of the washes and the length of seismic lines necessary to record bedrock refractions.

Pagany Wash is 2.5 miles in length and has an average width of 340 ft in the upper wash and 430 ft in the lower wash. Total area is approximately 510 acres. Elevation ranges from 3,840 to 4,380 ft. Average slope of the walls is 0.46 in the upper wash and 0.35 in the lower wash. Stream channels are located across the bottom of the wash; depth of cut below land surface ranges from 0 to 4 ft.

The wash was undisturbed at the beginning of this study; there were no roads or boreholes. Seismic line locations were initially estimated. After several neutron-access holes were drilled, the lines were mapped by locating them in reference to the surveyed borehole locations

Qac Canyon is 1 mile in length and has an average width of 430 ft in the upper wash, 445 ft in the middle wash, and 800 ft in the lower wash. Total area is approximately 385 acres. Elevation ranges from 3,820 to 4,280 ft. Average slope of the walls is 0.45 in the upper wash, and 0.30 in the middle and lower wash. The northwest extent of the wash is divided by a bedrock spur into two branches. At the juncture, a large area has been disturbed from a trenching project. A stream channel with a cut of 0 to 6 ft runs eastward from the trench along the south wall of the wash. A jeep trail is located in the approximate center of the wash and extends for the entire length.

Qac Canyon did not contain any boreholes. Seismic lines were located on the map by siting to two or more control points. Control points were coordinate locations that had been surveyed prior to this study, for example: (1) Control point #1, original site for test well USW WT-2; (2) control point #5, a recording seismic station; (3) control point #6, west boundary, NTS; and (4) seismic shothole US-25#1. Several neutron-access holes were tentatively sited in this area, therefore many seismic lines were run.

The third area surveyed is unnamed, and is referred to as WT2 Wash. It is 0.6 miles in length and has an average width of 315 ft in the upper wash and 250 ft in the lower wash. Total area is approximately 165 acres. Elevation ranges from 4,020 to 4,340 ft. Average slope of the walls is 0.15 in the upper wash and 0.30 in the lower wash. Narrow stream channels are located between the base of the walls and a road bed.

Neutron-access holes located in this wash have not been drilled or surveyed. Therefore, seismic lines were located on the map in relation to prominent land forms.

## PREVIOUS WORK

Sledgehammer Seismic Refraction Method

The sledgehammer seismograph was developed by Gough (1952) for use in seismic investigations of subsurface geologic structure to a maximum depth of about 100 ft. The original equipment consisted of: (1) A 10-lb sledgehammer with inertia contactor; (2) a timing unit; (3) a single geophone; (4) an amplifier unit; (5) a display unit with cathode-ray tube; and (6) a power supply unit. Parts (2), (4), and (5) were built into a single receiver unit. The inertia contactor consisted of two flat springs with silver contacts that were normally separated by 0.01 inch. When the hammer struck a hard surface, the upper spring bent under the inertia of its own mass and closed the gap. A voltage pulse was sent from the contactor to a trigger circuit in the receiver. Input time-constants were designed such that if the contactor closed more than once for a given blow, due to vibration of the upper spring, only the first contact would operate the trigger. A vertical-component, moving-coil geophone was used. The geophone was connected to the amplifier with shielded cable because of the voltage surge induced when the contactor closed.

Field procedures consisted of burying the geophone 100 ft from the receiver unit and setting shotpoints at increasing distances away from the geophone. The method of increasing shotpoint distance was intended to allow the operator to become familiar with the appearance of the seismic wave at short range, where noise was not visible, so that the

same signal could be recognized in noise at large distances. Accuracy of surveying techniques and depth models was tested by surveying an area that contained several boreholes that determined layer depths directly. A typical, long seismic line was about 800 ft with 33 shotpoint locations. The number of sledgehammer strikes per record ranged from 4 to 20. Data were interpreted using intercept times. The seismic lines were not reversed, and depths obtained represented an average over the length of the line. Seismic depths compared to borehole depths within a range of 15 percent.

#### Shallow Seismic Refraction Surveys in Hydrologic Investigations

Research of geophysical and hydrologic literature yielded no reports of shallow seismic investigations conducted in unsaturated sediments only. Previous work in weathered bedrock and alluvium, or similar unconsolidated sediments, has been conducted in areas with a relatively shallow water table and location of the velocity horizon between unsaturated and saturated sediments was at least one of the study objectives. Although the magnitude of velocity values from saturated sediments cannot be directly compared to unsaturated velocity values, previous seismic investigations in unconsolidated sediments and weathered bedrock zones have reported similar difficulties and results that were attributed to the sediment type rather than the presence or absence of fluid.

Shallow seismic refraction studies were conducted by Hobson to determine bedrock topography and thereby identify previously existing surface-drainage systems (Hobson and others, 1964; Hobson and Carr, 1967). Bedrock units were overlain by Pleistocene sands, gravels, and tills. Depths to bedrock were determined within 7.3 percent of borehole depths. Within the study area, three layers of unconsolidated sediments were identified based on compressional wave velocity. Beneath any one seismic line, each layer was represented by one of two or more velocity sub-layers. The range of velocities was attributed to different degrees of compaction. Stratigraphic differentiation between unconsolidated sediments was possible in general terms only. The soil zone and aerated tills were identified with velocities of about 1,500 ft/s and less. Low occurrences of high-velocity (3,000 to 6,750 ft/s) unconsolidated material were identified as tills with a large concentration of cobbles and boulders (Hobson, 1967). Although velocities were not able to be identified with specific stratigraphic layers, the velocity demarkation between unconsolidated sediments and bedrock was determined to 6,750 ft/s.

Depth to the water table and thickness of saturated alluvial fill have been determined using seismic refraction methods to locate the velocity horizon between saturated and unsaturated sediments. Studies conducted in alluvium-filled valleys and river channels have reported that depths determined by seismic methods corresponded within 10 percent of borehole depths (Duguid, 1968; Wahrhaftig, 1984). Differentiation based on compressional wave velocity was possible between saturated and unsaturated sediments, and alluvium and bedrock only. For unconsolidated

materials in general,  $V_{sat}$  (saturated velocity) is about 5,000 ft/s and  $V_{usat}$  (unsaturated velocity) is 1,000 ft/s (Haeni, 1984).

Weathered bedrock zones underlying alluvium have been identified as layers with velocity values intermediate to alluvium and non-weathered bedrock (Duguid, 1968; Wahrhaftig and others, 1984). Depths to the weathered zone were determined within 5 to 10 percent of depths determined by borehole data. Thickness of the weathered zone was obtained where velocity contrasts between overburden, weathered bedrock, and non-weathered bedrock were appreciable. Where the weathered zone had insufficient thickness and(or) velocity contrast with overlying layers, refractions were not recorded and the weathered zone was considered as a hidden layer. Because bedrock refractions were from the base of the weathered zone, actual depths to bedrock were less than those determined by seismic methods.

#### Seismic Studies in the Yucca Mountain Area

Previous seismic studies in the Yucca Mountain area were primarily concerned with identifying regional structure and basement complexes. Seismic waves generated by tectonic events, nuclear weapons tests, and conventional explosives were recorded (King, 1982; Pankratz, 1982; Hoffman, 1983). Summary reports contain little information regarding velocities and geologic layering for depths less than 100 feet. Two studies that did provide information pertinent to this study were conducted by Pankratz and Ackerman.

Experiments conducted by Pankratz in December, 1978 and September, 1979 included three 1.7-mile seismic lines that were located in the vicinity of Yucca Mountain. The spreads are shown in figure 16 as Yucca A, Yucca 2b, and Yucca C. Three problems noted in his summary report were: (1) Inaccessability of the area to vehicles, (2) difficulty in obtaining adequate first arrivals which he attributed to absorption of seismic energy in weathered material, and (3) lateral velocity variations having no geologic significance (Pankratz, 1982). In general, results in the Yucca Mountain area were considered poor and subject to discrepancy with velocity and depth information obtained from borehole data (Ue-25a#1). Discrepancies were attributed to the following factors: (1) Low signal-to-noise ratio due to the absorptive character of the subsurface, (2) occurrences of undetected low-velocity layers, (3) the existence of a major vertical discontinuity between materials of contrasting velocity in the vicinity of the seismic spread (i.e., fault blocks with different degrees of weathering or welding), and (4) the suspected presence of a strong anisotropy of acoustic impedance. With much caution, he assigned velocities of approximately 5,577 ft/s to the Tiva Canyon Member and velocities of approximately 6,562 ft/s either to the lower Tiva or the upper Topopah Springs Member.

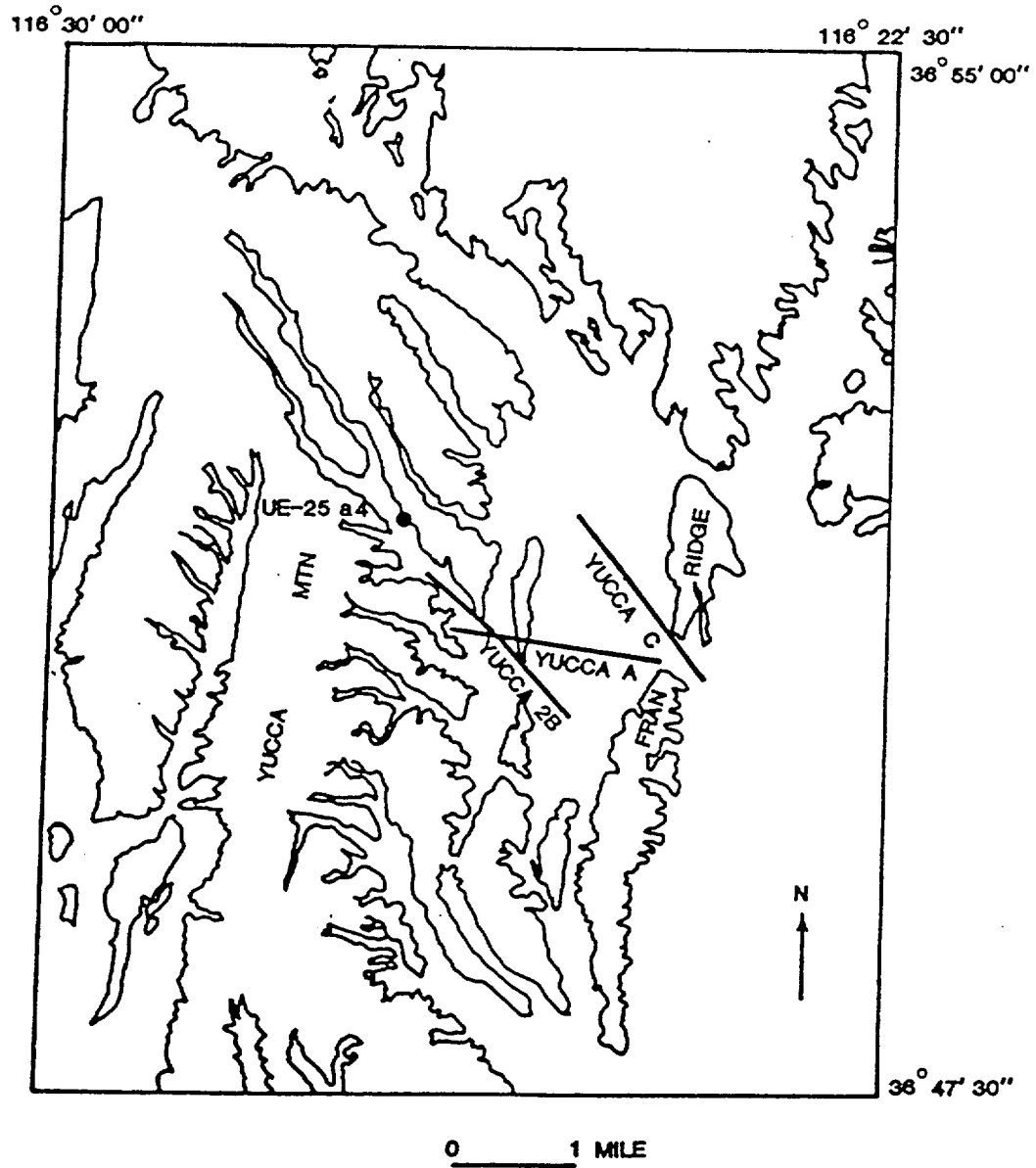


Figure 16.--Location of seismic lines surveyed by Pankratz (modified from Pankratz, 1982).

Location of the seismic line surveyed by Ackerman is shown in figure 17. The line consisted of three spreads, 48 geophones per spread. Shotpoints were 50 feet deep and explosive charge weight varied from 10 to 75 pounds.

One important result of this investigation was the observation and experimental verification of the apparent large variability in seismic velocity of the welded Tiva Canyon Member. At the eastern end of the seismic line, velocity of the Tiva Canyon Member was approximately 10,000 ft/sec. At the western end, near Exile Hill, the velocity was about 6,800 ft/sec (Ackerman, written commun. 1984). To further verify the velocity variation, measurements were made in wells along the crest of Yucca Mountain and velocity values obtained were lower yet (no velocity value cited). A functional relationship between degree of welding and velocity was not established, although it has been generally agreed upon that degree of welding is the primary factor affecting density in ash-flow tuffs, and density to a large degree controls velocity (Ackerman, written commun., 1984; Scott and others, 1983).

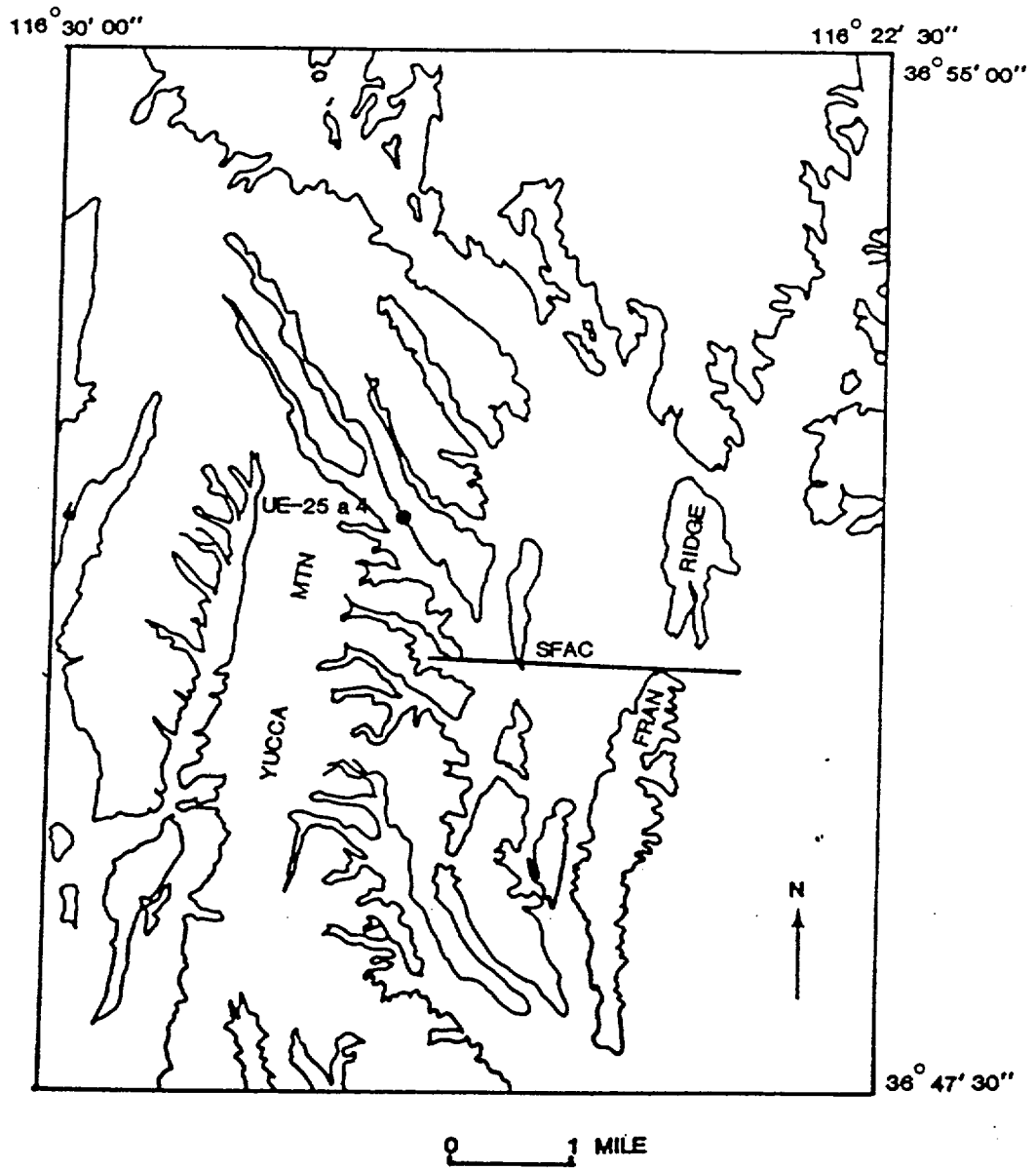


Figure 17.--Location of seismic line SFAC surveyed by Ackerman (Ackerman, written commun., 1984)

## MATERIALS AND METHODS

Seismic Refraction Survey Equipment

## Seismograph

The EG&G ES-1210 signal enhancement seismograph was used for all seismic surveys in this study. It is packaged in a weatherproof, aluminum case and operates from a 12-volt external power supply. It records 1024 by 10-bit words on 12 channels. Enhancement is achieved by signal sampling, digitizing and storage in a random access memory. Repeated signals are added while random noise is cancelled or limited. A CRT (cathode ray tube) screen continuously displays the signal stored in memory on all channels simultaneously, or on selected combinations of fewer channels. Each channel has a separate input gain control, trace-size control, and analogue filter mode-selector. Filter settings available are: (1) Band pass, that records on the selected frequency only; (2) band reject, that eliminates the selected frequency only; (3) low pass, that records low frequencies only; (4) high pass, that records high frequencies only; and (5) all pass, that records all frequencies. Filters are used to eliminate noise that may be present in a particular area. Vehicle traffic, machinery, and wind are examples of the noise that may be eliminated. Existing noise may be analyzed by depressing a noise monitor button that causes any noise being transmitted to the geophones to be displayed on the CRT. This capability aids in determining filter selection and quality of geophone emplacement. A variable time delay option allows recording signals from great depths

(greater than 100 ft) or use of time-delayed energy sources. Built-in voltage and resistance meters allow the operator to monitor power input and check cable and geophone conditions before recording.

Once a data set is recorded and stored in the seismograph memory, it is immediately displayed on the CRT for observing data quality and for adjusting individual trace sizes. A built-in electric writing oscillograph provides a permanent paper record when desired. Data is displayed and printed in either wiggle-trace or variable-area form (fig. 18). Wiggle-trace form produces a good printed copy from seismic records that contain much background noise or where several shots per seismic record are required. The first arrivals are recorded and printed as solid lines; the late, large amplitude, wave arrivals as scattered lines.

#### Cables and Geophones

Signal input is obtained through a 12-channel cable that connects directly to the seismograph. Receiver stations of 10, 20, 50, and 100 ft spacings are available. At each of the 12 stations, a geophone is connected with alligator clips. Fourteen-Hz Geosource SM-7<sup>1</sup> geophones were used for all surveys.

<sup>1</sup>Use of brand names is for descriptive purposes only and does not constitute endorsement by the U.S. Geological Survey.

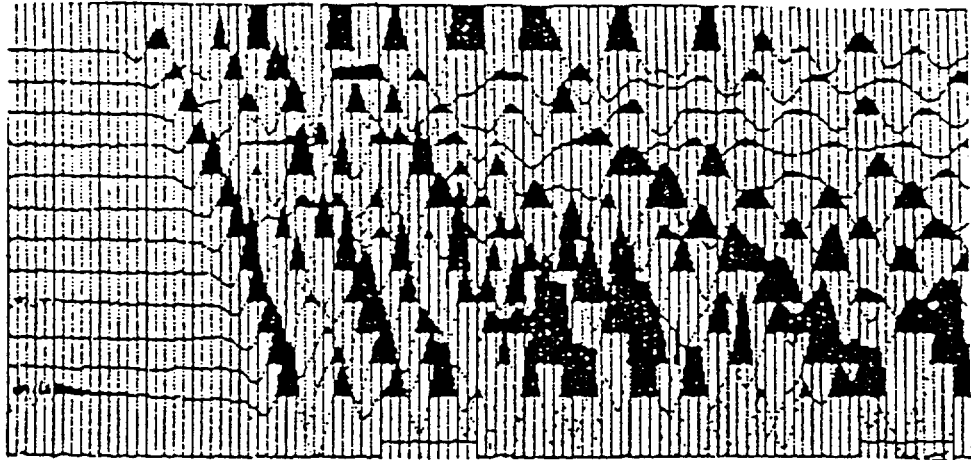


Figure 18A.--ES-1210 seismic data record with variable area trace.

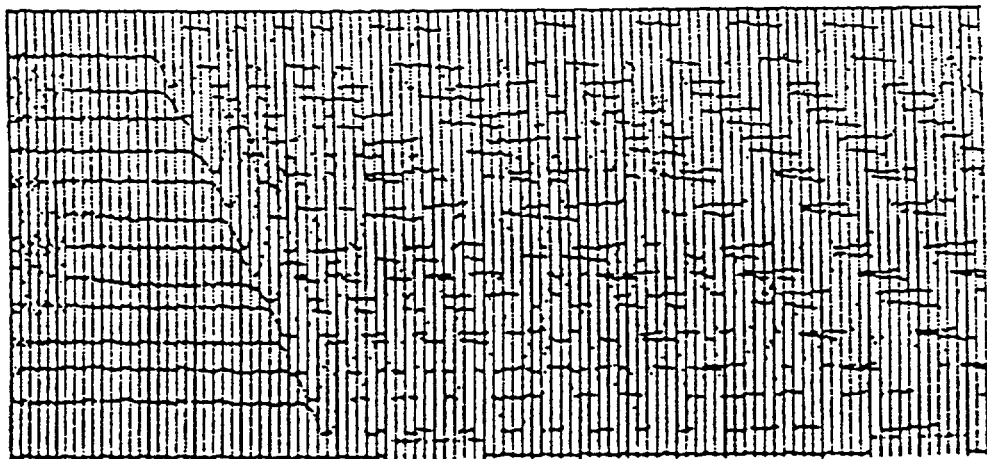


Figure 18B.--ES-1210 seismic data record with wiggle trace.

### Seismic Energy Source

Several energy sources are available for use with this system. A 12-lb sledgehammer impact on an aluminum plate was used for all surveys in this study. Zero-time for the seismic record is initiated by a switch that is attached with tape along the length of the handle, a few inches from the hammer head. It is protected by silicone from excessive vibration and environmental elements. A 250-ft cable between the sledgehammer and seismograph start-signal port allows the seismograph to remain stationary while the shotpoints are moved along the line.

### Miscellaneous Equipment

Assorted hand tools and spare parts are necessary to perform equipment repairs and modifications in the field. Screwdrivers, pliers, fuses, a volt-ohmmeter, wire cutter and stripper, electrical tape, extra wire, spare hammer switch, and heat-sensitive recording paper are some of the items that should be available.

### Field Vehicle and Survey Crew

The seismograph system and survey team was transported in a 4 X 4 pick-up truck. On most occasions, a two-member field crew operated the system. A few surveys were conducted by one person. Although less time-efficient, operating the system without assistance allowed the

author to more easily trouble-shoot field operations and determine optimum working arrangements.

### Equipment Setup

#### Geophone Cable and Geophones

After the survey site had been selected, the line was measured for cable length and shotpoints. Stakes were used to identify first and twelfth geophone positions. Rock rings identified shotpoints. The geophone cable was then laid out between the stakes. The cable was pulled taut as equidistant 10- or 20-ft geophone spacings were used. Geophones were then emplaced. Geophones were placed within 10 degrees of the vertical and firmly planted such that they would not wiggle when tested with a finger on the top. After each geophone was emplaced, it was connected to the geophone cable with alligator clips.

## Seismograph

The seismograph was operated from the seat of a vehicle. Geophone cable, 12-volt power cord, and start-signal cord connect to the seismograph. The geophone cable has a 12-pin Canon connector on each end and may be connected to the seismograph from either end. Connecting either end of the geophone cable determines which geophone (#1 or #12) is recorded at the top of the seismograph CRT screen. Screen position of the geophones can be determined by tapping the first or twelfth geophone or stamping the ground and then noticing which seismic trace responds on the CRT.

### Preliminary Survey

A seismic survey was performed to establish geophone and shotpoint arrangements capable of obtaining refractions from bedrock. This was accomplished by surveying an area where the depth to bedrock was known. Test hole Ue-25 a#4, located in Drill Hole Wash (fig. 16), was selected for this purpose. From drilling data, depth to bedrock was known to be 30 ft (Spengler, 1980). The geophone cable was laid out in a line across the drill site: 10-ft geophone spacings were used. The first shotpoint was set 40 ft southeast of geophone #1. Surveys with shotpoints at 50, 70, and 200 ft were also performed. First arrivals were not observed at any of the locations. As a result of these surveys, it was determined that the delay switch in the seismograph was malfunctioning. Wave arrivals were being recorded after an unknown, set

time delay. As a check for the malfunction, a seismic line was surveyed on Frenchman Flat, NTS, where refraction surveys had been previously performed and first arrivals were obtained. First arrivals were not observed. Large-amplitude, irregular wave traces were recorded. On recommendation of the manufacturer, the delay switch was removed from the seismograph and the preliminary survey resumed. First arrivals of sequentially greater time at each geophone were then observed. Ten-ft geophone spacings were determined to be adequate and off-set shotpoints equal to the length of the geophone spread (110 ft) would be sufficient to obtain refractions from bedrock.

#### RESULTS AND DISCUSSION

Data interpretations are reported for seismic surveys that produced data records with first arrivals that could be picked within a 2-ms (millisecond) range and depth models that were verifiable by borehole data or field correlation.

Elevations cited are relative for each line. Where land surface is horizontal over the length of the seismic line, land surface is assigned an elevation of 0.0 ft. Elevation of velocity layers beneath a horizontal line are given as feet below land surface. Seismic lines surveyed on a sloping surface are assigned elevations relative to the last shotpoint. The furthest shotpoint down-slope is assigned an elevation of 0.0 ft; elevations for geophones and other shotpoints are calculated for the appropriate slope angle. This method of elevation assignment is

considered to be the easiest and most practical method for this study because the information desired is thickness of alluvium beneath land surface.

Seismic line trends were sited from geophone #1 to geophone #12. Where the land surface was sloping, geophone #12 was the furthest geophone down-slope.

Seven shotpoints were used for each seismic line wherever possible. For a 110-ft geophone spread (10-ft geophone spacing), with respect to geophone #1, shotpoints were placed at -110 ft, -55 ft, -10 ft (forward shotpoints), 55 ft (interior shotpoint), 120 ft, 165 ft, and 220 ft (reverse shotpoints) (fig. 19). Several attempts were made to obtain data records from -165 and 275 ft. These records were of poor quality and first arrivals could not be picked with the desired precision.

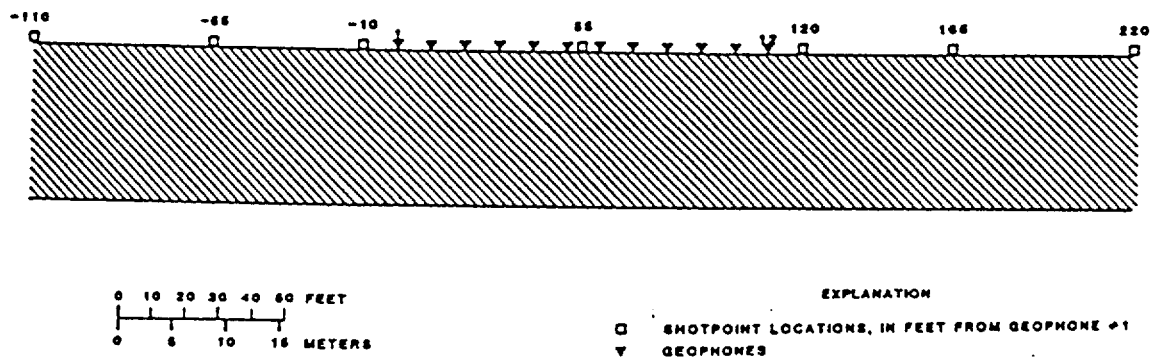


Figure 19.--Shotpoint and geophone locations for a typical seismic line.

#### Pagany Wash

Eight neutron-access holes are located along a line that extends about 180 ft across the wash (fig. 20). Stream channels intersect the line between access holes N5 and N6. Alluvium-bedrock contacts, measured below land surface are; N2, 0 ft; N3, 9 ft; N4, 24.5 ft; N5, 44.5 ft; N6, 39.5 ft; N7, 40.5 ft; N8, 40 ft; and N9, 35 ft (Hammermeister, written commun., 1985). N2 and N5 are 86 ft apart and have a 44.5 ft difference in depth to bedrock. N4 and N5 are about 26 ft apart and have a 20 ft difference in depth to bedrock.

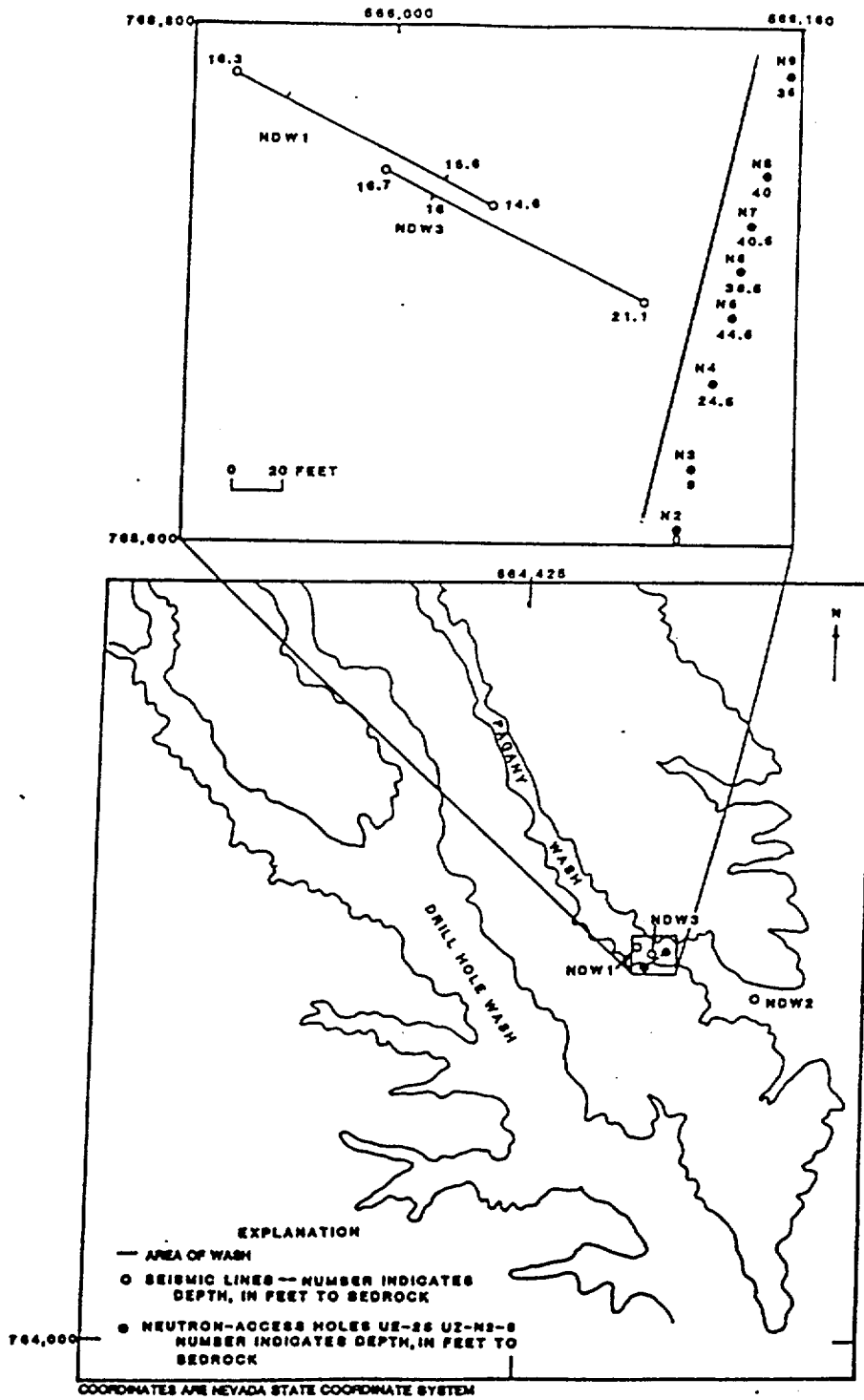


Figure 20.--Location of seismic lines and neutron-access holes in Pagany Wash

## Seismic Line NDW1

The line was located about 78 ft northeast of the south wall of the wash. Northeast of the line was a well-developed stream channel with a cut of about 4 ft below land surface. Data acquired were good with exception of the 220-ft shotpoint. Recorded waveforms were complete, however, first arrivals were difficult to pick within the 2-ms range of precision. Four velocity layers were identified on the time-distance graph (fig. 21). Three data sets were used to generate depth models: (1) Model #1 was obtained using estimated first arrival times from the 220-ft shotpoint; (2) model #2 was obtained by deleting layer designations from the 220-ft shotpoint; and (3) model #3 was obtained by adding the 2-degree slope of the land surface to the input data of (2).

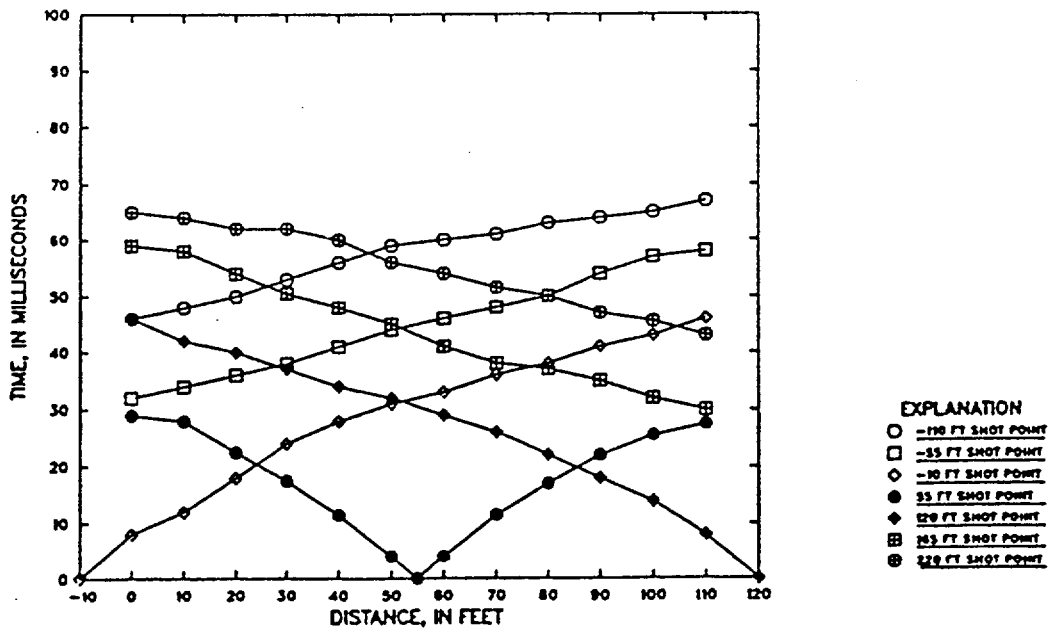


Figure 21.--Time-distance graph for seismic line NDW1.

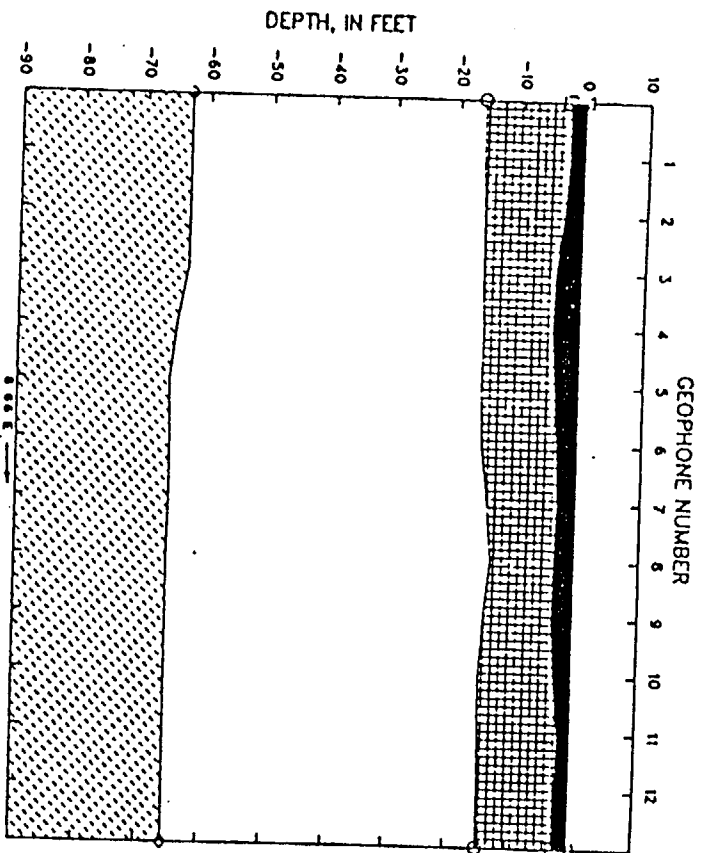
Velocities generated from the three models range within 2 percent for a particular layer (table 2). Because reciprocity of reversed profiles requires that total travel times and identifiable layers be the same for reversed shotpoints, velocity layers identified from the -110 shotpoint should be present at the 220-ft shotpoint. Refractions recorded at the -110 ft-shotpoint are from layers 3 and 4. Deleting layer designations from the 220-ft shotpoint has little effect on velocity determination because refractions from layers 3 and 4 also were recorded at the -110, -55, and 165-ft shotpoints and these arrivals were sufficient to calculate velocities and depths.

Table 2.--Seismic velocities, line NDW1.

Layer number	Layer velocity		
	Model #1	Model #2	Model #3
1	1250 ft/s	1251 ft/s	1251 ft/s
2	1965 ft/s	1966 ft/s	1966 ft/s
3	4138 ft/s	4078 ft/s	4078 ft/s
4	8229 ft/s	8172 ft/s	8172 ft/s

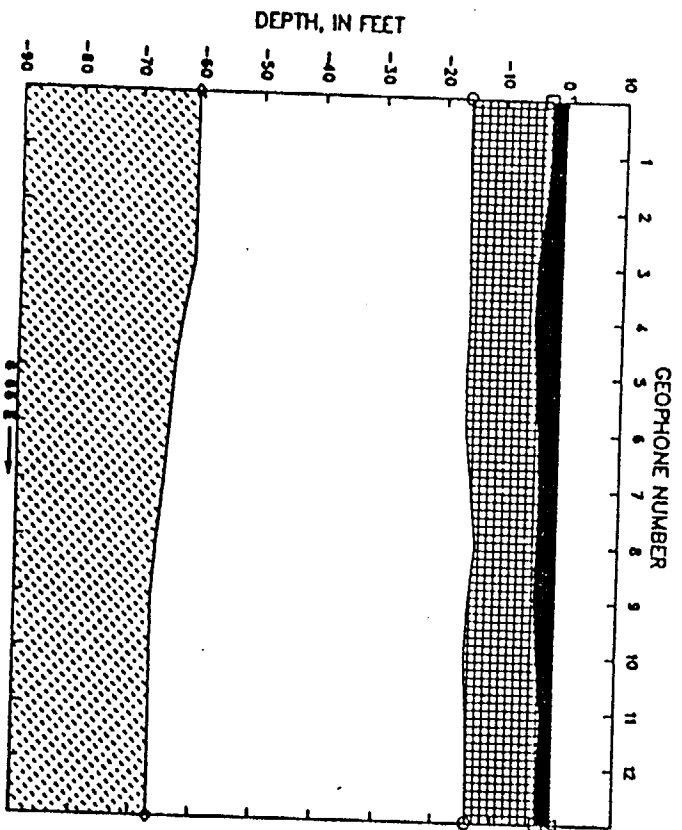
Depth plots obtained from each model are shown as figures 22, 23, and 26. Removing uncertain data from the 220-ft shotpoint changes the depth to layer 4 by less than  $\pm 2$  feet. Velocities and depths are considered to be accurate values because slope angle is small and refractions from all layers were recorded from reversed shotpoints.

Model #3 is considered the most reasonable interpretation of seismic line NDW1 (table 3).



- EXPLANATION**
- ▽ ALLUVIUM (MATERIALS) (T/2)
  - ALLUVIUM (MATERIALS) (T/2)
  - SANDSTONE (MATERIALS) (T/2)
  - ◇ GRAVEL (MATERIALS) (T/2)

Figure 22.--Depth plot, line NDW1, model #1.



- EXPLANATION**
- ▽ ALLUVIUM (MATERIALS) (T/2)
  - ALLUVIUM (MATERIALS) (T/2)
  - SANDSTONE (MATERIALS) (T/2)
  - ◇ GRAVEL (MATERIALS) (T/2)

Figure 23.--Depth plot, line NDW1, model #2.

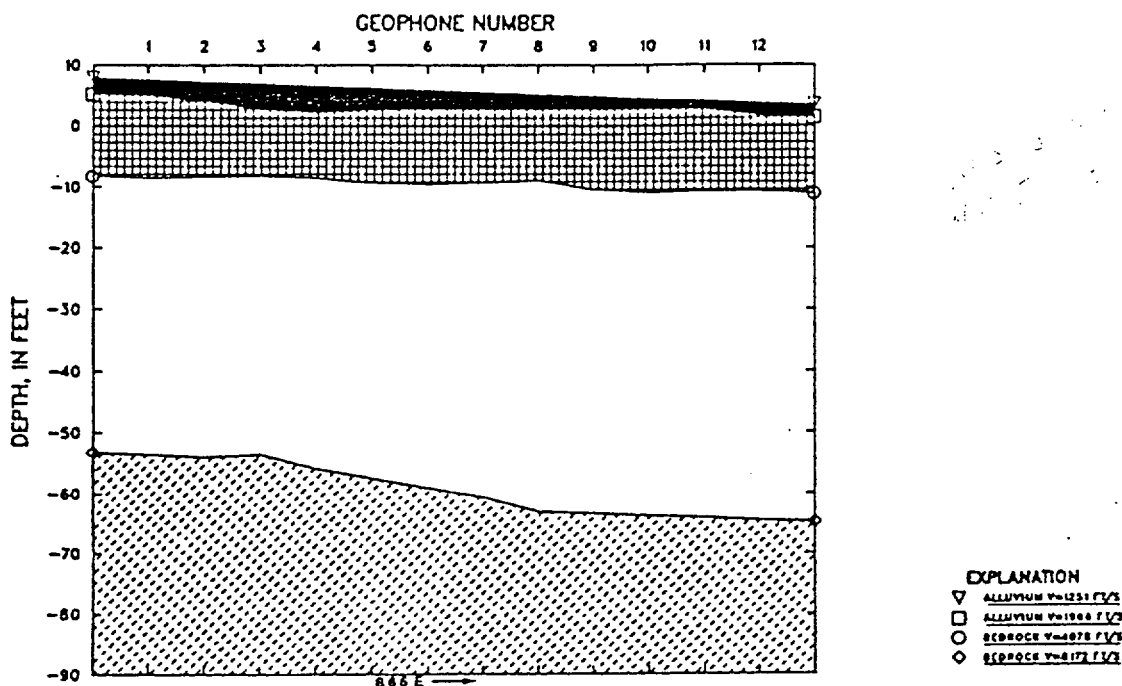


Figure 24.--Depth plot, line NDW1, model #3.

#### Seismic Line NDW3

Close proximity of this line to NDW1 caused anticipation of two results. First, that seismic velocities and number of layers would be the same as determined from NDW1. Secondly, because this line was down slope from NDW1, depth to bedrock was expected to be slightly greater. Four velocity layers are identifiable on the time-distance graph (fig. 25). Seismic velocities of layers 1 and 2 are greater than those from NDW1. This may be due to compaction of the alluvium by drilling support equipment and development of a jeep trail during the drilling of

nine neutron-access holes at or above (NW of) the seismic line site. Seismic velocities of layers 3 and 4 are within 10 percent of those obtained from NDW1. Seismic velocities and depth to layers beneath each geophone and the nearest (-10 ft and 120 ft) shotpoints are shown in table 4. A depth plot beneath the line is shown as figure 26.

Table 3.--Seismic depths beneath line NDW1, model #3.

Position of Layers Beneath Shotpoints and Geophones								
SP	Position	Surface Elev	Layer 2		Layer 3		Layer 4	
			Depth	Elev	Depth	Elev	Depth	Elev
3	-10.0	8.0	2.8	5.2	16.3	-8.3	61.2	-53.2
4	55.0	5.8	3.1	2.7	15.3	-9.5	65.6	-59.8
5	120.0	3.5	2.1	1.4	14.7	-11.2	68.3	-64.8
GEO								
1	0.0	7.7	2.8	4.9	16.3	-8.6	61.2	-53.5
2	10.0	7.3	3.3	4.0	15.7	-8.4	61.2	-53.9
3	20.0	7.0	4.4	2.6	15.3	-8.3	60.5	-53.5
4	30.0	6.6	4.5	2.1	15.2	-8.6	62.5	-55.9
5	40.0	6.3	3.8	2.5	15.7	-9.4	63.8	-57.5
6	50.0	5.9	3.2	2.7	15.6	-9.7	65.0	-59.1
7	60.0	5.6	3.0	2.6	15.0	-9.4	66.2	-60.6
8	70.0	5.2	2.6	2.6	14.2	-9.0	68.3	-63.1
9	80.0	4.9	2.0	2.9	15.5	-10.6	68.3	-63.4
10	90.0	4.5	1.7	2.8	15.6	-11.1	68.3	-63.8
11	100.0	4.2	1.6	2.6	15.1	-10.9	68.3	-64.1
12	110.0	3.8	2.1	1.7	14.6	-10.8	68.3	-64.5

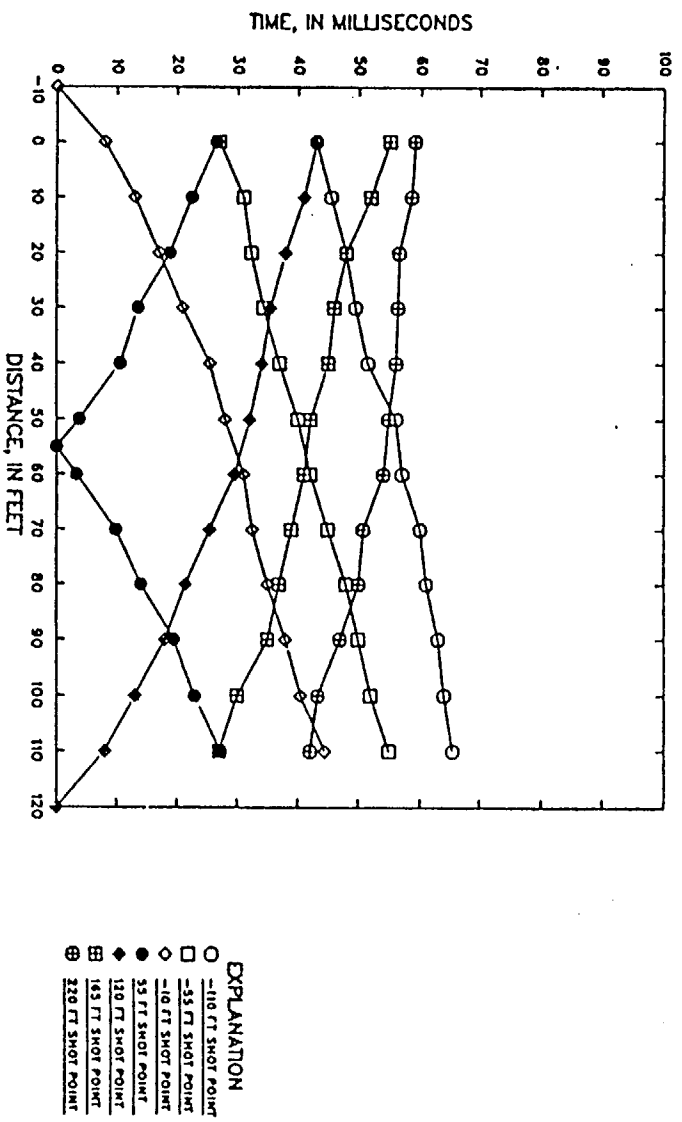


Figure 25.--Time-distance graph for seismic line NDW3.

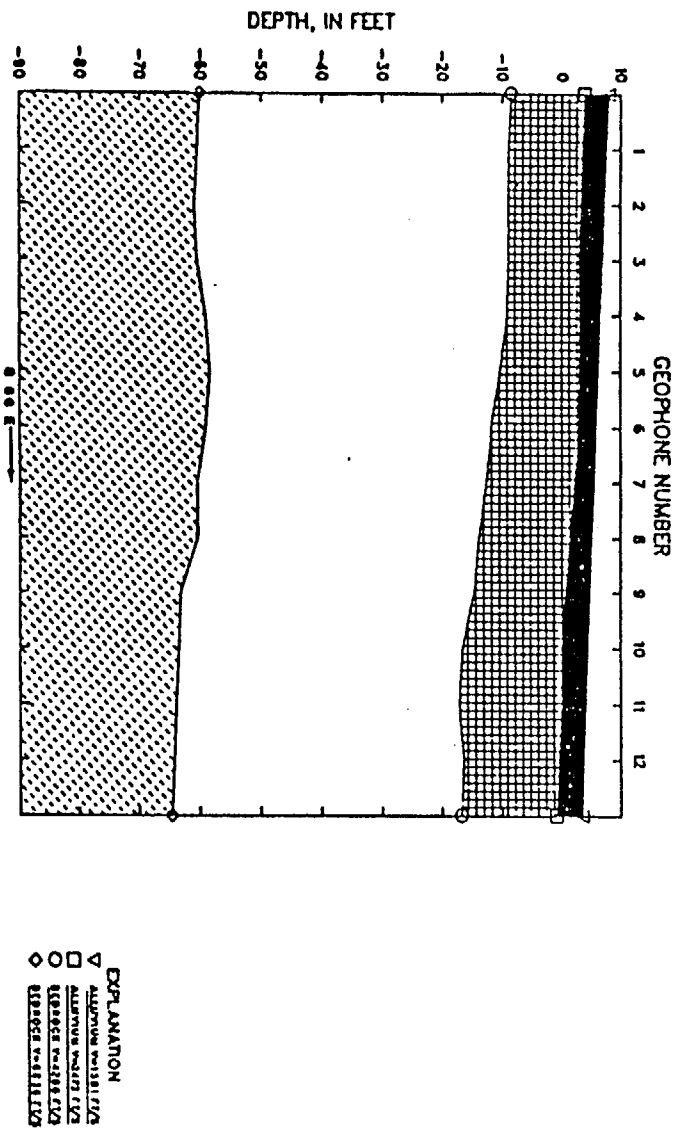


Figure 26.--Depth plot, line NDW3.

Table 4.--Seismic velocities and depths, line NDW3.

Layer number		Layer velocity							
1		1381 ft/s							
2		2472 ft/s							
3		4286 ft/s							
4		8836 ft/s							

Position of Layers Beneath Shotpoints and Geophones									
SP	Position	Surface Elev	Layer 2		Layer 3		Layer 4		
			Depth	Elev	Depth	Elev	Depth	Elev	
C	-10.0	8.0	4.1	3.9	16.6	-8.6	68.2	-60.2	
D	55.0	5.8	3.2	2.6	18.1	-12.3	65.6	-59.8	
E	119.9	3.5	4.4	-0.9	20.3	-16.8	68.1	-64.6	
GEO									
1	0.0	7.7	4.2	3.5	16.7	-9.0	68.2	-60.5	
2	10.0	7.3	4.1	3.2	16.3	-9.0	68.2	-60.9	
3	20.0	7.0	4.0	3.0	16.0	-9.0	67.5	-60.5	
4	30.0	6.6	3.5	3.1	15.8	-9.2	65.7	-59.1	
5	40.0	6.3	3.3	3.0	16.7	-10.4	64.7	-58.4	
6	50.0	5.9	2.9	3.0	17.8	-11.9	65.0	-59.1	
7	60.0	5.6	3.5	2.1	18.3	-12.7	66.1	-60.5	
8	70.0	5.2	3.9	1.3	19.1	-13.9	65.6	-60.4	
9	79.9	4.9	4.3	0.6	19.6	-14.7	68.1	-63.2	
10	89.9	4.5	4.6	-0.1	21.1	-16.6	68.0	-63.5	
11	99.9	4.2	4.2	-0.0	21.4	-17.2	68.1	-63.9	
12	109.9	3.8	4.4	-0.6	20.2	-16.4	68.0	-64.2	

Table 5.--Seismic velocities and depths to layers beneath seismic lines NDW1 and NDW3

Layer Number	NDW1		NDW3	
	Velocity (ft/s)	Average depth (ft)	Velocity (ft/s)	Average depth (ft)
1	1251	Surface	1381	Surface
2	1966	3.5	2472	3.9
3	4078	15.3	4286	18.3
4	8172	65.0	8836	67.0

Velocity layers 1 and 2 can be identified as surface and more-compacted alluvium respectively.

Depths to bedrock determined from neutron-access holes (fig. 20) more closely correspond to velocity layer 3 than layer 4. Although velocity values of about 4,200 ft/s are low for a rock unit, density and neutron-moisture logs from N3, N4, and N5 show a common increase in density and decrease in moisture content at the bedrock contact (Hammermeister, written commun., 1985). This suggests that although the bedrock surface may be weathered, it is significantly more dense than overlying sediments and should be identifiable by methods dependent on density contrasts. The low moisture content of the upper bedrock unit may also be a contributing factor to the low seismic velocity of the unit.

The bedrock unit penetrated by neutron-access holes N2 through N9 is non-lithophysal Tiva Canyon Member (hackly and columnar field subdivisions), about 35 ft thick, underlain by the non-welded shardy base

(basal field subdivision) (Hammermeister, D., written commun., 1985). Velocity layer 3 corresponds to the weathered and(or) fractured densely-welded tuff and layer 4 to non-weathered densely-welded tuff or the lower, non-welded unit.

#### Seismic line NDW2

The line is located in the approximate center of Pagany Wash, 0.10 miles from the end of the south-eastern wall of the wash. Three velocity layers are indicated by the time-distance graph (fig. 27). Seismic velocities and depths are shown in table 6. Layer 2 has the greatest velocity for alluvium encountered in Pagany Wash. This is attributed to increased compaction with depth.

A depth plot is shown as figure 28. There are not any boreholes in the near area for depth correlation, however, access holes drilled in the center of Pagany Wash, both above and below NDW2 have bedrock contacts between 44 ft and 49 ft.

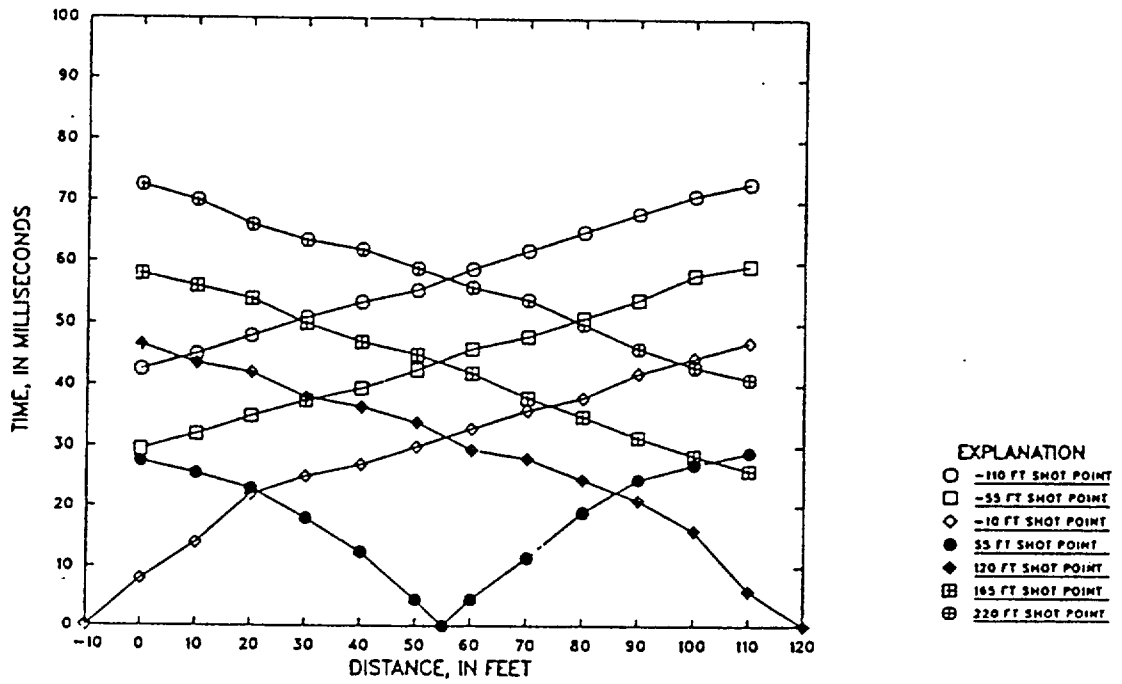


Figure 27.--Time-distance graph for seismic line NDW2.

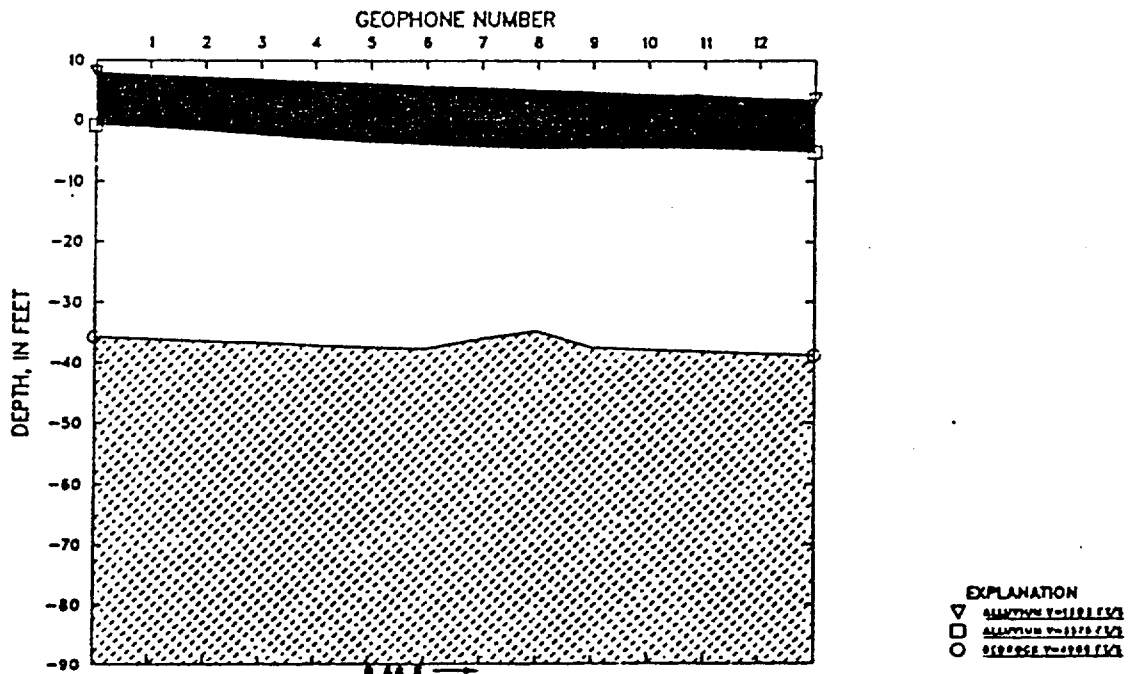


Figure 28.--Depth plot, line NDW2.

Table 6.--Seismic velocities and depths, line NDW2.

Layer number	Layer velocity		Geologic description			
1	1303 ft/s		alluvium			
2	3576 ft/s		alluvium			
3	4909 ft/s		bedrock			
Position of Layers Beneath Shotpoints and Geophones						
SP	Position	Surface Elev	Layer 2		Layer 3	
			Depth	Elev	Depth	Elev
C	-10.0	8.0	8.9	-0.9	43.8	-35.8
D	55.0	5.8	10.0	-4.2	42.8	-37.0
E	120.0	3.5	8.7	-5.2	42.4	-38.9
GEO						
1	0.0	7.6	8.9	-1.3	43.7	-36.1
2	10.0	7.3	9.1	-1.8	43.8	-36.5
3	20.0	7.0	9.5	-2.5	43.8	-36.8
4	30.0	6.6	9.7	-3.1	43.8	-37.2
5	40.0	6.3	9.9	-3.6	43.8	-37.5
6	50.0	5.9	9.9	-4.0	43.7	-37.8
7	60.0	5.6	10.0	-4.4	41.7	-36.1
8	70.0	5.2	9.8	-4.6	40.0	-34.8
9	80.0	4.9	9.4	-4.5	42.4	-37.5
10	90.0	4.5	9.0	-4.5	42.4	-37.9
11	100.0	4.2	8.8	-4.6	42.4	-38.2
12	110.0	3.8	8.7	-4.9	42.4	-38.6

## Qac Canyon

Several seismic lines were surveyed in this wash. This was the first area surveyed, and much unusable data was acquired during the time that survey techniques and line location skills were being learned. Limitations of the sledgehammer refraction method for obtaining layer depth information in arid, alluvium-filled washes were learned in this study area.

### Seismic line Qac 14

Line location (fig. 29) is approximately two feet north of and parallel to a well-established jeep trail. The area contains debris piles of welded tuff and several rodent habitats and tunnels. Slope is 2 degrees. Four velocity layers are present (fig. 30).

Depths to velocity layers (table 7) are shown as Figure 31.

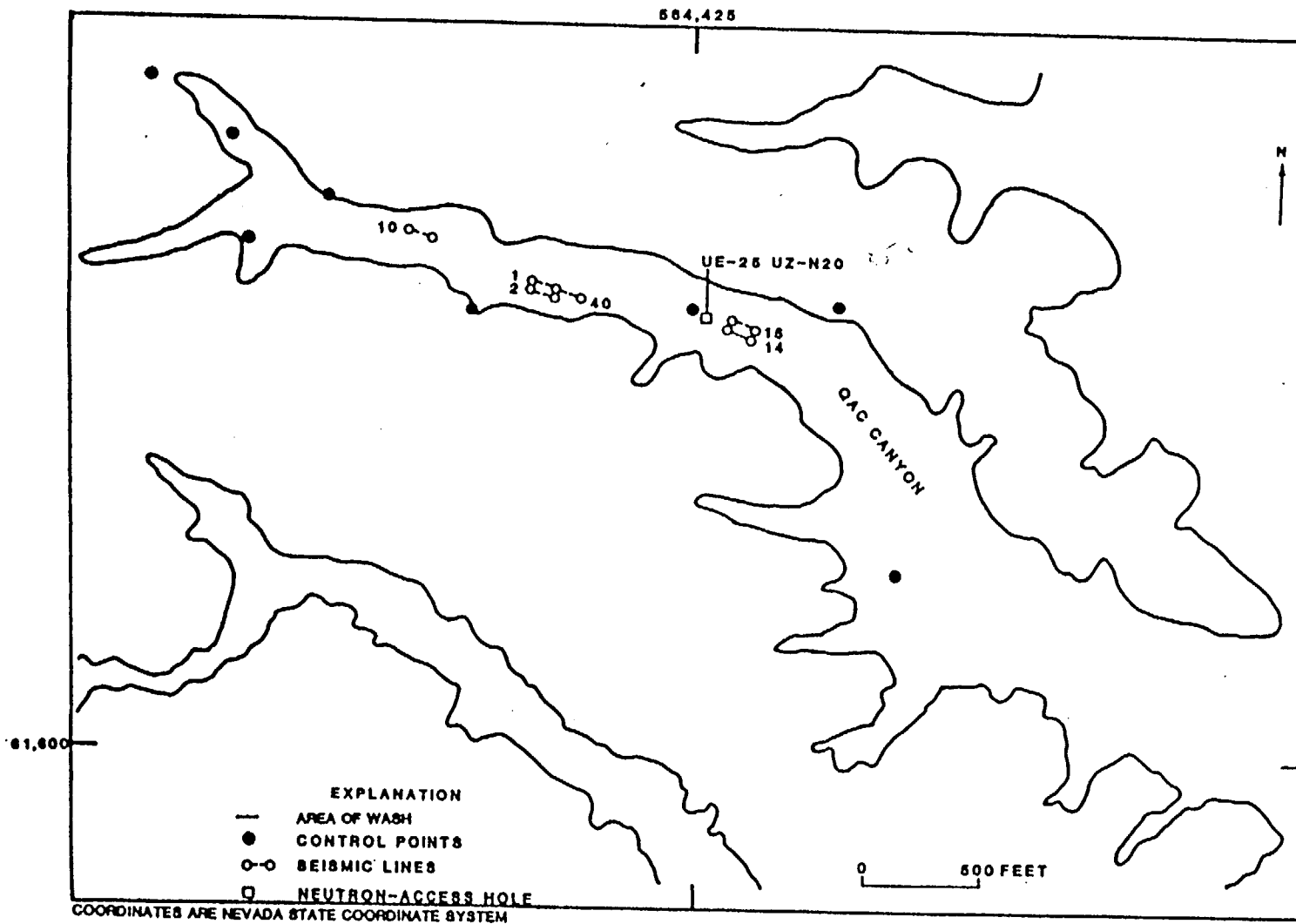


Figure 29.--Map showing location of seismic lines in Qac Canyon.

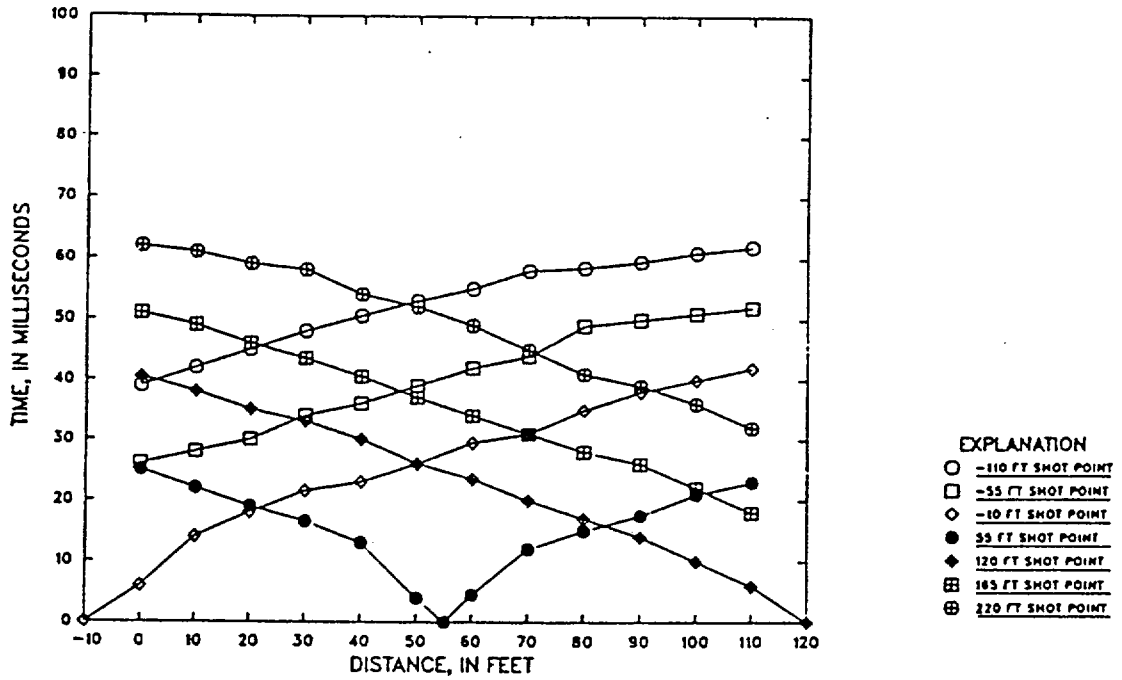


Figure 30.--Time-distance graph for seismic line Qac14.

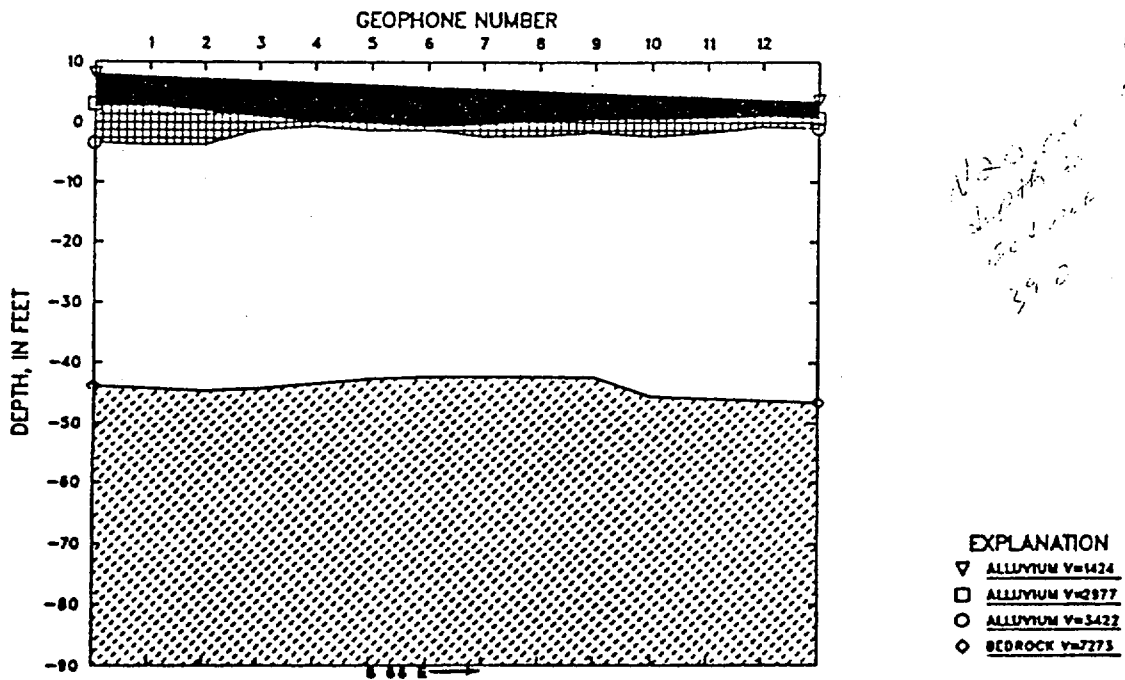


Figure 31.--Depth plot, line Qac14.

Table 7.--Seismic velocities and depths, line Qac14.

Layer number		Layer velocity							
1		1424 ft/s							
2		2977 ft/s							
3		3422 ft/s							
4		7273 ft/s							

Position of Layers Beneath Shotpoints and Geophones									
SP	Position	Surface Elev	Layer 2		Layer 3		Layer 4		
			Depth	Elev	Depth	Elev	Depth	Elev	
C	-10.0	8.0	5.0	3.0	11.5	-3.5	51.9	-43.9	
D	55.0	5.8	6.3	-0.5	7.7	-1.9	48.1	-42.3	
E	120.0	3.5	2.8	0.7	4.6	-1.1	50.0	-46.5	
GEO									
1	0.0	7.6	4.9	2.7	11.4	-3.8	51.8	-44.2	
2	10.0	7.3	5.4	1.9	11.1	-3.8	51.9	-44.6	
3	20.0	7.0	6.1	0.9	8.3	-1.3	51.2	-44.2	
4	30.0	6.6	6.4	0.2	7.3	-0.7	50.0	-43.4	
5	40.0	6.3	6.5	-0.2	7.7	-1.4	48.9	-42.6	
6	50.0	5.9	6.6	-0.7	7.3	-1.4	48.2	-42.3	
7	60.0	5.6	6.0	-0.4	8.0	-2.4	47.9	-42.3	
8	70.0	5.2	4.9	0.3	7.5	-2.3	47.5	-42.3	
9	80.0	4.9	4.4	0.5	6.7	-1.8	47.2	-42.3	
10	90.0	4.5	4.0	0.5	6.9	-2.4	50.0	-45.5	
11	100.0	4.2	3.5	0.7	6.0	-1.8	50.0	-45.8	
12	110.0	3.8	2.8	1.0	4.6	-0.8	50.0	-46.2	

## Seismic Line Qac15

Line Qac15 is located 55 ft, N 25 E (90 degrees) of line Qac14. The line is 177 ft from the north wall of the wash and runs approximately parallel to it. Three velocity layers are identifiable (fig. 32). Seismic velocities and depths are shown in table 8.

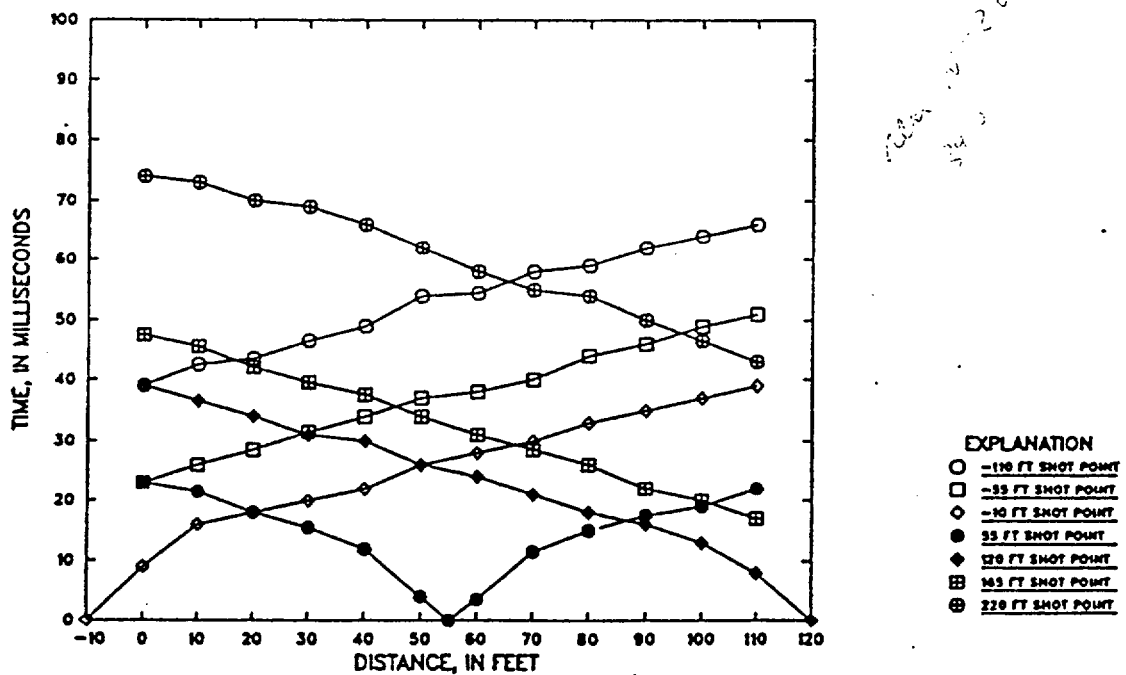


Figure 32.--Time-distance graph for seismic line Qac15.

Table 8.--Seismic velocities and depths, line Qac15.

Layer number		Layer velocity			
1		1266 ft/s			
2		3876 ft/s			
3		4760 ft/s			

Position of Layers Beneath Shotpoints and Geophones						
SP	Position	Surface Elev	Layer 2		Layer 3	
			Depth	Elev	Depth	Elev
C	-10.0	8.0	6.4	1.6	31.5	-23.5
D	55.0	5.8	6.5	-0.7	32.8	-27.0
E	120.0	3.5	4.4	-0.9	34.9	-31.4
GEO						
1	0.0	7.6	6.4	1.2	31.5	-23.9
2	10.0	7.3	6.5	0.8	31.5	-24.2
3	20.0	7.0	6.3	0.7	30.9	-23.9
4	30.0	6.6	6.4	0.2	30.4	-23.8
5	40.0	6.3	6.9	-0.6	31.6	-25.3
6	50.0	5.9	6.7	-0.8	32.7	-26.8
7	60.0	5.6	6.1	-0.5	32.8	-27.2
8	70.0	5.2	5.7	-0.5	34.9	-29.7
9	80.0	4.9	5.9	-1.0	34.9	-30.0
10	90.0	4.5	5.3	-0.8	34.9	-30.4
11	100.0	4.2	4.7	-0.5	34.9	-30.7
12	110.0	3.8	4.4	-0.6	34.9	-31.1

A depth plot is shown as figure 33.

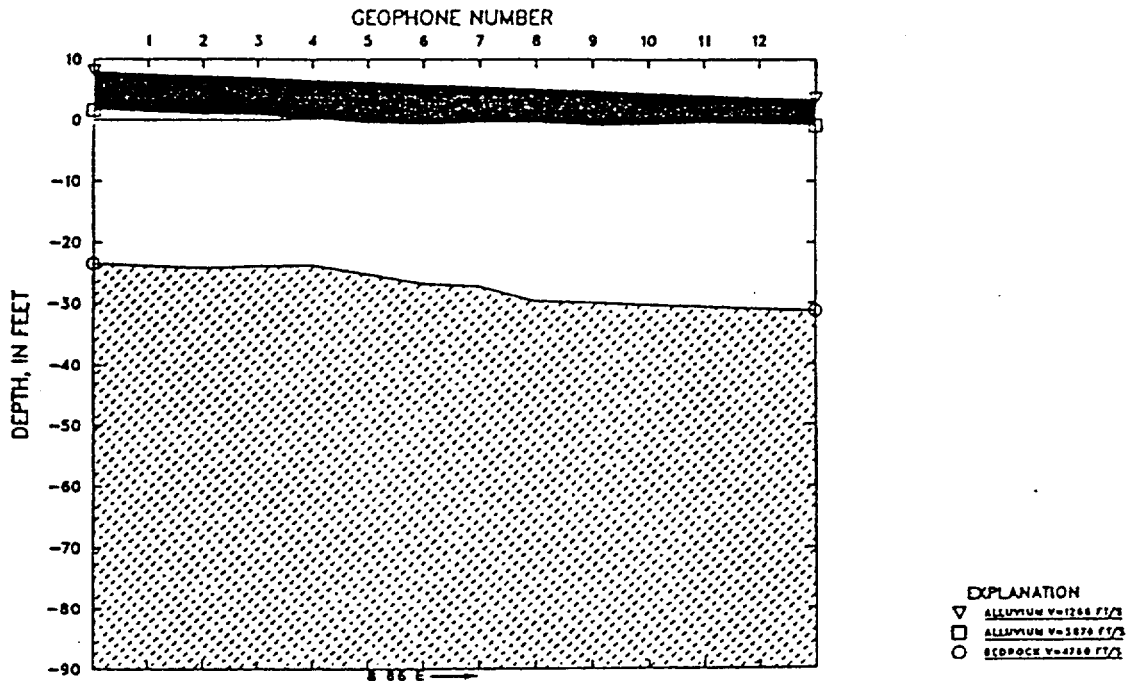


Figure 33.--Depth plot, line Qac15.

Velocity layers 1 and 2 beneath Qac14 and Qac15 can be related to surface materials that are transported by modern vehicles, water, and animals. Neutron-moisture logs from UE-25 UZ-N20 (Fig. 29) indicate a zone of increasing moisture that peaks between 6 and 7 ft below land surface (Hammermeister, written commun., 1985). This type of change in moisture content and increasing compaction with depth may be related to the velocity changes between layers of alluvium.

Neutron-access hole UE-25 UZ-N20 is located 61 ft, N55W (up-slope) of geophone #1, line Qac14. Layer 4, line Qac14, corresponds to the Tiva Canyon Member. The seismic velocity, 7,273 ft/s, is greater than

was determined at all other sites in the wash and may be due to a lower degree of weathering. Qac14 is located near the center of the wash where early alluvial deposits may have accumulated and protected the bedrock surface. The seismic velocity of layer 3, line Qac15 is within the range of bedrock velocities determined from NDW1, NDW2, and NDW3. The corresponding depth of about 33 ft agrees with field estimates of the change in depth to bedrock as the wall of the wash is approached.

#### Seismic Lines Qac1 and Qac40

Lines Qac1 and Qac40 were laid out end-to-end: geophone #12 for Qac1 was the location of geophone #1 for Qac40. Because of the limited amount of clear area, 110 ft offset shotpoints were not used, therefore total line length was 330 ft. Layer designations for each line were determined from separate time-distance graphs. Data from each line was then combined to form a single input file for the SIPT program.

Shotpoints A through E are from line Qac1. Shotpoints F through J are from line Qac40. Because each line had a shared geophone position, there are 23 geophone positions rather than 24. Geophones #1 through #12 are from line Qac1. Geophones #13 through #23 are from line Qac40. The combined time-distance graph (fig. 34) indicated three velocity layers. Seismic velocities and depths are shown in table 9.

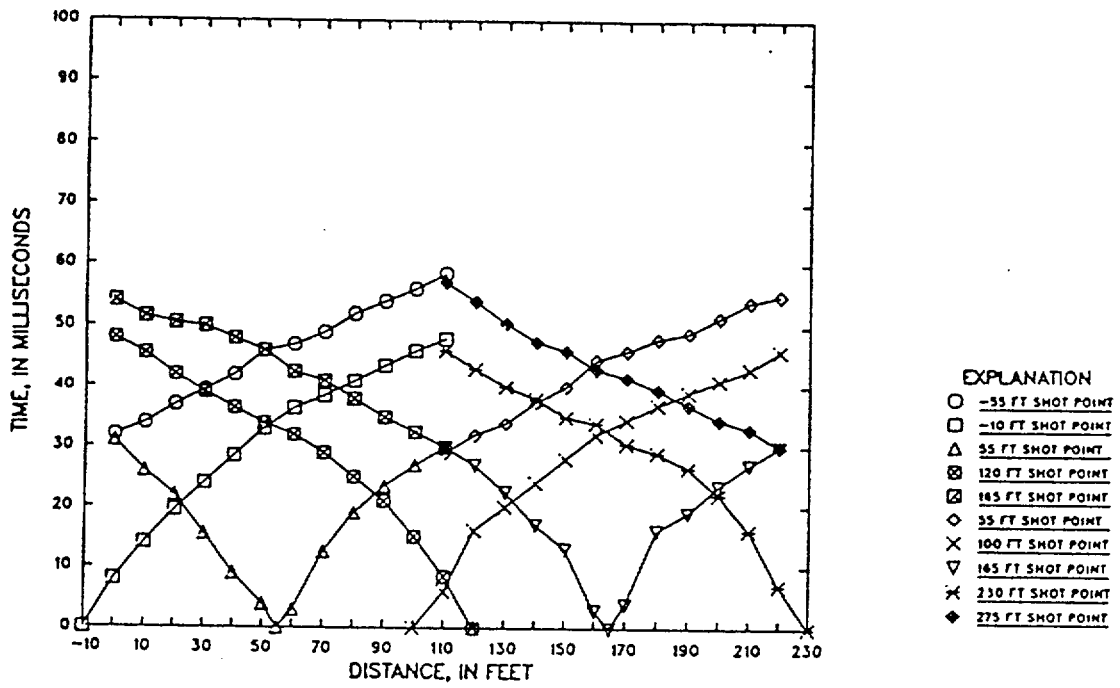


Figure 34.--Combined time-distance graph for seismic lines Qac1 and Qac40.

The depth plot (fig. 35) shows a 7.6-ft change in bedrock elevation beneath geophones #22 and #23. A field study was not made to account for this feature, however, it could represent a buried drainage channel or a terrace-like change in bedrock elevation. At least one more seismic survey, continuing from the end of line Qac40, would be required to determine the extent of this feature.

Table 9.--Seismic velocities and depths, lines Qac1 and Qac40.

Layer number	Layer velocity		Geologic description			
1	1402 ft/s		alluvium			
2	2792 ft/s		alluvium			
3	4578 ft/s		bedrock			

Position of Layers Beneath Shotpoints and Geophones						
SP	Position	Surface Elev	Layer 2		Layer 3	
			Depth	Elev	Depth	Elev
B	-10.0	9.9	9.9	-0.0	19.3	-9.4
C	55.0	7.7	8.1	-0.4	25.2	-17.5
G	100.0	6.1	8.5	-2.4	27.4	-21.3
D	120.0	5.4	9.0	-3.6	24.6	-19.2
H	165.0	3.8	6.9	-3.1	20.7	-16.9
I	230.0	1.6	9.2	-7.6	24.7	-23.1
GEO						
1	0.0	9.6	10.0	-0.4	19.3	-9.7
2	10.0	9.3	10.2	-0.9	19.0	-9.7
3	20.0	8.9	9.9	-1.0	19.1	-10.2
4	30.0	8.5	9.1	-0.5	21.3	-12.8
5	40.0	8.2	8.0	0.2	23.6	-15.4
6	50.0	7.9	7.4	0.5	24.7	-16.9
7	60.0	7.5	8.7	-1.2	25.6	-18.1
8	70.0	7.1	8.1	-1.0	27.3	-20.2
9	80.0	6.8	7.9	-1.1	27.0	-20.2
10	90.0	6.5	8.3	-1.8	27.4	-20.9
11	100.0	6.1	8.5	-2.4	27.4	-21.3
12	110.0	5.8	8.8	-3.0	25.4	-19.6
13	120.0	5.4	9.0	-3.6	24.6	-19.2
14	130.0	5.1	9.1	-4.0	24.0	-18.9
15	140.0	4.7	8.4	-3.7	22.8	-18.1
16	150.0	4.4	7.4	-3.0	21.5	-17.1
17	160.0	4.0	6.4	-2.4	20.7	-16.7
18	170.0	3.7	7.6	-3.9	20.8	-17.1
19	180.0	3.3	8.3	-5.0	19.6	-16.3
20	190.0	3.0	9.1	-6.1	18.5	-15.5
21	200.0	2.6	9.6	-7.0	17.5	-14.9
22	210.0	2.3	9.6	-7.3	17.4	-15.1
23	220.0	1.9	9.2	-7.3	24.6	-22.7

The depth model obtained from these lines cannot be verified by borehole data. Seismic data obtained from Qac1 and Qac40 were first analyzed as single seismic lines. Velocities obtained were within a 10-percent range. Depth to layer 3 beneath geophone #12, line Qac1, was the same depth obtained beneath geophone #1, line Qac40 (25.0 ft). Velocities determined from Qac14 and Qac15 were used as the delineating factor between alluvium and bedrock. The results from this survey were then compared with results from a nearby seismic line, Qac2.

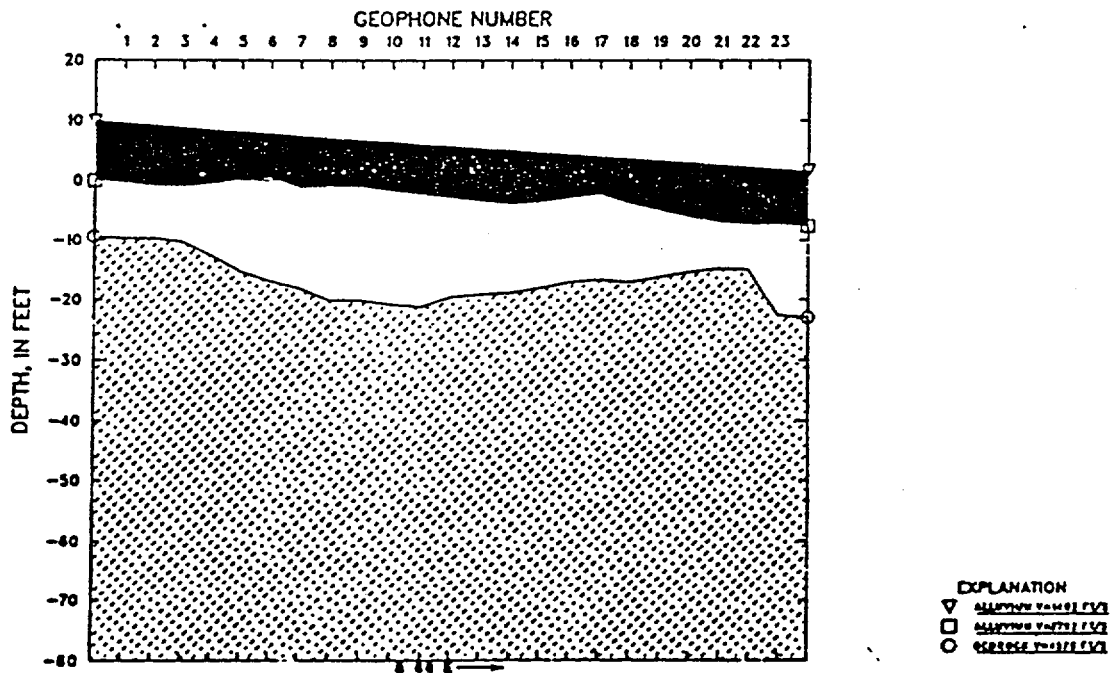


Figure 35.--Depth plot, lines Qac1 and Qac40.

## Seismic Line Qac2

Line Qac2 is located 45 ft due south of line Qac1: geophone locations and shotpoints for Qac2 are parallel to those for Qac1. Three velocity layers are present (fig. 36). Seismic velocities and depths are shown in table 10.

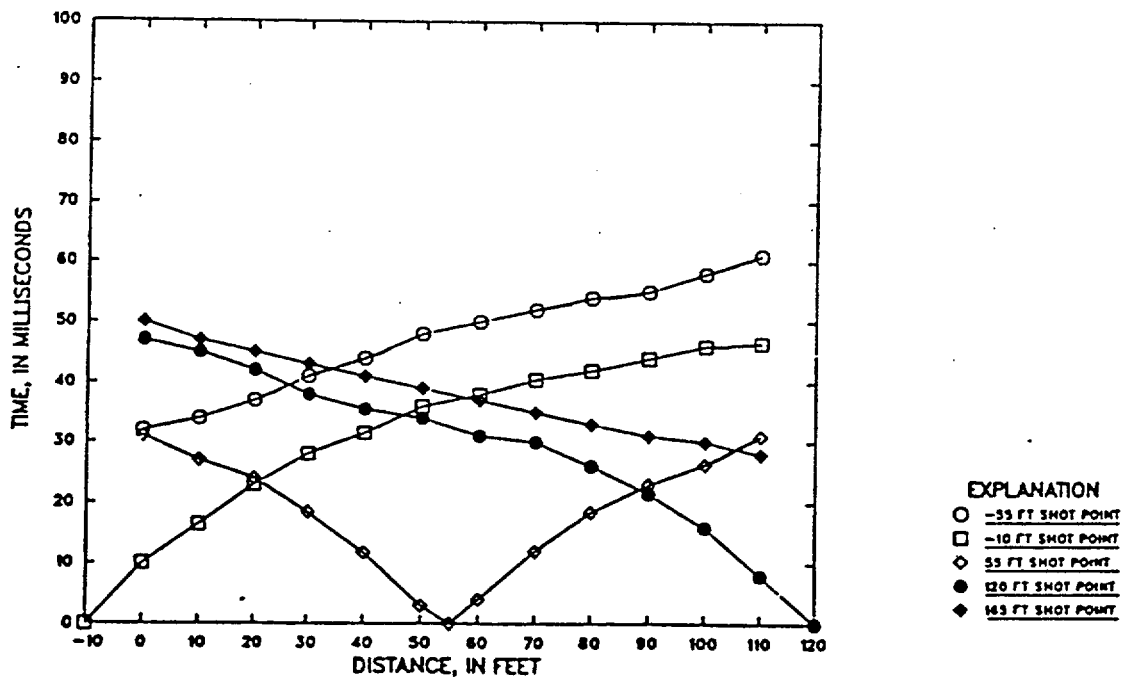


Figure 36.--Time-distance graph for seismic line Qac2.

Table 10.--Seismic velocities and depths, line Qac2.

Layer number	Layer velocity		Geologic description			
1	1282 ft/s		alluvium			
2	2795 ft/s		alluvium			
3	4881 ft/s		bedrock			

Position of Layers Beneath Shotpoints and Geophones						
SP	Position	Surface Elev	Layer 2		Layer 3	
			Depth	Elev	Depth	Elev
B	-10.0	9.2	9.0	0.2	28.0	-18.8
C	55.0	5.8	7.7	-1.9	22.7	-16.9
D	120.0	2.4	8.3	-5.9	23.2	-20.8
GEO						
1	0.0	8.6	9.0	-0.4	28.0	-19.4
2	10.0	8.1	8.6	-0.5	27.5	-19.4
3	20.0	7.6	8.5	-0.9	24.8	-17.2
4	30.0	7.1	8.5	-1.4	23.6	-16.5
5	40.0	6.5	8.3	-1.8	22.8	-16.3
6	50.0	6.0	8.1	-2.1	22.8	-16.8
7	60.0	5.5	7.2	-1.7	22.4	-16.9
8	70.0	5.0	8.1	-3.1	21.9	-16.9
9	80.0	4.5	8.9	-4.4	22.5	-18.0
10	90.0	3.9	9.1	-5.2	22.4	-18.5
11	100.0	3.4	8.8	-5.4	22.2	-18.8
12	110.0	2.9	8.3	-5.4	23.2	-20.3

Layer velocities correspond with the velocities obtained from Qac1 and Qac15 within 10 percent.

The depth plot is shown as figure 37. Comparing depth plots obtained from lines Qac1 and Qac2, the alluvial layers thicken and thin to a similar degree beneath corresponding geophones.

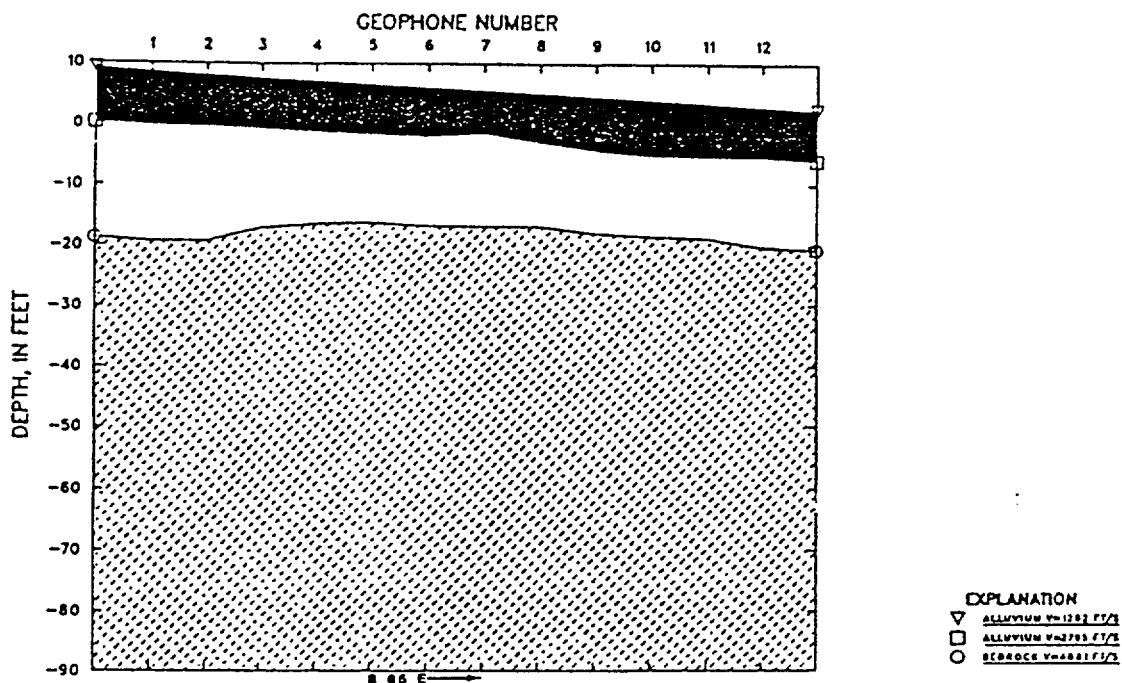


Figure 37.--Depth plot, line Qac2.

#### Seismic Line Qac10

Geophones #1 through #4 were located near a 3-ft channel cut: geophones #5 through #12 were near a 6-ft channel cut. The time-distance graph (fig. 38) indicated three velocity layers. Seismic velocities and depths are shown in table 11.

→ The contact between alluvium and bedrock was determined from the velocity contrast between layers 2 and 3 (fig. 39).

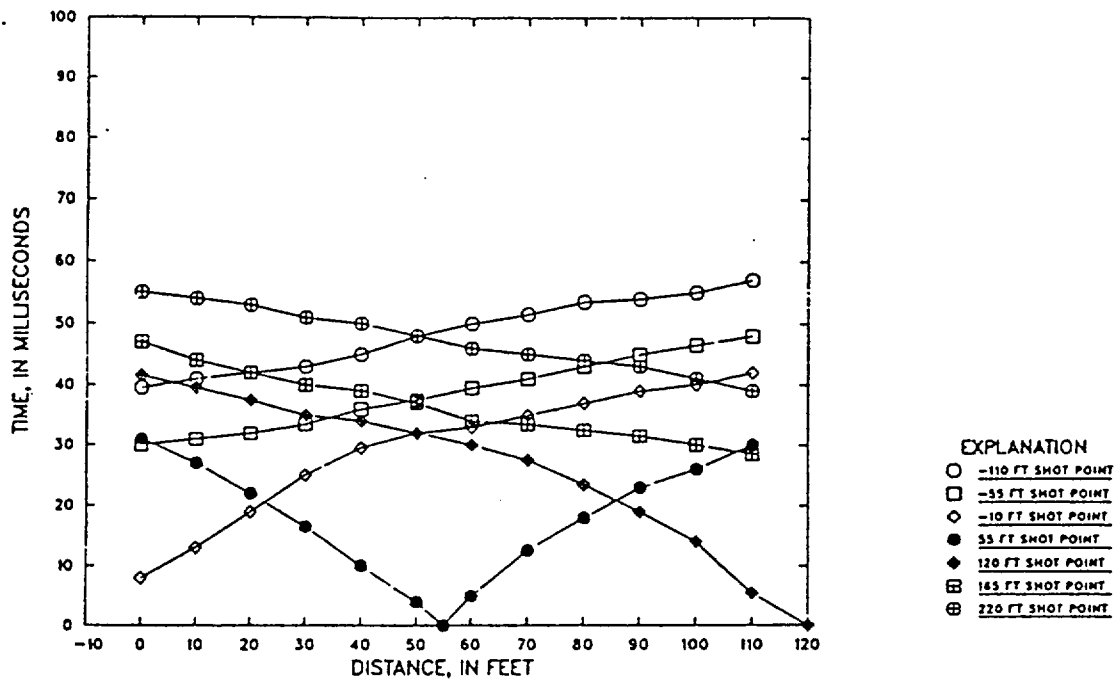


Figure 38.--Time-distance graph for seismic line Qac10.

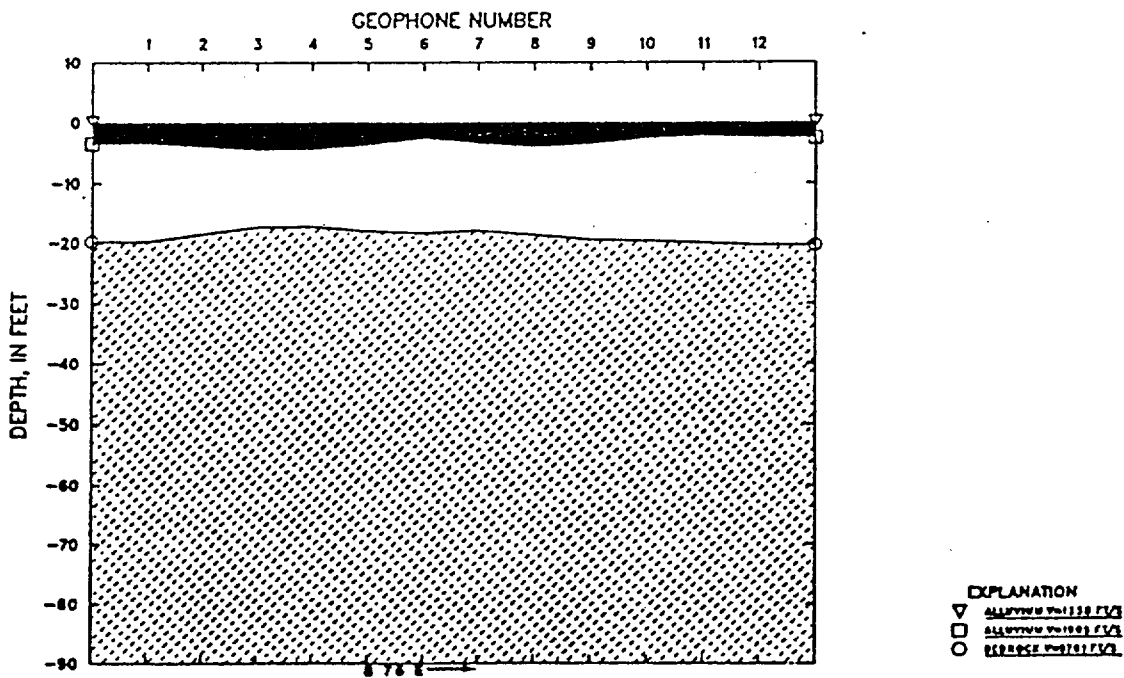


Figure 39.--Depth plot, line Qac10.

Table 11.--Seismic velocities and depths, line Qac10.

Layer number	Layer velocity		Geologic description			
1	1330 ft/s		alluvium			
2	1878 ft/s		alluvium			
3	5753 ft/s		bedrock			

Position of Layers Beneath Shotpoints and Geophones							
SP	Position	Surface Elev	Layer 2		Layer 3		
			Depth	Elev	Depth	Elev	
C	-10.0	8.0	3.3	4.7	19.6	-11.6	
D	55.0	5.8	2.8	3.0	18.2	-12.4	
E	120.0	3.5	2.2	1.3	20.4	-16.9	
GEO							
1	0.0	7.6	3.3	4.3	19.5	-11.9	
2	10.0	7.3	3.8	3.5	18.3	-11.0	
3	20.0	7.0	4.4	2.6	17.2	-10.2	
4	30.0	6.6	4.2	2.4	17.2	-10.6	
5	40.0	6.3	3.3	3.0	18.0	-11.7	
6	50.0	5.9	2.6	3.3	18.2	-12.3	
7	60.0	5.6	3.0	2.6	18.1	-12.5	
8	70.0	5.2	2.4	2.8	19.0	-13.8	
9	80.0	4.9	1.9	3.0	19.4	-14.5	
10	90.0	4.5	1.1	3.4	19.6	-15.1	
11	100.0	4.2	1.6	2.6	20.0	-15.8	
12	110.0	3.8	2.2	1.6	20.4	-16.6	

## WT2 Wash

The study area consisted of two branches that merged with the trunk of the wash (fig. 40). Compacted, dirt road beds extend the length of the wash trunk and the branches.

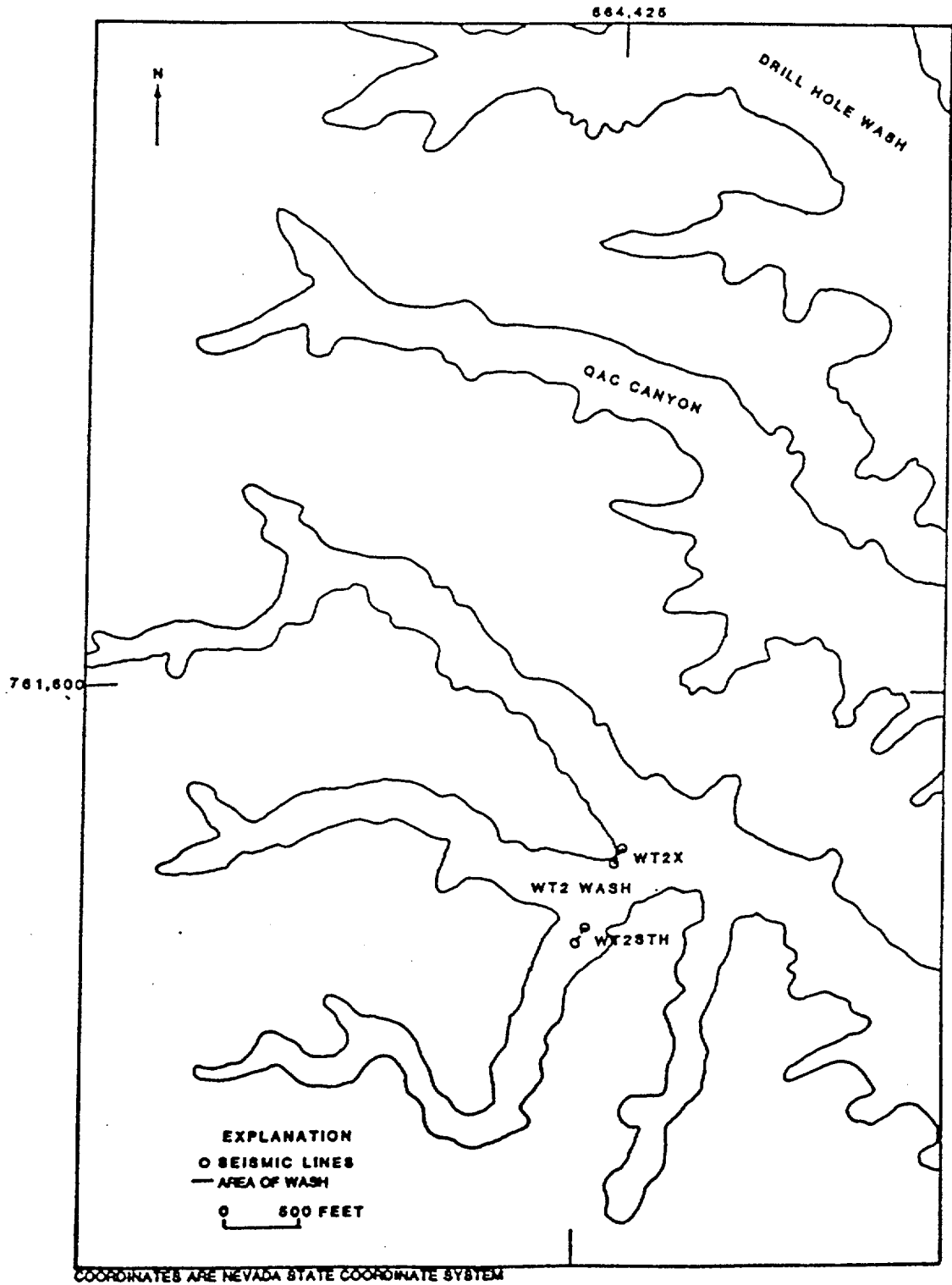


Figure 40.--Map showing location of seismic lines in WT2 Wash.

## Seismic Line WT2X

The line was located on the eastern border of a dirt road. The road was located at the intersection of a bedrock spur and land surface. Three velocity layers were identified on the time-distance graph (fig. 41). Seismic velocities and depths are shown in table 12.

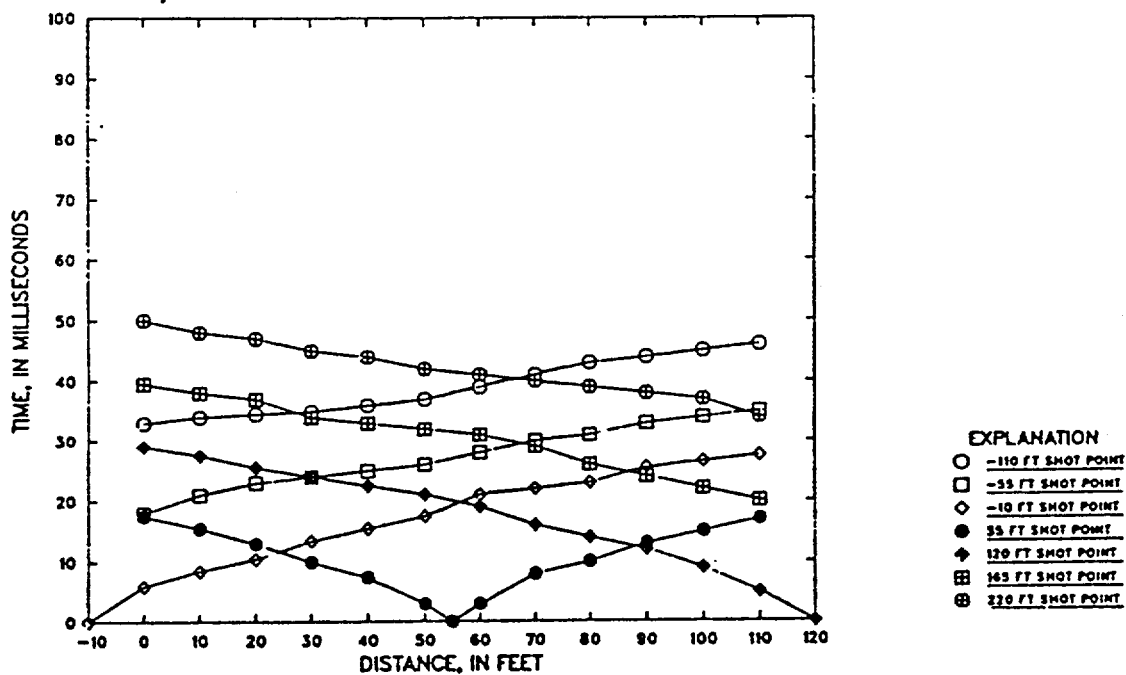


Figure 41.--Time-distance graph for seismic line WT2X.

Table 12.--Seismic velocities and depths, line WT2X.

Layer number	Layer velocity		Geologic description			
1	1750 ft/s		alluvium			
2	4180 ft/s		bedrock			
3	7459 ft/s		bedrock			

Position of Layers Beneath Shotpoints and Geophones							
SP	Position	Surface Elev	Layer 2		Layer 3		
			Depth	Elev	Depth	Elev	
C	-10.0	0.0	4.2	-4.2	23.3	-23.3	
D	55.0	0.0	3.4	-3.4	20.8	-20.8	
E	120.0	0.0	4.3	-4.3	22.9	-22.9	
GEO							
1	0.0	0.0	4.2	-4.2	23.3	-23.3	
2	10.0	0.0	4.3	-4.3	21.5	-21.5	
3	20.0	0.0	4.2	-4.2	21.6	-21.6	
4	30.0	0.0	4.1	-4.1	21.6	-21.6	
5	40.0	0.0	3.6	-3.6	21.0	-21.0	
6	50.0	0.0	3.3	-3.3	20.7	-20.7	
7	60.0	0.0	3.5	-3.5	21.0	-21.0	
8	70.0	0.0	3.7	-3.7	21.6	-21.6	
9	80.0	0.0	3.5	-3.5	21.9	-21.9	
10	90.0	0.0	4.0	-4.0	21.6	-21.6	
11	100.0	0.0	4.0	-4.0	21.4	-21.4	
12	110.0	0.0	4.3	-4.3	22.9	-22.9	

The depth model (fig. 42) can reasonably be verified by local geology. The small rise in bedrock elevation shown in the cross section, corresponds with the bedrock spur.

The seismic velocities of layers 2 and 3 represent the general range of velocities that have been attributed to bedrock. Because of the shallow depths to layers, a borehole along this line could be drilled to directly determine the accuracy of layer assignments.

*for 1/2  
check  
with  
hand*

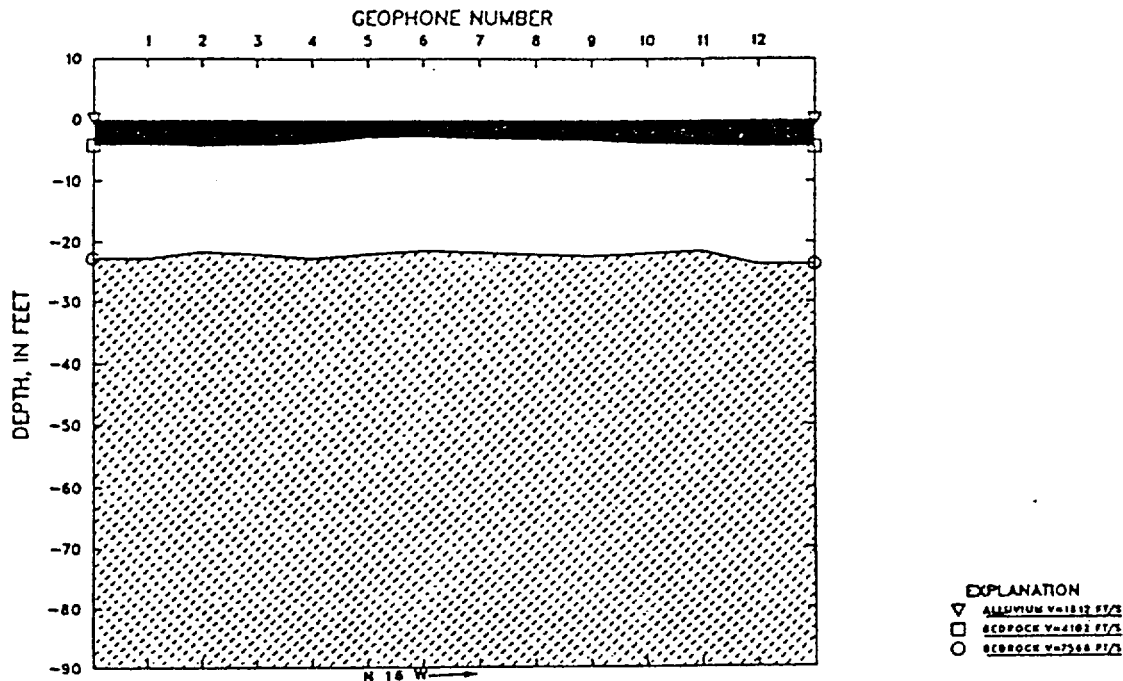


Figure 42.--Depth plot, line WT2X.

#### Seismic Line WT2STH

Line location was near the base of a branch, where it merged with the trunk of the wash. Data acquired from reverse shotpoints did not show distinct first arrivals. This was due to noise from machinery operating in the area and perhaps the merging of the wash branch with the trunk of the wash. Using forward and interior shotpoints only, three velocity layers were indicated from the time-distance graph (fig. 43). Seismic velocities and depths are shown in table 13.

The depth plot is shown as figure 44. Beneath geophone #8, layers 2 and 3 merge to form a single layer. This fault(?) in the data interpretation probably is the result of the lack of reversed data. Depths to bedrock beneath geophones #1 through #7 are reasonable. It was expected that the depth to bedrock would increase towards the base of the wash, however, the results obtained and the lack of reversed data make it difficult to assign layer depths with confidence. Results from this survey do point out the necessity of reversed data when interpreting seismic data from areas with irregular and dipping refractors.

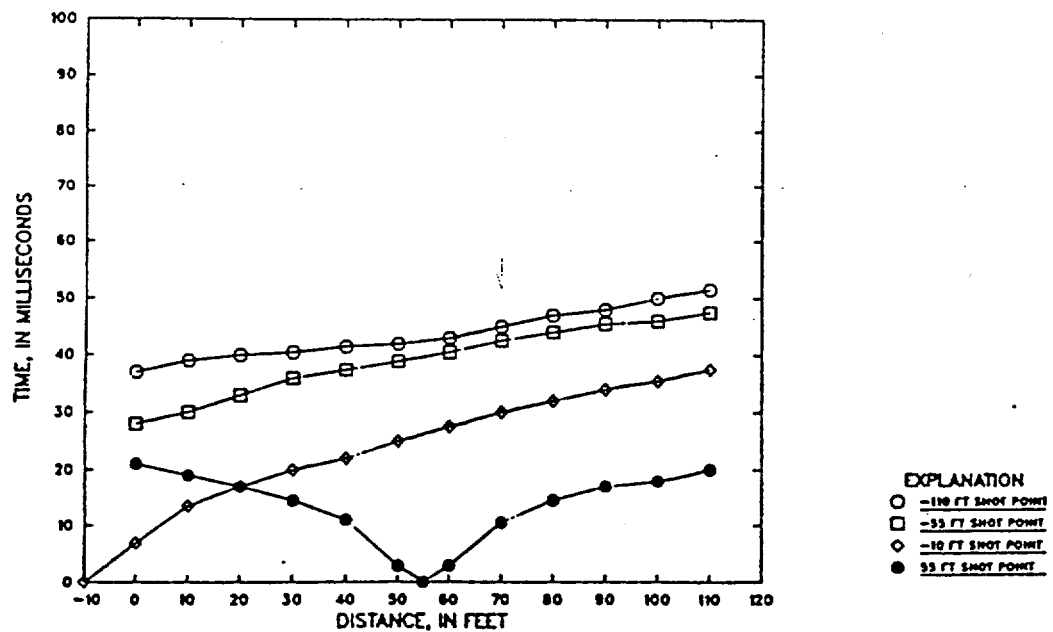


Figure 43.--Time-distance graph for seismic line WT2STH.

Table 13.--Seismic velocities and depths, line WT2STH.

Layer number	Layer velocity		Geologic description			
1	1510 ft/s		alluvium			
2	4306 ft/s		bedrock			
3	6876 ft/s		bedrock			

Position of Layers Beneath Shotpoints and Geophones							
SP	Position	Surface Elev	Layer 2		Layer 3		
			Depth	Elev	Depth	Elev	
C	-10.0	8.4	7.3	1.1	33.8	-25.4	
D	55.0	3.8	11.9	-8.1	24.7	-20.9	
GEO							
1	0.0	7.7	7.3	0.4	33.8	-26.1	
2	10.0	7.0	7.5	-0.5	33.2	-26.2	
3	20.0	6.3	8.1	-1.8	32.0	-25.7	
4	30.0	5.6	8.7	-3.1	30.8	-25.2	
5	40.0	4.9	9.3	-4.4	29.6	-24.7	
6	50.0	4.2	10.0	-5.8	27.0	-22.8	
7	60.0	3.5	13.9	-10.4	22.5	-19.0	
8	70.0	2.8	20.4	-17.6	20.4	-17.6	
9	80.0	2.1	30.6	-28.5	30.6	-28.5	
10	90.0	1.4	36.2	-34.8	36.2	-34.8	
11	100.0	0.7	36.2	-35.5	36.2	-35.5	
12	110.0	0.0	36.2	-36.2	36.2	-36.2	

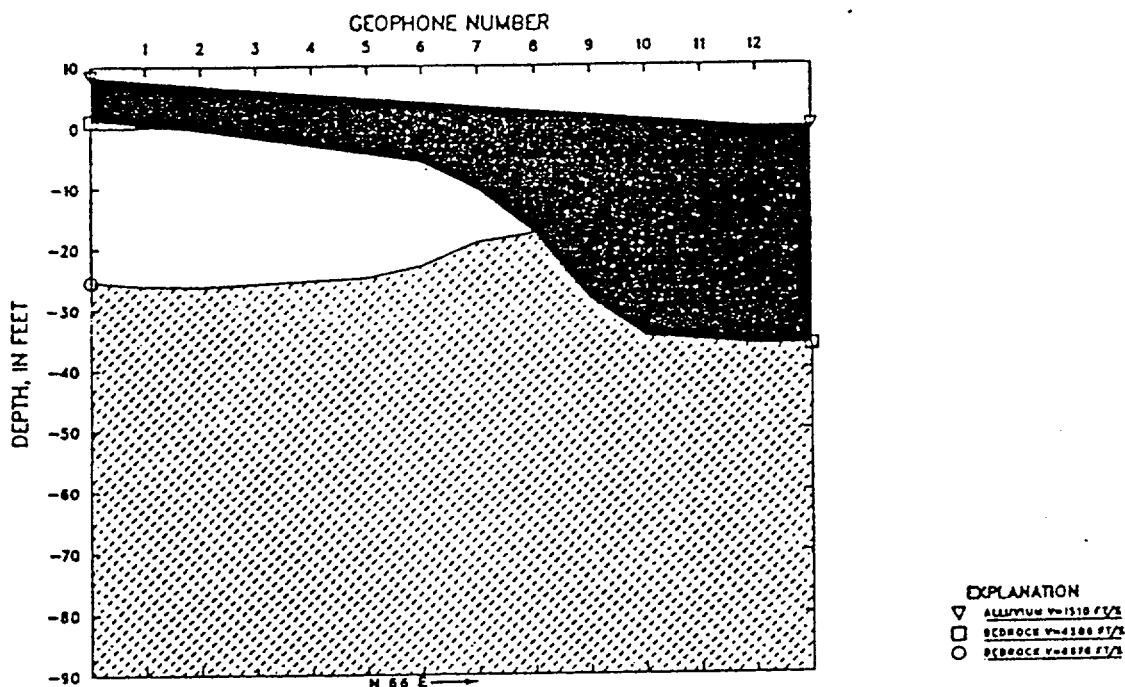


Figure 44.--Depth plot, line WT2STH.

In each of the study areas, at least one other seismic line was surveyed. Data interpretations were not possible or presented because of uncertain first arrival times. Uncertainties were the result of high levels of noise that masked compressional wave traces and(or) weak signals that had no distinct break in slope.

Data records obtained from upper wash locations (most proximal to Yucca Mountain) contained much noise. [Upper washes are characterized by narrow width, steep walls, and deep channel cuts.] Seismic noise was attributed to interception of signals by the walls, the presence of large boulders, and the unconsolidated state of surface sediments. Data records from lower wash locations (most distal from Yucca Mountain) were

of poor quality because of noise, low-amplitude compressional wave traces, and distortion of the printed wave traces. Seismic noise and signal dispersion was attributed to wind, animal burrows, the unconsolidated state of surface sediments, and perhaps, increased stratification within the alluvial layers due to the relatively high-deposition environment. To obtain distinct first arrivals at difficult sites or from offset distances, several shots per data record were required. In theory, first arrivals should become more pronounced with each additional shot, while noise signals cancel out. In several surveys this was the case. In the lower washes however, more than 20 shots per seismic record were required and the additional shots produced unreadable records. Wave traces were large in amplitude and irregular over the entire time period recorded; first arrivals could not be distinguished from the background.

Seismic noise was primarily caused by: (1) Dry and unconsolidated surface sediments that lessen the strength of seismic signals through decreased coupling of the sediment grains and increased gas-filled void space, and (2) wind that caused the geophones to vibrate and sense non-seismic vertical motion. To minimize the effects of these two phenomena, methods for emplacing geophones and setting the strike plate were established.  Geophones were firmly placed in the surface sediments, a small amount of water was poured over them to increase ground-to-geophone coupling, and then each geophone was covered with local surface sediments. At each measured shotpoint, ground surface was broken with a pick and the sediments tilled. Rock fragments and debris were removed until an area slightly larger than that of the plate was

clear. The strike plate was placed in the cleared area and hit with a hammer until it was well-seated. Where the clear area was very dry and loose, a small amount of water was poured around the perimeter of the strike plate to increase ground-to-plate coupling. These techniques did improve the quality of first arrivals recorded from mid-wash seismic line locations, however, first arrivals from upper and lower wash locations remained masked by noise or distorted.

A histogram of observed P wave velocities versus each occurrence is shown as Figure 45. Based on extrapolation of borehole data, compressional wave velocity in alluvium was always less than 4,000 ft/s; velocities in bedrock were always greater than 4,000 ft/s. Boreholes on which seismic layer assignments were based, were always less than 70 ft up or down slope from seismic lines. Preliminary density logs have shown that a significant density contrast exists between alluvium and bedrock, therefore, the bedrock surface was not considered to be a hidden layer and velocity values are considered accurate within the limits of the seismic refraction method.

#### SUMMARY AND CONCLUSIONS

The sledgehammer seismic refraction method has been used to determine overburden thickness in arid, alluvium-filled washes near Yucca Mountain, Nevada. Seismic and borehole data are compatible in the study areas. It is therefore concluded that this technique can be used successfully in the washes associated with Yucca Mountain, where thickness of alluvium is generally less than 70 ft. Application of this

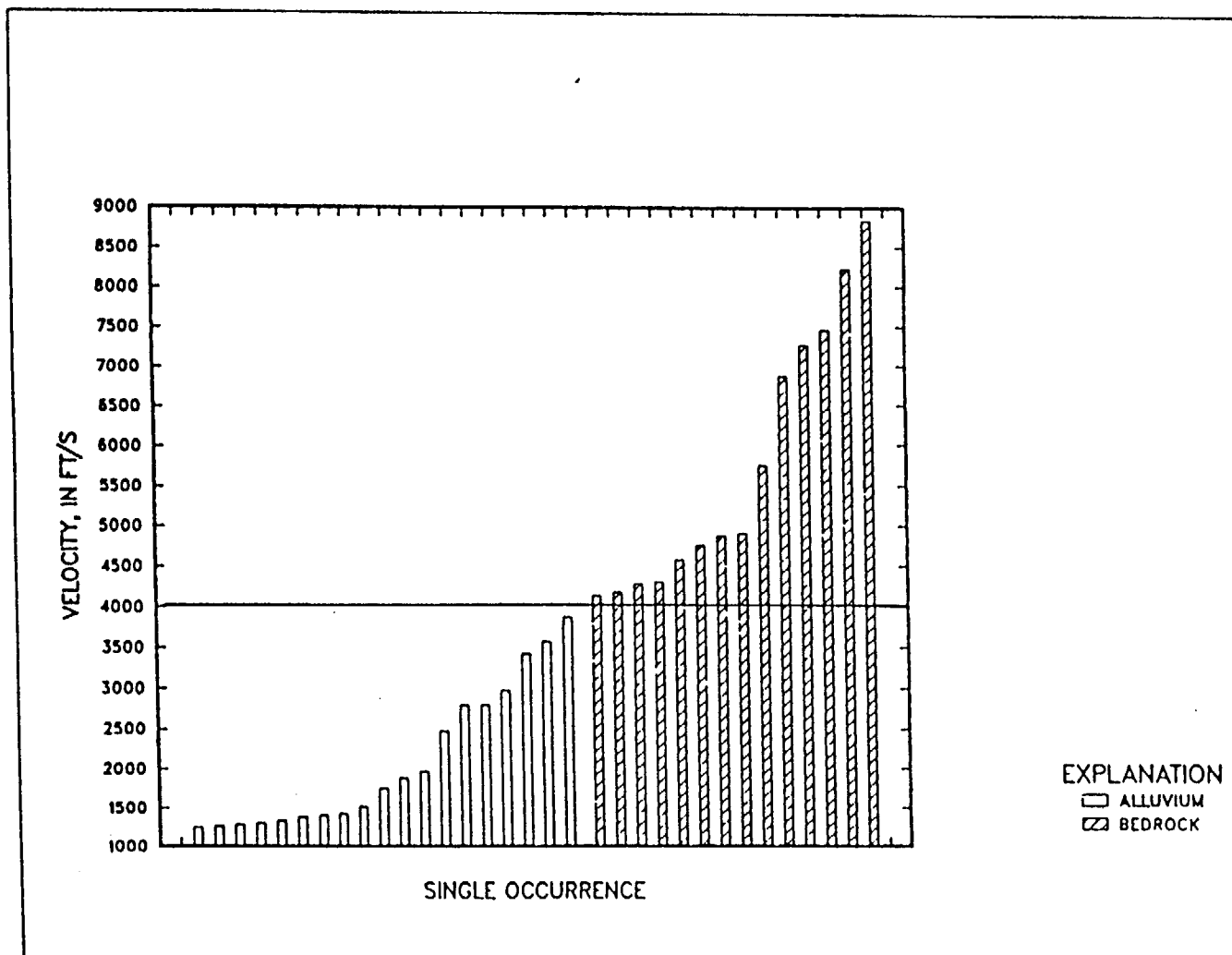


Figure 45.--Histogram of observed compressional wave velocities.

method does have limitations which are controlled by the condition of alluvial overburden. Limits of the depth of investigation could not be defined.

Results cited in this report were generated from data records that had distinct first arrivals. Arrival times could always be picked within a 2-ms range. Each 12-channel seismic line was shot internally and offset from both ends. Geophone spacing was 10-ft. Seven shot-points were used wherever possible. Velocity of alluvium was consistently less than 4000 ft/s; bedrock velocity was greater than 4,000 ft/s. Velocity values obtained for the Tiva Canyon Member agree within the range determined by the previous investigators. The range of bedrock velocities was attributed to changes in degree of weathering degree of welding, and perhaps the low moisture content of the surface bedrock unit.

Seismic lines were surveyed at upper, middle, and lower wash locations. Best data were obtained from mid-wash locations. Data records from upper wash locations (most proximal to Yucca Mountain) contained large amounts of noise that masked the first arrivals of P waves. Seismic data records obtained from lower wash locations (most distal from Yucca Mountain) were generally of poor quality because of noise and distortion of the printed record trace. Seismic noise was attributed to wind and the unconsolidated state of surface sediments.

[Verification of seismic depth models was primarily based on reasonable extrapolation of drill hole data and secondly, on local geology.] Angle and direction of bedrock slope beneath alluvial overburden

was not accurately known, therefore, analytical determination of the change in bedrock elevation along the length of the washes was not possible. When first arrivals have been accurately selected and masked layers accounted for, degree of accuracy of the seismic refraction method has been reported to be between 5 and 20 percent (Domzalski, 1956; Berry, 1971; Wahrhaftig, 1984).

Hidden layers were not considered to be a source of error in this study because of the large quantity of borehole data showing alluvium to be underlain by the Tiva Canyon Member. Velocity inversions could occur because of sand and gravel layers, however, alluvium in the study areas was generally quite thin (less than 40 ft) and often disturbed by flash flooding and runoff. Compaction is gradual or slight.

Drilling associated with the shallow unsaturated zone project is continuing. As of May, 1985, more than 45 neutron access holes have been drilled in several of the washes associated with Yucca Mountain, at upper, middle, and lower wash locations. Bedrock contact is at depths of less than 60 ft at all locations. Sledgehammer seismic refraction methods are well suited to shallow depths of interest. [However, dry, unconsolidated surface materials do not transmit compressional waves well; therefore, use of this method is limited to areas where the surface sediments have not been greatly disturbed.] Data acquisition could be improved by using small explosive charges as the seismic energy source. This may permit the successful seismic surveying of broad washes and bases of washes as well as improve the quality of data obtained from offset shotpoints. / Seismic data interpretations are based

on the first arrival times of compressional waves. Further interpretation of this data, as well as that from surveys that did not produce distinct first arrival times, may be possible using later wave arrival times.

#### REFERENCES

- Ackerman, H.D.; Pankratz, L.W., and Dansereau, D.A., 1982, A comprehensive system for interpreting seismic-refraction arrival-time data using interactive computer methods: U.S. Geological Survey Open-File Report 82-1065, 265 p.
- Berry, M.J., 1971, Depth uncertainties from seismic first-arrival refraction studies: *Journal of Geophysical Research*, v.76, no.26, p. 6464-6468.
- Clark, S.P., Jr., 1966, *Handbook of physical constants*: Geological Society of America, Memoir 97, 587 p.
- Dobrin, M.B., 1976, *Introduction to geophysical prospecting*: New York, McGraw-Hill Book Company, 630 p.
- Domzalski, W., 1956, Some problems of shallow refraction investigations: *Geophysical Prospecting*, v. 4, p. 140-166.
- Duguid, J.O., 1968, Refraction determination of water table depth and alluvium thickness: *Geophysics*, v.33, n. 3, p. 481-488.
- Gardner, L.W., 1939, An areal plan of mapping subsurface structure by refraction shooting: *Geophysics*, v. 4, p. 247-259.
- \_\_\_\_\_ 1967, Refraction seismograph profile interpretation, in Musgrave, A.W., ed., *Seismic refraction prospecting*: Tulsa, Okla., Society of Exploration Geophysicists, p. 338-347.

## REFERENCES--Continued

- Gary, M., McAfee Jr., R., and Wolf, C.L., Eds., 1974, Glossary of geology: Washington D.C., American Geological Institute, 805 p.
- Gough, D.I., 1952, A new instrument for seismic exploration at very short ranges: Geophysics, v.17, nos. 1-4, p.311-333.
- Grant, F.S., and West, G.F., 1965, Interpretation theory in applied geophysics: New York, International Series in Earth Science, McGraw-Hill Book Company, 583 p.
- Green, R., 1962, The hidden layer problem: Geophysical Prospecting, v. 10, p. 166-177.
- Greenhalgh, S.A., 1977, Comments on "The Hidden Layer Problem in Seismic Refraction Work": Geophysical Propecting, v. 25, p.179-181.
- Haeni, F.P., and Melvin, R.L., 1984, High resolution continuous seismic reflection study of a stratified drift deposit in Connecticut: NWWA/EPA Conference on Surface and Borehole Geophysical Methods in Ground Water Investigations, San Antonio, Texas, Feb.7-9, 1984, p. 237-256.
- Halliday, D., and Resnick, R., 1974, Fundamentals of physics: New York, John Wiley & Sons, Inc., 827 p.
- ① Hatherly, P.J., 1982, A computer method for determining seismic first arrival times: Geophysics, v.47, no.10, p.1431-1436.
- ✓ Hobson, G.D., Scott, J.S., and van Everdingen, R.O., 1964, Geotechnical investigations Red River Floodway, Winnipeg, Manitoba: Geological Survey of Canada, paper 65-18, p. 4-15.
- ✓ Hobson, G.D., and Carr, P.A., 1968, Hammer seismic survey, Moncton Map-area, New Brunswick: Geological Survey of Canada, paper 65-43.

## REFERENCES--Continued

- Hoffman, L.R., and Mooney, W.D., 1983, A seismic study of Yucca Mountain and vicinity, Southern Nevada; data report and preliminary results: U.S. Geological Survey Open-File Report 83-588, 25 p.
- Hoover, D.L., Swadley, W C, and Gordon, A.J., 1981, Correlation characteristics of surficial deposits with a description of surficial stratigraphy in the NTS region: U.S. Geological Survey Open-File Report 81-512, 27 p.
- Jakosky, J.J., 1950, Exploration geophysics: Newport Beach, Calif., Trija Publishing Company, 1195 p.
- King, K.W., 1982, A study of surface and subsurface ground motions at Calico Hills, Nevada Test Site: U.S. Geological Survey Open-File Report 82-1044, 19 p.
- Layat, C., 1967, Modified "Gardner" delay time and "Constant Distance Correlation" interpretation, in Musgrave, A.W., ed., Seismic refraction prospecting: Tulsa, Okla., Society of Exploration Geophysicists, p. 171-193.
- Lipman, P.W., and McKay, E.J., 1965, Geologic map of the Topopah Spring SW quadrangle Nye County, Nevada: U.S. Geological Survey Geologic Quadrangle Map GQ-439.
- Mason, B., and Berry, L.G., 1968, Elements of mineralogy: San Francisco, Calif., W.H. Freeman and Company, 550 p.
- Martin, L.C., and Welford, W.T., 1966, Technical optics, v.1: New York, N.Y., Pitman Publishing Corporation.

## REFERENCES--Continued

Merrick, N.P., Odins, J.A., and Greenhalgh, S.A., 1978, A blind zone solution to the problem of hidden layers within a sequence of horizontal or dipping refractors: *Geophysical Prospecting*, v. 26, p. 703-721.

Mooney, H.M., 1977, *Handbook of engineering geophysics*, v. 1: Bison Instruments, Inc., Minneapolis, Minn.

Musgrave, A.W., Ed., 1967, *Seismic refraction prospecting*: Tulsa, Okla., Society of Exploration Geophysicists.

~~\*~~ Pankratz, L.W., 1982, Reconnaissance seismic refraction studies at Calico Hills, Wahmonie, and Yucca Mountain Southwest Nevada Test Site, Nye County, Nevada: U.S. Geological Survey Open-File Report 82-478, 25 p.

Redpath, Bruce, B., 1973, *Seismic refraction exploration for engineering site investigations*: Technical Report E-73-4, National Technical Information Service, Virginia, 51 p.

Schmoller, R., 1982, Some aspects of handling velocity inversion and hidden layer problems in seismic refraction work: *Geophysical Prospecting*, v.30, p. 735-751.

Scott, J.H., 1973, *Seismic refraction modeling by computer*: *Geophysics*, v. 38, no. 2, p.271-284.

       1977, SIPT -- a seismic refraction inverse modeling program for timeshare terminal computer systems: U.S. Geological Survey Open-File Report 77-365, 107 p.

## REFERENCES--Continued

- \_\_\_\_ 1977, SIPB--a seismic refraction inverse modeling program for batch computer systems: U.S. Geological Survey Open-File Rept. 77-366, 108 p.
- Scott, J.H., Tibbets, B.L., and Burdick, R.G., 1972, Computer analysis of seismic refraction data: U.S. Bureau of Mines R.I. 7595, 95 p.
- ∞ Scott, R.B., and Castellanos, M., 1984, Stratigraphic and structural relations of volcanic rocks in drill holes USW GU-3 and USW G-3, Yucca Mountain, Nye County, Nevada: U.S. Geological Survey Open-File Report, 84-491, 121 p.
- Scott, R.B., Spengler, R.W., Diehl, S., Lappin, A.R., and Chornak, M.P., 1983, Geologic character of tuffs in the unsaturated zone at Yucca Mountain, southern Nevada, in Mercer, J. W., and others, eds., Role of the unsaturated zone in radioactive and hazardous waste disposal: Ann Arbor Science, Ann Arbor, Michigan, p.289-335.
- Soske, J.L., 1959, Blind zone problem in engineering geophysics: Geophysics, v.24, p.359-365.
- Spengler, R.W., 1980, Preliminary interpretations of geologic results obtained from boreholes UE25a-4, UE25a-5, UE25a-6, and UE25a-7, Yucca Mountain, Nevada Test Site: U.S. Geological Survey Open-File Report 80-929, 33 p.
- Swadley, W C, 1983, Map showing surficial geology of the Lathrop Wells Quadrangle, Nye County, Nevada: U.S. Geological Survey Miscellaneous Investigations Series Map I-1361, scale 1:48,000.

## REFERENCES--Continued

- Waddell, R.K., Robison, J.H., and Blankennagel, R.K., 1984, Hydrology of Yucca Mountain and vicinity, Nevada-California--investigative results through mid-1983: U.S. Geological Survey Open-File Report 84-4267, 72 p.
- Wahrhaftig, C., Moore, J.G., and Tinsley, J.C., 1984, Geomorphology and glacial geology Wolverton and Crescent Meadow areas and vicinity Sequoia National Park, California: U.S. Geological Survey Open-File Report 84-400.
- Whiteley, R.J., and Greenhalgh, S.A., 1979, Velocity inversion and the shallow seismic refraction method: *Geoexploration* 17, p.125-141.
- Whitfield, M.S., Jr., Thordarson, W., and Eshom, E.P., 1984, Geohydrologic and drill-hole data for test well USW H-4, Yucca Mountain, Nye County, Nevada: U.S. Geological Survey Open-File Report 84-449, 39 p.
- Winograd, I.J., and Thordarson, W., 1975, Hydrogeologic and hydrochemical framework, south-central Great Basin, Nevada-California, with special reference to the Nevada Test Site: U.S. Geological Survey Professional Paper 712-C, 126 p.
- Wyllie, M.R., Gregory, A.R., and Gardner, G.H.F., 1958, An experimental investigation of factors affecting elastic wave velocities in porous media: *Geophysics*, v.23, p.459-493.
- Zohdy, A.A.R., Eaton, G.P., and Mabey, D.R., 1980, Application of surface geophysics to ground-water investigations: *Techniques of Water-Resources Investigations of the U.S. Geological Survey*, Book 2, Chapter D1, 116 p.

MODIFICATION OF THE PRIESTLEY-TAYLOR EVAPORATION  
EQUATION FOR SOIL WATER LIMITED CONDITIONS

Alan L. Flint and Stuart W. Childs

U.S. Geological Survey  
Mercury, Nevada  
and  
Oregon State University  
Corvallis, Oregon

1. INTRODUCTION

A major limitation of many reforestation sites is a lack of water during the growing season. In areas with xeric climates, this is often combined with high temperatures which act to increase plant stress. Any assessment of the harshness of reforestation sites requires information regarding both water supply and environmental demand. The measurement and evaluation of a surface energy budget is a useful analytical approach because components of both the heat and water environments are included. This approach does, however, require detailed, site specific measurements.

A number of simplifications of energy budget techniques have been used to decrease the quantity and intensity of measurements required. The Penman equation (Penman, 1948) is commonly used in situations where detailed data are available. The simplifications used to model the aerodynamic parts of the equation make the equation useful only for calculation of potential evapotranspiration. Furthermore, the equation requires calibration. The Penman-Monteith equation (Monteith, 1966) allows calculation of actual evapotranspiration but requires detailed knowledge about the resistance to heat and water flow at the evaporating surface. Priestley and Taylor (1972) suggested a modification of the Penman equation which requires less extensive measurements:

$$\lambda E_p = \alpha \cdot \frac{s}{s + \gamma} \cdot (Q^* - G) \quad (1)$$

where  $\lambda E_p$  is potential evapotranspiration,  $\alpha$  is a model coefficient,  $s$  is the slope of the saturation vapor density curve,  $\gamma$  is the psychrometric constant,  $Q^*$  is net radiation and  $G$  is soil heat flux. In this formulation the aerodynamic term is modeled as  $(\alpha-1) \cdot [s/(s+\gamma)] \cdot (Q^*-G)$ . This simplification is successful because the radiation term generally dominates the aerodynamic term (Stewart, 1983).

The coefficient  $\alpha$  for daily calculations is 1.26 for freely evaporating surfaces (Priestley and Taylor, 1972; Stewart and Rouse, 1977).  $\alpha$  depends on surface vegetation and microclimatic conditions and ranges from 1.57 for conditions of strong advection to 0.72 for forest conditions (Table 1).

Table 1. Measured values of the Priestley-Taylor coefficient,  $\alpha$ .

$\alpha$	Surface conditions	Reference
1.57	Strongly advective conditions	Jury & Tanner, 1975
1.29	Grass (soil at field capacity)	Mukammal & Neumann, 1977
1.27	Irrigated ryegrass	Davies & Allen, 1972
1.26	Saturated surface	Priestley & Taylor, 1972
1.26	Open water surface	Priestley & Taylor, 1972
1.26	Wet meadow	Stewart & Rouse, 1977
1.18	Wet Douglas-fir forest	McNaughton & Black, 1973
1.12	Short grass	DeBruin & Holtslag, 1982
1.05	Douglas-fir forest	McNaughton & Black, 1973
1.04	Bare soil surface	Barton, 1979
0.84	Douglas-fir forest Unthinned	Black, 1979
0.80	Douglas-fir forest Thinned	Black, 1979
0.73	Douglas-fir forest (Daytime)	Giles et al., 1984
0.72	Spruce forest (Daytime)	Shuttleworth & Calder, 1979

Although the value of  $\alpha$  for moist surface conditions ( $\alpha > 1$ ) may be a function of wind speed and aerodynamic resistance, under drier conditions ( $\alpha < 1$ ) it is related to surface resistance (De Bruin, 1983). Actual evapotranspiration under dry conditions is lower than potential and depends on soil water status, exchange surface properties and environmental demand (Black, 1979; De Bruin, 1983; Priestley and Taylor, 1972; Tanner and Jury, 1975).

Methods involving calculation of surface resistance have generally been based on the Penman-Monteith equation. Use of the Priestley-Taylor equation for calculation of actual evapotranspiration has involved empirical relationships to soil water content. Often,  $\alpha$  is redefined to be a function of soil water content (Mukammal and Neumann, 1977, Davies and Allen, 1972, Barton, 1979). Another approach is to define a soil water content below which evapotranspiration is limited and the Priestley-Taylor equation is in error. This value would vary

greatly with soil type, vegetation and environmental demand but covers a much smaller range when expressed as a percentage of total "available" soil water (Table 2). For vegetated surfaces, 50 to 80 percent of the "available" soil water can be extracted at the potential rate. Bare soil evaporation was limited when 40 percent of the available water was removed. This result is not unexpected (Tanner and Jury, 1976).

## 2. OBJECTIVE AND APPROACH

The objective of this research was to calibrate the modified Priestley-Taylor equation for soil water limited conditions. This was done by redefining the coefficient,  $\alpha$ , to be a function of soil water content ( $\alpha'$ ). Since soil water status changes with depth, we also examined the relationship between  $\alpha'$  and soil water content at different depths. Although the original approach of Priestley and Taylor was to apply their formulation to large scale environments, we apply the modified version to a small forest clearcut.

Table 2. Percentage reduction in "available" water ( $R_c$ ) before evapotranspiration is limited.

$R_c$	Surface conditions	Reference
82	Douglas-fir forest (Low Demand)	Black & Spittlehouse, 1980
81	Lysimeter and bean crop	Priestley & Taylor, 1972
77	Lysimeter and field crop	Priestley & Taylor, 1972
75	Lysimeter and grass cover	Mukammal & Neumann, 1977
66	Douglas-fir forest (High Demand)	Black & Spittlehouse, 1980
60	Douglas-fir forest	Black, 1979
60	Forest clearcut	Figure 3, this paper
55	Cropped surface	Davies & Allen, 1972
50	Lysimeter and pasture crop	Priestley & Taylor, 1972
40	Bare soil surface	Estimate from Barton, 1979

## 3. METHODS

### 3.1 Field Methods

Data for this study were obtained during a reforestation field experiment in southwest Oregon [see Flint and Childs (1987) for complete details]. The site had a southerly exposure, a shallow, rocky soil and 81 percent vegetation cover. Measurements of soil water content and temperature were made at ten locations and averaged for the site. Data were collected on ten dates between April and September, 1983. Soil water content was measured using a two probe gamma attenuation device (Model 2376, Troxler Labs, Research Triangle Park, NC) in 0.025 m depth intervals.

Soil temperatures were measured at five depths (0.02, 0.04, 0.08, 0.16, 0.32 m) using five thermistors (YSI #44202, Yellow Springs Instruments, Yellow Springs, OH) in a plastic probe. Data were integrated for 15 minutes and stored in a data logger (Model CR-5, Campbell Scientific Inc., Logan, UT). Temperature data and soil heat capacities calculated from soil density and water content were used to calculate soil heat flux using a calorimetric technique (Fuchs, 1986).

Air temperatures were measured at 0.2 m and 2.0 m using thermistors (YSI #44202) mounted in radiation shields. Dew point temperatures were measured at 0.2 and 2.0 m using LiCl dew-cells (Holbo, 1981). Net radiation was measured using a miniature all-wave net radiometer (C. W. Thornthwaite Assoc., Camden, NJ). Sensor output was read every 10 seconds, integrated for 30 minutes and stored [using a Model CR-21 data-logger (Campbell Scientific Inc., Logan, UT)].

### 3.2 Modeling Procedure

Actual evaporation was calculated hourly using the Bowen ratio method:

$$\lambda E_a = \frac{(Q^* - G)}{1 + \beta} \quad (2)$$

where  $\beta$ , the Bowen ratio, is the ratio of sensible to latent heat flux.  $\beta$  is calculated as:

$$\beta = \frac{\rho C_p (T_1 - T_2)}{\lambda (\rho_1 - \rho_2)} \quad (3)$$

where  $\rho C_p$  is the volumetric heat capacity of air,  $\lambda$  is the latent heat of vaporization,  $T_1$  and  $T_2$  are air temperatures at two heights,  $\rho_1$  and  $\rho_2$  are water vapor density at the same heights.

The Priestley-Taylor equation (Eq. 1) was modified by replacing  $\lambda E_p$  and  $\alpha$  with  $\lambda E_a$  and  $\alpha'$  and solving for  $\alpha'$ :

$$\alpha' = \frac{\lambda E_a}{\frac{s}{s+\gamma} \cdot (Q^* - G)} \quad (4)$$

Although the coefficient  $\alpha'$  could be related to any process that limits evapotranspiration (e.g. soil hydraulic resistance, aerodynamic resistance, stomatal resistance), we chose to relate  $\alpha'$  to soil water status in a manner similar to Davies and Allen (1973) and Barton (1979):

$$\alpha' = A [1 - \exp(-B \frac{\theta}{\theta_s})] \quad (5)$$

where A and B are regression coefficients and  $\theta/\theta_s$  is the current volumetric soil water content divided by the value at saturation. Davies and Allen (1972) used soil water content divided by soil water content at field capacity ( $\theta/\theta_{fc}$ ) while Barton (1979) simply used gravimetric water content without any scaling. In Eq. 5 the coefficient A approaches the Priestley-Taylor coefficient ( $\alpha$ ) as the soil moisture content approaches saturation.

#### 4. RESULTS AND DISCUSSION

One of the ten diurnal data sets analyzed is shown in Figure 1. The measured values (Bowen ratio) and the modeled data (modified Priestley-Taylor equation with daily average  $\alpha'$ ) are in close agreement at midday. The apparent error in measured values of  $\lambda E_a$  occurs when the Bowen ratio ( $\beta$ ) is near -1 (0700, 1800 and 1900 hours, Figure 2). In order to avoid the large variation in  $\alpha'$  calculated when the Bowen ratio method is unstable (Jury and Tanner, 1975), daily average values of  $\alpha'$  were calculated using midday values of  $\alpha'$  when  $\beta > 0$ . The magnitude of error associated with applying the midday average of  $\alpha'$  to early and late periods of the day is small because the value of  $(Q^* - G)$  is small. The Bowen ratio technique could also be improved by smoothing or averaging  $\beta$ . We preferred, however, to use the Priestley-Taylor equation because of the smaller data requirements.

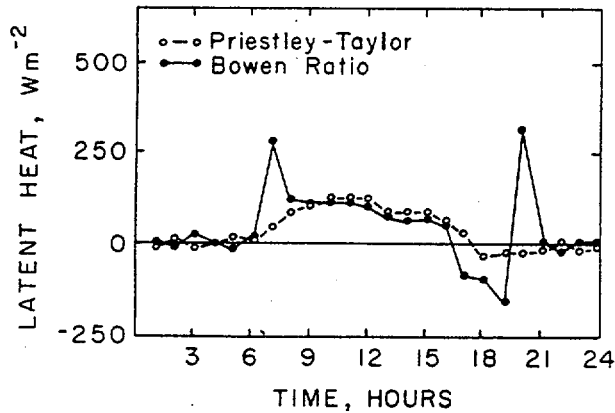


Figure 1. Results of latent heat flux using the Bowen ratio technique and the Priestley-Taylor technique with the daytime average value of the modified Priestley-Taylor coefficient  $\alpha'$  for August 12, 1983. ( $\alpha' = 0.55$ ).

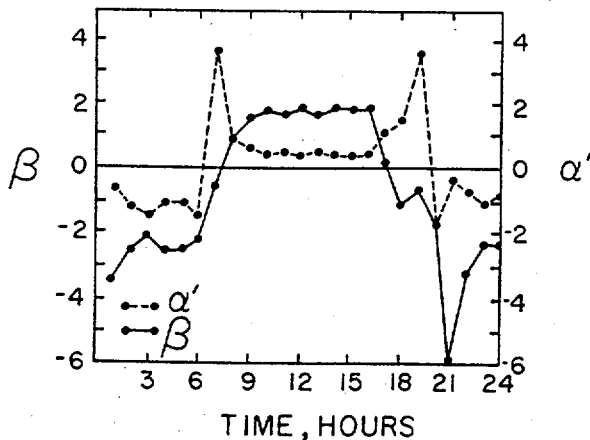


Figure 2. Values for the Bowen ratio ( $\beta$ ) and for the ratio of latent heat ( $\lambda E$ ) to  $(s/s+\gamma) \cdot (Q^* - G)$  which is equated to the Priestley-Taylor coefficient  $\alpha'$  for nonsaturated conditions.

The regression coefficients A and B in Eq. 5 were estimated using nonlinear regression of  $\alpha'$  against  $\theta/\theta_s$ . The values for  $\theta$  and  $\theta_s$  were determined for five different total soil profile depth increments (Table 3).

Table 3. Results of a series of regressions between  $\alpha'$  and  $\theta/\theta_s$  (Eq. 5). SSQ is the error sum of squares.

Depth (m)	----- $\theta/\theta_s$ -----		
	A	B	SSQ
All data points			
0-0.1	1.08	-4.06	0.1178
0-0.2	1.09	-4.20	0.1243
0-0.3	1.18	-3.41	0.1017
0-0.4	1.17	-3.38	0.0922
0-0.5	1.27	-2.83	0.0831
----- $\theta/\theta_s$ -----			
Depth (m)	----- $\theta/\theta_s$ -----		
	A	B	SSQ
All data points where $Q^* > 12 \text{ MJ m}^{-2}$			
0-0.1	0.89	-6.30	0.0559
0-0.2	0.88	-6.63	0.0642
0-0.3	0.93	-5.42	0.0490
0-0.4	0.96	-4.82	0.0378
0-0.5	1.00	-4.18	0.0371

The effect of depth of water content measurement on regression results showed distinct trends. Increased profile depth reduced the error sum of squares (SSQ) in the regressions. The coefficient A, which should approximate the Priestley-Taylor coefficient ( $\alpha$ ) ranges from 1.08 to 1.27 as the soil thickness goes from 0.1 to 0.5 m. This large variation is within the range commonly measured (Table 1) but the sensitivity of this value to depth of measurement of soil water content discourages attaching any significance to the value of A.

The relationship of  $\alpha'$  to soil water content is given in Figure 3 for a profile depth of 0.50 m. The regression fits the data well except at higher soil water contents. One of these outlier points represents a day with low environmental demand. Black (1979) suggested that it may be inappropriate to use the modified Priestley-Taylor approach on such days because even soils with low water content can supply enough water for potential evapotranspiration. We reanalyzed our data excluding values with a total radiation load of  $< 12 \text{ MJ m}^{-2} \text{ day}^{-1}$  (one data point is noted in Figure 3). The resulting values of A (0.89 to 1.00 over the depth range, Table 4) were similar to the values of  $\alpha$  found by Black (1979, Table 1). Excluding the one data point  $< 12 \text{ MJ m}^{-2} \text{ day}^{-1}$ , would yield an estimate of  $A \approx 0.85$  when the soil is near field capacity ( $\theta/\theta_s \approx 0.6$ ).

A simplified formulation of  $\alpha'$  would be to set an upper limit of  $\alpha' = 0.85$  where  $\lambda E_p =$

$\alpha E_a$ .  $\alpha'$  could be reduced when soil water content falls below some critical value of  $\theta/\theta_s$  where soil water supply limits evapotranspiration. By estimating total available water content as the difference between field capacity ( $\theta/\theta_s \approx 0.60$ ) and driest seasonal water content ( $\theta/\theta_s \approx 0.18$ ) it can be seen that when more than 60 percent of this total available water is used, ( $\theta/\theta_s \approx 0.35$ , Figure 3), soil water becomes limiting. This value is in general agreement with the data in Table 2. Although further analysis is needed to properly evaluate  $\alpha'$  when the soil is at field capacity for our soil, the relationship between  $\alpha'$  and  $\theta/\theta_s$  below field capacity would remain the same.

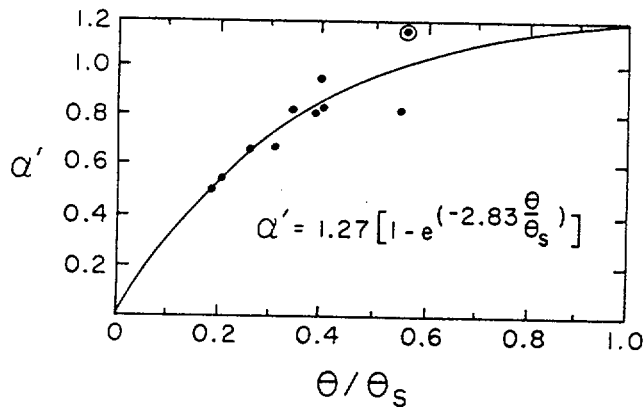


Figure 3. Modified Priestley-Taylor coefficient  $\alpha'$  versus percentage of saturation ( $\theta/\theta_s$ , 0-0.5 m). The circled point indicates data for a day with  $Q^* < 12 \text{ MJ m}^{-2} \text{ day}^{-1}$ .

## 5. CONCLUSIONS

The Priestley-Taylor equation can be used to calculate actual evaporation by incorporating  $\alpha'$ , a variable dependent on soil water content. The relationship to soil water content is exponential. The coefficients A and B depend on the depth of measurement for soil water content and the environmental demand. The best results for our data were achieved when soil water content was averaged from the surface to 0.50 m and any data point with total radiation less than  $12 \text{ MJ m}^{-2} \text{ day}^{-1}$  was excluded.

## 6. REFERENCES

- Barton, I. J., 1979. A parameterization of the evaporation from nonsaturated surfaces. *J. Appl. Meteorol.* 18:43-47.
- Black, T. A., 1979. Evapotranspiration from Douglas-fir stands exposed to soil water deficits. *Water Resour. Res.* 15(1):164-170.
- Black, T. A. and D. L. Spittlehouse, 1980. Modeling the water balance for watershed management. p. 117-129. In: D. M. Baumgartner (ed.), *Interior West Watershed Management*. Washington State University. Pullman, WA.
- Davies, J. A. and C. D. Allen, 1973. Equilibrium, potential and actual evaporation from cropped surfaces in southern Ontario. *J. Appl. Meteorol.* 12:649-657.
- De Bruin, H. A. R., 1983. A model for the Priestley-Taylor parameter  $\alpha$ . *J. Climate and Appl. Meteorol.* 22:572-578.
- De Bruin, H. A. R. and A. A. M. Holtslag, 1982. A simple parameterization of the surface fluxes of sensible and latent heat during daytime compared with the Penman-Monteith concept. *J. Appl. Meteorol.* 21:1610-1621.
- Flint, L. E. and S. W. Childs, 1987. Competing vegetation and soil surface effects on seedling water use. *Forest Ecol. Manage.* 18: .
- Fuchs, M., 1986. Heat flux. p. 957-968. In: A Klute (ed.) *Methods of soil analysis, Part 1. Physical and mineralogical methods*. Agron. Monograph 9, 2nd Ed. Amer. Soc. Agron., Madison, WI.
- Giles, D. G., T. A. Black and D. L. Spittlehouse, 1985. Determination of growing season soil water deficits on a forested slope using water balance analysis. *Can. J. For. Res.* 15:107-114.
- Holbo, H. R., 1981. A dew-point hygrometer for field use. *Agric. Meteorol.* 24:117-130.
- Jury, W. A. and C. B. Tanner, 1975. Advection modification of the Priestley and Taylor evapotranspiration formula. *Agron. J.* 67:840-842.
- McNaughton, K. G. and T. A. Black, 1973. A study of evapotranspiration from a Douglas-fir forest using the energy balance approach. *Water Resour. Res.* 9:1579-1590.
- Monteith, J. L., 1964. Evaporation and environment. In *The State and Movement of Water in Living Organisms*. 19th Symp. Soc. exp. Biol., 205.
- Mukammal, E. I. and H. H. Neumann, 1977. Application of the Priestley-Taylor evaporation model to assess the influence of soil moisture on the evaporation from a large weighing lysimeter and class A pan. *Boundary Layer Meteorol.* 12:243-256.
- Penman, H. L., 1948. Natural evaporation from open water, bare soil and grass. *Proc. Roy. Soc. London.* A193:120-145.
- Priestley, C. H. B. and R. J. Taylor, 1972. On the assessment of surface heat flux and evaporation using large-scale parameters. *Monthly Weather Rev.* 100(2):81-92.
- Shuttleworth, W. J. and I. R. Calder, 1979. Has the Priestley-Taylor equation any relevance to forest evaporation? *J. Appl. Meteorol.* 18:639-646.
- Stewart, R. B., 1983. A discussion of the relationships between the principal forms of the combination equation for estimating crop evaporation. *Agric. Meteorol.* 30:111-127.
- Stewart, R. B. and W. R. Rouse, 1977. Substantiation of the Priestley and Taylor parameter  $\alpha=1.26$  for potential evaporation in high latitudes. *J. Appl. Meteorol.* 16:649-650.
- Tanner, C. B. and W. A. Jury, 1976. Estimating evaporation and transpiration from a row crop during incomplete cover. *Agron. J.* 68:239-243.

MODIFICATION OF THE PRIESTLEY-TAYLOR EVAPORATION  
EQUATION FOR SOIL WATER LIMITED CONDITIONS

Alan L. Flint and Stuart W. Childs

U.S. Geological Survey  
Mercury, Nevada  
and

Oregon State University  
Corvallis, Oregon

### 1. INTRODUCTION

A major limitation of many reforestation sites is a lack of water during the growing season. In areas with xeric climates, this is often combined with high temperatures which act to increase plant stress. Any assessment of the harshness of reforestation sites requires information regarding both water supply and environmental demand. The measurement and evaluation of a surface energy budget is a useful analytical approach because components of both the heat and water environments are included. This approach does, however, require detailed, site specific measurements.

A number of simplifications of energy budget techniques have been used to decrease the quantity and intensity of measurements required. The Penman equation (Penman, 1948) is commonly used in situations where detailed data are available. The simplifications used to model the aerodynamic parts of the equation make the equation useful only for calculation of potential evapotranspiration. Furthermore, the equation requires calibration. The Penman-Monteith equation (Monteith, 1966) allows calculation of actual evapotranspiration but requires detailed knowledge about the resistance to heat and water flow at the evaporating surface. Priestley and Taylor (1972) suggested a modification of the Penman equation which requires less extensive measurements:

$$\lambda E_p = \alpha \cdot \frac{s}{s + \gamma} \cdot (Q^* - G) \quad (1)$$

where  $\lambda E_p$  is potential evapotranspiration,  $\alpha$  is a model coefficient,  $s$  is the slope of the saturation vapor density curve,  $\gamma$  is the psychrometric constant,  $Q^*$  is net radiation and  $G$  is soil heat flux. In this formulation the aerodynamic term is modeled as  $(\alpha-1) \cdot [s/(s+\gamma)] \cdot (Q^*-G)$ . This simplification is successful because the radiation term generally dominates the aerodynamic term (Stewart, 1983).

The coefficient  $\alpha$  for daily calculations is 1.26 for freely evaporating surfaces (Priestley and Taylor, 1972; Stewart and Rouse, 1977).  $\alpha$  depends on surface vegetation and microclimatic conditions and ranges from 1.57 for conditions of strong advection to 0.72 for forest conditions (Table 1).

Table 1. Measured values of the Priestley-Taylor coefficient,  $\alpha$ .

$\alpha$	Surface conditions	Reference
1.57	Strongly advective conditions	Jury & Tanner, 1975
1.29	Grass (soil at field capacity)	Mukammal & Neumann, 1977
1.27	Irrigated ryegrass	Davies & Allen, 1972
1.26	Saturated surface	Priestley & Taylor, 1972
1.26	Open water surface	Priestley & Taylor, 1972
1.26	Wet meadow	Stewart & Rouse, 1977
1.18	Wet Douglas-fir forest	McNaughton & Black, 1973
1.12	Short grass	DeBruin & Holtslag, 1982
1.05	Douglas-fir forest	McNaughton & Black, 1973
1.04	Bare soil surface	Barton, 1979
0.84	Douglas-fir forest Unthinned	Black, 1979
0.80	Douglas-fir forest Thinned	Black, 1979
0.73	Douglas-fir forest (Daytime)	Giles et al., 1984
0.72	Spruce forest (Daytime)	Shuttleworth & Calder, 1979

Although the value of  $\alpha$  for moist surface conditions ( $\alpha > 1$ ) may be a function of wind speed and aerodynamic resistance, under drier conditions ( $\alpha < 1$ ) it is related to surface resistance (De Bruin, 1983). Actual evapotranspiration under dry conditions is lower than potential and depends on soil water status, exchange surface properties and environmental demand (Black, 1979; De Bruin, 1983; Priestley and Taylor, 1972; Tanner and Jury, 1975).

Methods involving calculation of surface resistance have generally been based on the Penman-Monteith equation. Use of the Priestley-Taylor equation for calculation of actual evapotranspiration has involved empirical relationships to soil water content. Often,  $\alpha$  is redefined to be a function of soil water content (Mukammal and Neumann, 1977, Davies and Allen, 1972, Barton, 1979). Another approach is to define a soil water content below which evapotranspiration is limited and the Priestley-Taylor equation is in error. This value would vary

greatly with soil type, vegetation and environmental demand but covers a much smaller range when expressed as a percentage of total "available" soil water (Table 2). For vegetated surfaces, 50 to 80 percent of the "available" soil water can be extracted at the potential rate. Bare soil evaporation was limited when 40 percent of the available water was removed. This result is not unexpected (Tanner and Jury, 1976).

## 2. OBJECTIVE AND APPROACH

The objective of this research was to calibrate the modified Priestley-Taylor equation for soil water limited conditions. This was done by redefining the coefficient,  $\alpha$ , to be a function of soil water content ( $\alpha'$ ). Since soil water status changes with depth, we also examined the relationship between  $\alpha'$  and soil water content at different depths. Although the original approach of Priestley and Taylor was to apply their formulation to large scale environments, we apply the modified version to a small forest clearcut.

Table 2. Percentage reduction in "available" water ( $R_c$ ) before evapotranspiration is limited.

$R_c$	Surface conditions	Reference
82	Douglas-fir forest (Low Demand)	Black & Spittlehouse, 1980
81	Lysimeter and bean crop	Priestley & Taylor, 1972
77	Lysimeter and field crop	Priestley & Taylor, 1972
75	Lysimeter and grass cover	Mukammal & Neumann, 1977
66	Douglas-fir forest (High Demand)	Black & Spittlehouse, 1980
60	Douglas-fir forest	Black, 1979
60	Forest clearcut	Figure 3, this paper
55	Cropped surface	Davies & Allen, 1972
50	Lysimeter and pasture crop	Priestley & Taylor, 1972
40	Bare soil surface	Estimate from Barton, 1979

## 3. METHODS

### 3.1 Field Methods

Data for this study were obtained during a reforestation field experiment in southwest Oregon [see Flint and Childs (1987) for complete details]. The site had a southerly exposure, a shallow, rocky soil and 81 percent vegetation cover. Measurements of soil water content and temperature were made at ten locations and averaged for the site. Data were collected on ten dates between April and September, 1983. Soil water content was measured using a two probe gamma attenuation device (Model 2376, Troxler Labs, Research Triangle Park, NC) in 0.025 m depth intervals.

Soil temperatures were measured at five depths (0.02, 0.04, 0.08, 0.16, 0.32 m) using five thermistors (YSI #44202, Yellow Springs Instruments, Yellow Springs, OH) in a plastic probe. Data were integrated for 15 minutes and stored in a data logger (Model CR-5, Campbell Scientific Inc., Logan, UT). Temperature data and soil heat capacities calculated from soil density and water content were used to calculate soil heat flux using a calorimetric technique (Fuchs, 1986).

Air temperatures were measured at 0.2 m and 2.0 m using thermistors (YSI #44202) mounted in radiation shields. Dew point temperatures were measured at 0.2 and 2.0 m using LiCl dew-cells (Holbo, 1981). Net radiation was measured using a miniature all-wave net radiometer (C. W. Thornthwaite Assoc., Camden, NJ). Sensor output was read every 10 seconds, integrated for 30 minutes and stored [using a Model CR-21 data-logger (Campbell Scientific Inc., Logan, UT)].

### 3.2 Modeling Procedure

Actual evaporation was calculated hourly using the Bowen ratio method:

$$\lambda E_a = \frac{(Q^* - G)}{1 + \beta} \quad (2)$$

where  $\beta$ , the Bowen ratio, is the ratio of sensible to latent heat flux.  $\beta$  is calculated as:

$$\beta = \frac{\rho C_p (T_1 - T_2)}{\lambda (\rho_1 - \rho_2)} \quad (3)$$

where  $\rho C_p$  is the volumetric heat capacity of air,  $\lambda$  is the latent heat of vaporization,  $T_1$  and  $T_2$  are air temperatures at two heights,  $\rho_1$  and  $\rho_2$  are water vapor density at the same heights.

The Priestley-Taylor equation (Eq. 1) was modified by replacing  $\lambda E_p$  and  $\alpha$  with  $\lambda E_a$  and  $\alpha'$  and solving for  $\alpha'$ :

$$\alpha' = \frac{\lambda E_a}{\frac{s}{s+\gamma} \cdot (Q^* - G)} \quad (4)$$

Although the coefficient  $\alpha'$  could be related to any process that limits evapotranspiration (e.g. soil hydraulic resistance, aerodynamic resistance, stomatal resistance), we chose to relate  $\alpha'$  to soil water status in a manner similar to Davies and Allen (1973) and Barton (1979):

$$\alpha' = A[1 - \exp(-B \frac{\theta}{\theta_s})] \quad (5)$$

where  $A$  and  $B$  are regression coefficients and  $\theta/\theta_s$  is the current volumetric soil water content divided by the value at saturation. Davies and Allen (1972) used soil water content divided by soil water content at field capacity ( $\theta/\theta_{fc}$ ) while Barton (1979) simply used gravimetric water content without any scaling. In Eq. 5 the coefficient  $A$  approaches the Priestley-Taylor coefficient ( $\alpha$ ) as the soil moisture content approaches saturation.

#### 4. RESULTS AND DISCUSSION

One of the ten diurnal data sets analyzed is shown in Figure 1. The measured values (Bowen ratio) and the modeled data (modified Priestley-Taylor equation with daily average  $\alpha'$ ) are in close agreement at midday. The apparent error in measured values of  $\lambda E_a$  occurs when the Bowen ratio ( $\beta$ ) is near -1 (0700, 1800 and 1900 hours, Figure 2). In order to avoid the large variation in  $\alpha'$  calculated when the Bowen ratio method is unstable (Jury and Tanner, 1975), daily average values of  $\alpha'$  were calculated using midday values of  $\alpha'$  when  $\beta > 0$ . The magnitude of error associated with applying the midday average of  $\alpha'$  to early and late periods of the day is small because the value of  $(Q^*-G)$  is small. The Bowen ratio technique could also be improved by smoothing or averaging  $\beta$ . We preferred, however, to use the Priestley-Taylor equation because of the smaller data requirements.

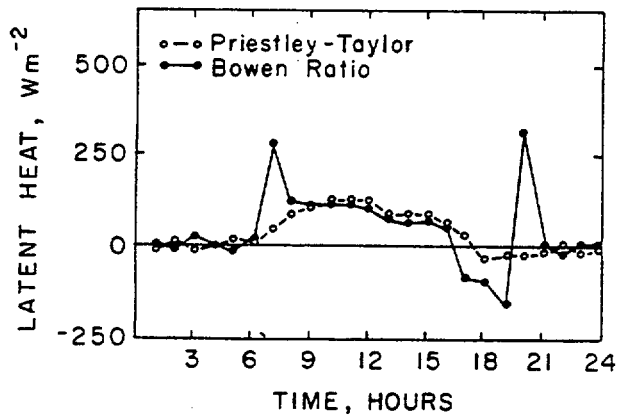


Figure 1. Results of latent heat flux using the Bowen ratio technique and the Priestley-Taylor technique with the daytime average value of the modified Priestley-Taylor coefficient  $\alpha'$  for August 12, 1983. ( $\alpha' = 0.55$ ).

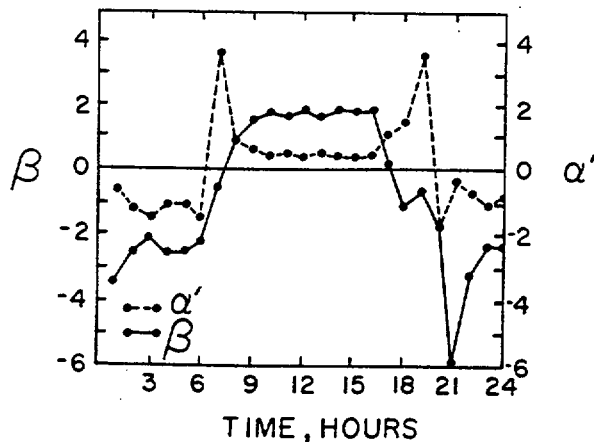


Figure 2. Values for the Bowen ratio ( $\beta$ ) and for the ratio of latent heat ( $\lambda E$ ) to  $(s/s+\gamma) \cdot (Q^*-G)$  which is equated to the Priestley-Taylor coefficient  $\alpha'$  for nonsaturated conditions.

The regression coefficients A and B in Eq. 5 were estimated using nonlinear regression of  $\alpha'$  against  $\theta/\theta_s$ . The values for  $\theta$  and  $\theta_s$  were determined for five different total soil profile depth increments (Table 3).

Table 3. Results of a series of regressions between  $\alpha'$  and  $\theta/\theta_s$  (Eq. 5). SSQ is the error sum of squares.

Depth (m)	----- $\theta/\theta_s$ -----		SSQ
	A	B	
All data points			
0-0.1	1.08	-4.06	0.1178
0-0.2	1.09	-4.20	0.1243
0-0.3	1.18	-3.41	0.1017
0-0.4	1.17	-3.38	0.0922
0-0.5	1.27	-2.83	0.0831
----- $\theta/\theta_s$ -----			
Depth (m)	----- $\theta/\theta_s$ -----		SSQ
	A	B	
All data points where $Q^* > 12 \text{ MJ m}^{-2}$			
0-0.1	0.89	-6.30	0.0559
0-0.2	0.88	-6.63	0.0642
0-0.3	0.93	-5.42	0.0490
0-0.4	0.96	-4.82	0.0378
0-0.5	1.00	-4.18	0.0371

The effect of depth of water content measurement on regression results showed distinct trends. Increased profile depth reduced the error sum of squares (SSQ) in the regressions. The coefficient A, which should approximate the Priestley-Taylor coefficient ( $\alpha$ ) ranges from 1.08 to 1.27 as the soil thickness goes from 0.1 to 0.5 m. This large variation is within the range commonly measured (Table 1) but the sensitivity of this value to depth of measurement of soil water content discourages attaching any significance to the value of A.

The relationship of  $\alpha'$  to soil water content is given in Figure 3 for a profile depth of 0.50 m. The regression fits the data well except at higher soil water contents. One of these outlier points represents a day with low environmental demand. Black (1979) suggested that it may be inappropriate to use the modified Priestley-Taylor approach on such days because even soils with low water content can supply enough water for potential evapotranspiration. We reanalyzed our data excluding values with a total radiation load of  $<12 \text{ MJ m}^{-2} \text{ day}^{-1}$  (one data point is noted in Figure 3). The resulting values of A (0.89 to 1.00 over the depth range, Table 4) were similar to the values of  $\alpha$  found by Black (1979, Table 1). Excluding the one data point  $<12 \text{ MJ m}^{-2} \text{ day}^{-1}$ , would yield an estimate of A  $\approx 0.85$  when the soil is near field capacity ( $\theta/\theta_s \approx 0.6$ ).

A simplified formulation of  $\alpha'$  would be to set an upper limit of  $\alpha' = 0.85$  where  $\lambda E_p =$

$\lambda E_a$ .  $\alpha'$  could be reduced when soil water content falls below some critical value of  $\theta/\theta_s$  where soil water supply limits evapotranspiration. By estimating total available water content as the difference between field capacity ( $\theta/\theta_s \approx 0.60$ ) and driest seasonal water content ( $\theta/\theta_s \approx 0.18$ ) it can be seen that when more than 60 percent of this total available water is used, ( $\theta/\theta_s \approx 0.35$ , Figure 3), soil water becomes limiting. This value is in general agreement with the data in Table 2. Although further analysis is needed to properly evaluate  $\alpha'$  when the soil is at field capacity for our soil, the relationship between  $\alpha'$  and  $\theta/\theta_s$  below field capacity would remain the same.

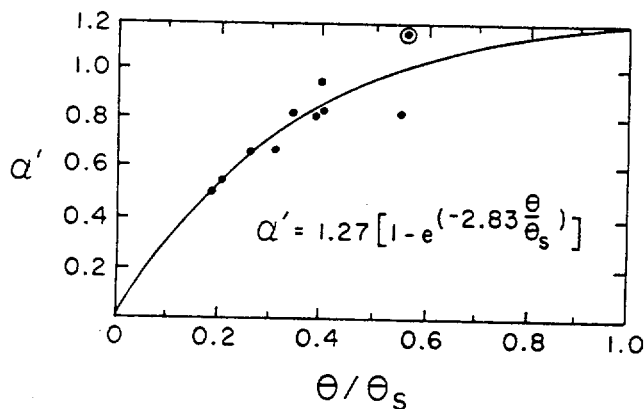


Figure 3. Modified Priestley-Taylor coefficient  $\alpha'$  versus percentage of saturation ( $\theta/\theta_s$ , 0-0.5 m). The circled point indicates data for a day with  $Q^* < 12 \text{ MJ m}^{-2} \text{ day}^{-1}$ .

## 5. CONCLUSIONS

The Priestley-Taylor equation can be used to calculate actual evaporation by incorporating  $\alpha'$ , a variable dependent on soil water content. The relationship to soil water content is exponential. The coefficients A and B depend on the depth of measurement for soil water content and the environmental demand. The best results for our data were achieved when soil water content was averaged from the surface to 0.50 m and any data point with total radiation less than  $12 \text{ MJ m}^{-2} \text{ day}^{-1}$  was excluded.

## 6. REFERENCES

- Barton, I. J., 1979. A parameterization of the evaporation from nonsaturated surfaces. *J. Appl. Meteorol.* 18:43-47.
- Black, T. A., 1979. Evapotranspiration from Douglas-fir stands exposed to soil water deficits. *Water Resour. Res.* 15(1):164-170.
- Black, T. A. and D. L. Spittlehouse, 1980. Modeling the water balance for watershed management. p. 117-129. In: D. M. Baumgartner (ed.), *Interior West Watershed Management*. Washington State University, Pullman, WA.
- Davies, J. A. and C. D. Allen, 1973. Equilibrium, potential and actual evaporation from cropped surfaces in southern Ontario. *J. Appl. Meteorol.* 12:649-657.
- De Bruin, H. A. R., 1983. A model for the Priestley-Taylor parameter  $\alpha$ . *J. Climate and Appl. Meteorol.* 22:572-578.
- De Bruin, H. A. R. and A. A. M. Holtslag, 1982. A simple parameterization of the surface fluxes of sensible and latent heat during daytime compared with the Penman-Monteith concept. *J. Appl. Meteorol.* 21:1610-1621.
- Flint, L. E. and S. W. Childs, 1987. Competing vegetation and soil surface effects on seedling water use. *Forest Ecol. Manage.* 18: .
- Fuchs, M., 1986. Heat flux. p. 957-968. In: A Klute (ed.) *Methods of soil analysis, Part 1. Physical and mineralogical methods*. Agron. Monograph 9, 2nd Ed. Amer. Soc. Agron., Madison, WI.
- Giles, D. G., T. A. Black and D. L. Spittlehouse, 1985. Determination of growing season soil water deficits on a forested slope using water balance analysis. *Can. J. For. Res.* 15:107-114.
- Holbo, H. R., 1981. A dew-point hygrometer for field use. *Agric. Meteorol.* 24:117-130.
- Jury, W. A. and C. B. Tanner, 1975. Advection modification of the Priestley and Taylor evapotranspiration formula. *Agron. J.* 67:840-842.
- McNaughton, K. G. and T. A. Black, 1973. A study of evapotranspiration from a Douglas-fir forest using the energy balance approach. *Water Resour. Res.* 9:1579-1590.
- Monteith, J. L., 1964. Evaporation and environment. In *The State and Movement of Water in Living Organisms*. 19th Symp. Soc. exp. Biol., 205.
- Mukammal, E. I. and H. H. Neumann, 1977. Application of the Priestley-Taylor evaporation model to assess the influence of soil moisture on the evaporation from a large weighing lysimeter and class A pan. *Boundary Layer Meteorol.* 12:243-256.
- Penman, H. L., 1948. Natural evaporation from open water, bare soil and grass. *Proc. Roy. Soc. London.* A193:120-145.
- Priestley, C. H. B. and R. J. Taylor, 1972. On the assessment of surface heat flux and evaporation using large-scale parameters. *Monthly Weather Rev.* 100(2):81-92.
- Shuttleworth, W. J. and I. R. Calder, 1979. Has the Priestley-Taylor equation any relevance to forest evaporation? *J. Appl. Meteorol.* 18:639-646.
- Stewart, R. B., 1983. A discussion of the relationships between the principal forms of the combination equation for estimating crop evaporation. *Agric. Meteorol.* 30:111-127.
- Stewart, R. B. and W. R. Rouse, 1977. Substantiation of the Priestley and Taylor parameter  $\alpha=1.26$  for potential evaporation in high latitudes. *J. Appl. Meteorol.* 16:649-650.
- Tanner, C. B. and W. A. Jury, 1976. Estimating evaporation and transpiration from a row crop during incomplete cover. *Agron. J.* 68:239-243.

Proc. 3rd Int'l Conf. Numerical Methods in Thermal  
Problems, 2-5 Aug 83, Seattle, R.W. Lewis, J.A. Johnson  
& W.P. Smith, eds.

Pitwridg Press

Swansea ~~England~~ <sup>UK</sup>

TJ260

E 575

IDENTIFICATION OF THE SOIL THERMAL DIFFUSIVITY FROM THE  
TEMPERATURE IN SITU MEASUREMENTS IN A SEMI-ARID REGION

M. FIRDAOUSS<sup>1</sup>, M. MAALEJ<sup>2</sup> and B. BELIN<sup>1</sup>

<sup>1</sup> LIMSI (CNRS) BP 30 91406 ORSAY CEDEX FRANCE

<sup>2</sup> IRST Campus Universitaire TUNIS TUNISIE

ABSTRACT

The purpose of this study is to predict the apparent thermal diffusivity of the soil from the temperature in situ measurements. It can be determined as a constant from an analytical approach based on Fourier analysis, or as varying with the soil temperature by a numerical identification. The results of numerical resolution of the heat diffusion equation utilizing different values of the diffusivity are compared to the observed temperatures. We note that the smaller differences are obtained when the diffusivity used for computations varies as a second order polynomial function of temperature. In all the cases the mean relative absolute difference doesn't exceed 0.33°C (1.14%). This confirms that the diffusion-based heat flow model gives quite acceptable simulations of the soil temperature.

INTRODUCTION

In the hot summer soil temperature becomes too high and this greatly affects the growth of roots of plants and micro-organisms living in the soil. The daily differences between maximum and minimum values of the soil temperature near the surface are about 30°C. Knowledge of the thermal and hydraulic characteristics of the soil plays an important role in the determination of the rate of evaporation of water, which is a rare element especially in arid regions. In this study we have taken into consideration the thermal characteristics related to this problem.

The temperatures of the natural soil in southern Tunisia had been measured at different depths below the surface and recorded at 3 min intervals during five different time period of a year. This soil is practically a homogeneous mixture of muddy sands down to a depth of 1 m. We show that the prediction of the thermal characteristics of the soil is possible from the

in situ measurements of the soil temperature either by an analytical approach based on Fourier analysis, or by a numerical identification on polynomial forms.

#### FOURIER ANALYSIS

The 1D heat conduction in the soil is modelled with the equation

$$\rho c(T) \frac{\partial T}{\partial t} = \frac{\partial}{\partial z} \left\{ \lambda(T) \frac{\partial T}{\partial z} \right\} \quad (1)$$

where:  $T$  is temperature in K,  $c$  is the specific heat capacity ( $J K^{-1} g^{-1}$ ),  $\rho$  is the density ( $g m^{-3}$ ),  $\lambda$  is the thermal conductivity ( $W m^{-1} K^{-1}$ ),  $z$  is depth (m),  $t$  is time (sec).

If we consider the variation with respect to the temperature of the heat capacity  $c(T)$  and thermal conductivity  $\lambda(T)$  negligible, and by introducing the thermal diffusivity  $a = \lambda/\rho c$  equation (1) can be rewritten as :

$$\frac{\partial T}{\partial t} = a \frac{\partial^2 T}{\partial z^2} \quad (2)$$

If we suppose that the boundary condition near the surface of the soil to be of the forme :

$$T(z_0, t) = T_a(z_0) + \sum_{k=1}^{\infty} A_k(z_0) \cdot \cos\{k\omega t - \phi_k(z_0)\} \quad (3)$$

and at the bottom as :

$$T \rightarrow T_{\infty} \text{ when } z \rightarrow \infty \quad (4)$$

The soil temperature can be approximated analytically in a Fourier series as below :

$$T(z, t) = T_a(z) + \sum_{k=1}^{\infty} A_k(z_0) \cdot \exp\{-(z-z_0)/D\} \cdot \cos\{k\omega t - (z-z_0)/D - \phi_k(z_0)\} \quad (5)$$

the constant  $D$  is called the damping depth. It is related to the thermal diffusivity of the soil and the frequency of the variations as follows :

$$D = \sqrt{2a/k\omega} \quad (6)$$

In Eq. 5,  $A_k(z) = A_k(z_0) \cdot \exp\{-(z-z_0)/D\}$  represents the amplitude of the soil temperature of an order of magnitude  $k$ , and  $\phi_k(z) = (z-z_0)/D + \phi_k(z_0)$  is the corresponding phase shift.

The table 1 presents the temperature amplitudes and phase shifts of the first and second order. The development is restricted to the second order because the amplitude of the third order are rather negligible. The decrease of the amplitude with depth and the increasing phase lag are typical for the propagation of the periodic temperature variation in a soil. At a depth  $z=16.2$  cm, the amplitude (first order) is 0.18 times the amplitude at  $z=1$ cm; it is only about 0.06  $A_1(z_0)$  at  $z=30$ cm.

This confirms that the diurnal variation does not penetrate below 50 cm.

z, cm	T <sub>a</sub> (z), °C	first order		second order	
		A <sub>1</sub> (z), °C	φ <sub>1</sub> (z), rd	A <sub>2</sub> (z), °C	φ <sub>2</sub> (z), rd
1.0	29.11	11.78	3.593	3.98	0.834
2.3	28.98	10.09	3.719	3.24	1.011
4.2	28.63	7.82	3.922	2.31	1.275
8.3	28.10	4.70	4.349	1.78	1.810
16.2	27.41	2.12	5.105	0.38	2.896
30.0	26.71	0.77	6.110	0.102	4.347
100.0	24.96	0.12	12.532	0.008	8.284

Table 1 : Values of the mean soil temperature, the amplitudes and the phase shifts of the first and second order, at different depths

The mean thermal diffusivity of the soil is obtained by a linear regression of the curves  $\text{Log}\{A_k(z)/A_k(z_0)\} = F(z)$  and  $\phi_k(z) - \phi_k(z_0) = G(z)$ . The diffusivities determined with respect to the amplitudes are :

$$a(A_1) = 10.492 \text{ cm}^2/\text{h} \text{ for the first order}$$

$$\text{and } a(A_2) = 11.181 \text{ cm}^2/\text{h} \text{ for the second order}$$

With respect to the phase shifts they are given by :

$$a(\phi_1) = 13.260 \text{ cm}^2/\text{h} \text{ for the first order}$$

$$\text{and } a(\phi_2) = 14.394 \text{ cm}^2/\text{h} \text{ for the second order}$$

The diffusivities are relatively the same whether they are calculated with the first or second order. But these values are rather different when calculated with the phase shifts and this is 25 % more important than that obtained from the amplitudes.

#### NUMERICAL SIMULATION

The direct problem (Eq. 2) is then solved numerically by an implicit scheme utilizing the values of diffusivity. The observed temperatures at the depth of 1 cm and 100 cm are taken respectively as the upper and the lower boundary conditions. The time step is taken to be 15 min and the space discretization is variable.

The results are compared to the observed temperatures as can be shown in the Figures 1 and 2 at depths of 2.3 cm, 4.2, 8.3, 16.2, and 30 cm. The differences are initially zero (at  $t=0\text{h}$ ), increase around noon, and decrease again after the soil temperature in a given depth reaches its maximum, and are negligible at the end of the cycle ( $t=24\text{h}$ ).

The effect of soil diffusivity used to solve numerically Eq. 2 is shown by comparisons between Figs. 1 and 2. The

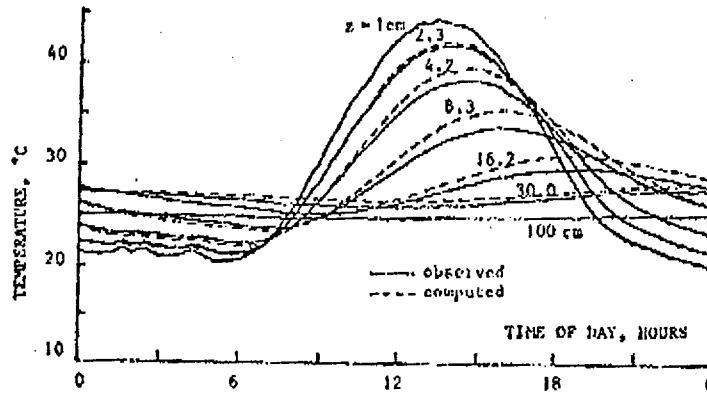


Figure 1 : Comparison of the observed soil temperature and the computed one using the diffusivity determined by the phase shifts

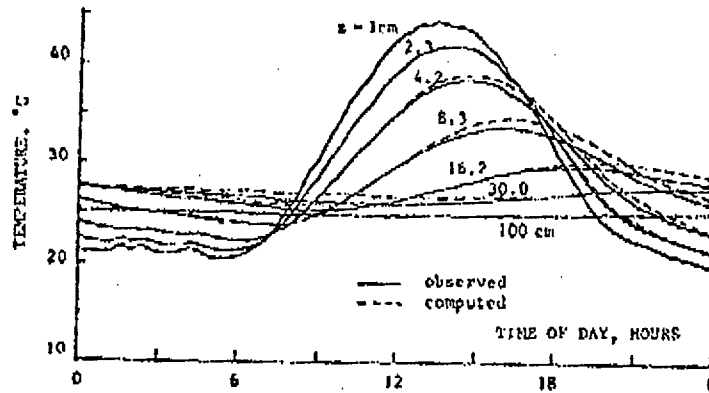


Figure 2 : Comparison of the observed soil temperature and the computed one using the diffusivity determined by the amplitudes

differences are quite smaller when the diffusivity is determined from the amplitudes ( $a=10.49\text{cm}^2/\text{h}$ ) than when it is determined from the phase shifts ( $a=13.26\text{cm}^2/\text{h}$ ).

In the table 2 are given the maximum values of the absolute differences between the observed and the computed soil temperature. The corresponding relative values (%), the absolute mean differences and their relative values are equally presented.

	maximum absolute difference	maximum relative difference	mean absolute difference	mean relative difference
$a(\phi_1)=13.26$	1.63 °C	4.87 %	0.330 °C	1.141 %
$a(A_1)=10.49$	1.08 °C	3.35 %	0.275 °C	0.982 %

Table 2 : Values of the maximum or mean, absolute or relative differences between the observed soil temperature and the computed one using the diffusivity determined by the phase shifts  $a(\phi_1)$  or by the amplitudes  $a(A_1)$

The mean relative differences are about 1 % and are of the same order as the experimental error induced by the thermocouples ( $\pm 0.5$  %).

#### NUMERICAL IDENTIFICATION

By minimizing the differences between experimental results and those obtained by numerical resolution of Eq. 1 it is possible to identify the apparent diffusivity of the soil knowing the thermal profiles at different instants of the cycle. The water content of the soil is supposed to be known, then it is possible to calculate at each instant the specific heat for different depths. This problem then leads to identification of the apparent thermal conductivity of the soil which can be determined from the following equation :

$$\rho \cdot c(z, t) \cdot \frac{\partial T}{\partial t} = \frac{\partial}{\partial z} \left\{ \lambda(T) \frac{\partial T}{\partial z} \right\} \quad (7)$$

and we search the value of  $\hat{\lambda}$  which minimizes the following function :

$$f(\hat{\lambda}) = \sum_n \left[ \sum_i \left| \frac{\{T_i^n(\hat{\lambda})\}^2 - \{T_i^n\}^2}{\{T_i^n\}^2} \right| \right] \quad (8)$$

where  $T_i^n$  is the experimental value of the soil temperature at any point  $z_i$  and at any instant  $t_n$  of the cycle,  $T_i^n(\hat{\lambda})$  is the temperature computed with  $\hat{\lambda}$  and corresponds to the same point.

Moreover, we assume that

$$\left| T_i^n(\hat{\lambda}) - T_i^n \right| \rightarrow 0 \quad \forall i, n \quad (9)$$

and  $\lambda_{\min} \leq \hat{\lambda}(T) \leq \lambda_{\max} \quad \forall T$  defined as  $T_{\min} \leq T \leq T_{\max}$

$\hat{\lambda}$  is expressed as a polynomial function of T as :

$$\hat{\lambda}(T) = \sum_i a_i T^{b_i} \quad (9)$$

The initial estimation of  $\hat{\lambda}$  is that obtained from the analytical solution. The numerical identification utilizes a sequential augmented lagrangian method. The minimization problem is solved by a newton method.

We show in figure 3 the variations of the apparent thermal diffusivity function of the temperature. These diffusivities are supposed to be of the form :  $a(T) = A + B \cdot T$ ,  $a(T) = A + B \cdot T + C \cdot T^2$ ,  $a(T) = A + B \cdot T^\alpha$ , values for  $20^\circ\text{C} \leq T \leq 44^\circ\text{C}$ . We note that the diffusivity determined by numerical identification as a constant is close to the value determined analytically from the amplitudes.

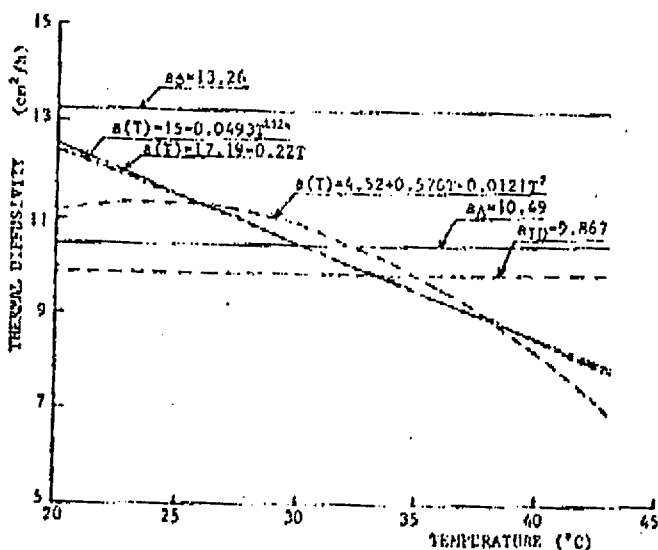


Figure 3 : Variation of the apparent thermal diffusivity of the soil as a function of the temperature

#### COMPARISON OF THE RESULTS

In figures 4, 5, 6, 7 the experimental results are compared at different depths to the results of numerical solution of the direct problem (Eq. 4) utilizing the diffusivity expressed by different polynomial forms. We note that the differences are the smaller when the diffusivity is assumed to vary with temperature. In this case appear successively under-estimations and over-estimations of the temperature when time increases. Remember that when the diffusivities are assumed to be constant (Figs. 1, 2, 4), the computed temperatures are always more important than the observed.

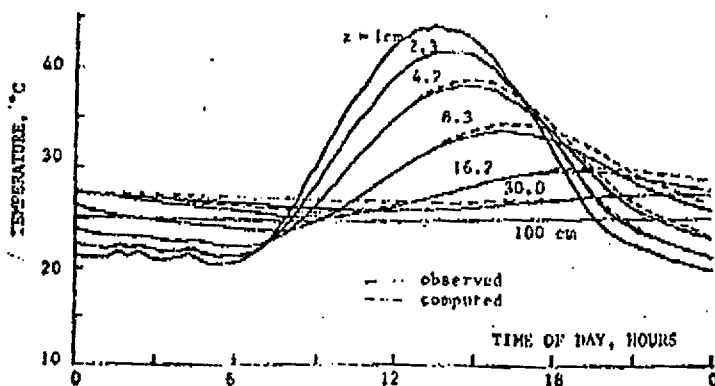


Figure 4 : Comparison of the observed soil temperature and the computed one using the diffusivity determined by numerical identification as a constant

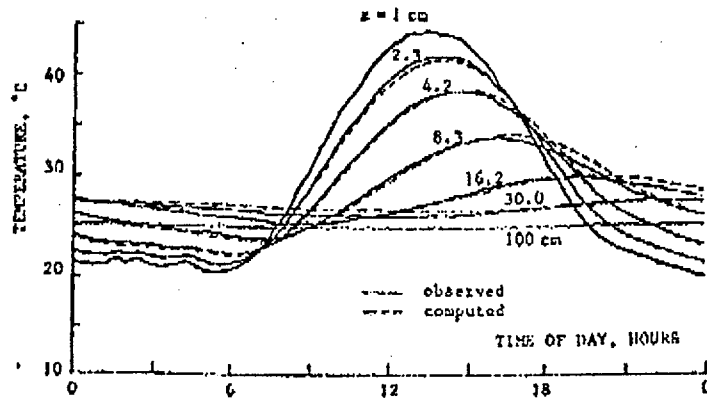


Figure 5 : Comparison of the observed soil temperature and the computed one using the diffusivity determined by numerical identification as :  $a(T) = A + B.T$

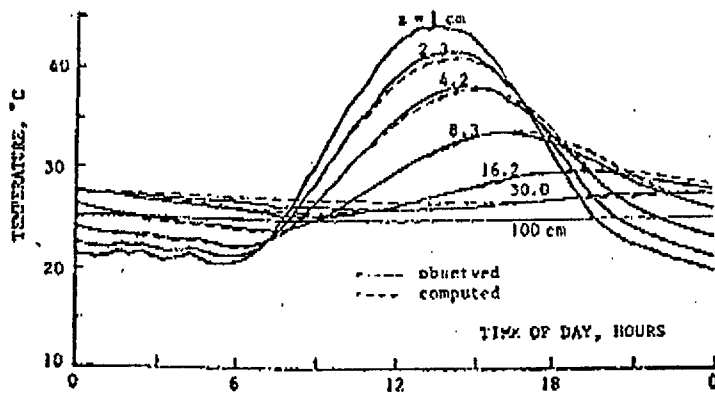


Figure 6 : Comparison of the observed soil temperature and the computed one using the diffusivity determined by numerical identification as :  $a(T) = A + B.T + C.T^2$

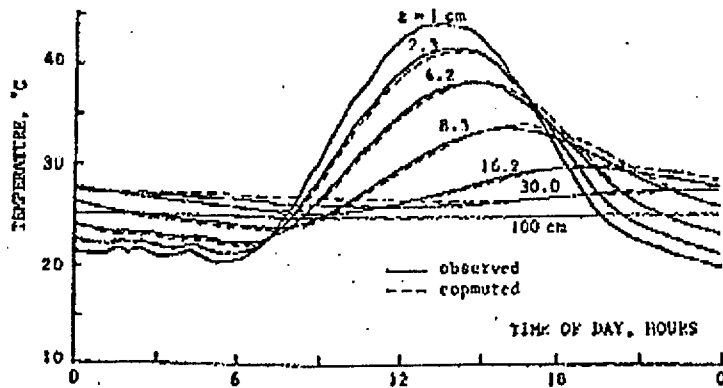


Figure 7 : Comparison of the observed soil temperature and the computed one using the diffusivity determined by numerical identification as :  $a(T) = A + B.T^n$

Finally we show in table 3, when the diffusivities are determined by numerical identification, the same differences as in table 2. One notes that the absolute mean difference obtained with the polynomial of the second order is  $0.22^{\circ}\text{C}$ , and is 1.5 times smaller than in case of diffusivity determined from the phase shifts ( $0.33^{\circ}\text{C}$ ).

	maximum absolute difference	maximum relative difference	mean absolute difference	mean relative difference
a = cte	1.09 $^{\circ}\text{C}$	3.47 %	0.281 $^{\circ}\text{C}$	1.01 %
a(T)=A+B.T	0.80 $^{\circ}\text{C}$	2.54 %	0.228 $^{\circ}\text{C}$	0.832 %
a(T)=A+B.T+C.T <sup>2</sup>	0.73 $^{\circ}\text{C}$	2.33 %	0.220 $^{\circ}\text{C}$	0.796 %
a(T)=A+B.T <sup><math>\alpha</math></sup>	0.79 $^{\circ}\text{C}$	2.53 %	0.227 $^{\circ}\text{C}$	0.828 %

Table 3 : Values of the maximum or mean, absolute or relative differences between the observed soil temperature and the computed one using the diffusivity determined by a numerical identification.

#### CONCLUSION

In the present work we propose a numerical method to identify the apparent thermal diffusivity of a soil from the experimental field temperature. The diffusivity can be determined either as a constant or varying with temperature. The differences between the observed and the computed temperatures are small, and are of the same order as the experimental error induced by the thermocouples.

The diffusivity which induces the smaller errors seems to be the second order polynomial as  $a(T)=4.52+0.576T-0.0121T^2$ . The mean absolute difference is in this case found to be  $0.22^{\circ}\text{C}$  and the absolute difference does not exceed  $0.7^{\circ}\text{C}$  in a maximum.

The proposed method was tested on one day cycle and will be applicated to other daily cycles. Now it seems possible that this analysis can be extended to other type of soils, which contains water and where the hydraulic non linearities will be preponderants.

#### REFERENCES

- W. R. VAN WIJK and D.A. DE VRIES - Periodic Temperature Variations in a Homogeneous Soil, Physics of Plant Environment, North Holland Pub. Co, AMSTERDAM, 1963
- M. FIRDAOUSS and M. MAALEJ - Measurement in situ and Numerical Simulation of Thermal Profiles in a Semi Arid Region, Heat Transfer 1982, Proceedings of the Seventh International Heat Transfer Conference - MUNCHEN - Fed. Rep. of Germany - 1982

FIELD MEASUREMENTS OF THE INFLUENCE OF ENTRAPPED AIR  
UPON PONDED INFILTRATION RATESJim Constantz and W.N. Herkelrath<sup>1</sup>

## ABSTRACT

Field experiments were designed to measure the effects of air entrapment in the transmission zone upon infiltration rates in two soils. Infiltration rates were measured using a double-cap infiltrometer, and soil water contents were measured using time-domain reflectometry (TDR). Carbon dioxide flooding was used to reduce the amount of air entrapment in half of the infiltration experiments. TDR measurements indicated that CO<sub>2</sub> in the pore space rapidly dissolved into infiltrating water, resulting in complete water-saturation of the transmission zone for experiments preceded by CO<sub>2</sub> flooding. For a gravelly loam soil as steady infiltration rates were approached, the average volumetric water content in the top 35 cm of soil, as measured by TDR, was 0.38 cm<sup>3</sup>cm<sup>-3</sup> for control experiments and 0.43 cm<sup>3</sup>cm<sup>-3</sup> for CO<sub>2</sub> experiments. The average steady infiltration rate was 0.42 cm min<sup>-1</sup> for the control experiments compared to 4.40 cm min<sup>-1</sup> for the CO<sub>2</sub> experiments. For a sandy loam soil as steady infiltration rates were approached, the average volumetric water content in the top 35 cm of soil was 0.43 cm<sup>3</sup>cm<sup>-3</sup> for control experiments compared to 0.45 cm<sup>3</sup>cm<sup>-3</sup> for CO<sub>2</sub> experiments. The average final infiltration rate was 0.07 cm min<sup>-1</sup> for the control experiments compared to 0.36 cm min<sup>-1</sup> for the CO<sub>2</sub> experiments. These results suggest that at least some air resided in open channels or conduits within the soil, reducing the effective hydraulic conductivity of the transmission zone well below the saturated hydraulic conductivity of the soil.

<sup>1</sup>Hydrologist and Physicist, respectively; U.S. Geological Survey,  
345 Middlefield Road, MS 496, Menlo Park, CA 94025 USA.

Researchers have known for more than half a century that air residing in the pore space of soils reduces infiltration rates (Powers, 1934; Horton, 1940). Soil air influences infiltration through four processes: 1) air displacement out of the transmission zone, 2) air compression below the transmission zone, 3) air solution-dissolution within the transmission zone, 4) and air entrapment or retention within the transmission zone. One or all of these processes can influence infiltration rates, depending on boundary conditions and soil properties. Numerous workers have shown that air displacement can effect infiltration rates (e.g., Morel-Seytoux, 1973). During infiltration, air is displaced downward in advance of the wetting front (Wilson and Luthin, 1963), and sometimes, air is displaced upward through the infiltrating water (Adrian and Franzini, 1966). Air compression is extremely important where an impervious layer or water table exists near the soil surface (Adrian and Franzini, 1966; Jarret and Fritton, 1978; Linden and Dixon, 1973; Dixon and Linden, 1972; and Breckenridge, Jarret, and Hoover, 1978). Air solution into infiltrating water has been shown to be important when infiltration continues for an extended period (Bianchi and Haskell, 1966). However, air entrapment or retention in the transmission zone always influences the rate of water entry into soils (Christiansen, 1944). During infiltration, air is entrapped or retained in the soil's transmission zone as downward flowing water circumvents regions in the air-filled pore space (Bond and Collis-George, 1981). Air retained in the pore space of the transmission zone reduces the volume of water which can enter the soil over a given time period. In this study, experiments are designed to minimize the influence of air displacement, compression, and solution upon infiltration rates, in order to isolate and measure the influence of air entrapment in the transmission zone upon infiltration.

A physically based infiltration equation is useful in predicting the effects of air in the transmission zone upon infiltration rates. Green and Ampt (1911) derived an equation to describe vertical downward movement of water in a soil under ponded conditions. Their equation is based on the assumptions that water travels down into the soil with a sharp wetting front and that the transmission zone above the wetting front has a uniform water content. If the depth of ponding is  $h$ , the Green and Ampt equation can be represented by the following expression:

$$\underline{I} = K(\theta_t)[(h - \psi_w)/z] + K(\theta_t) \quad (1)$$

where  $\underline{I}$  is the infiltration rate,  $K(\theta_t)$  is the effective hydraulic conductivity in the transmission zone,  $\psi_w$  is the matric potential at the wetting front, and  $z$  is the depth to the wetting front. Since  $K(\theta_t)$  depends strongly upon the volumetric water content of the transmission zone,  $\theta_t$ , the infiltration rate can be expected to be strongly influenced by entrapped air in the transmission zone. Furthermore, as  $z$  becomes large relative to the value for  $h - \psi_w$ ,  $\underline{I}$  approaches  $K(\theta_t)$ , and the influence of entrapped air upon  $K(\theta_t)$  can be estimated if the value of  $\theta_t$  is known.

Slack (1978) suggests that a soil has a fillable porosity available to infiltrating water, depending on the application rate and initial soil moisture conditions. This may imply that there is a single value for  $K(\theta_t)$  for a given infiltration event, but the value would vary somewhat for different situations. As a first approximation, he indicates that for most fine-textured agricultural soils, the volumetric water content of the

transmission zone,  $\theta_t$ , is about 90% of the saturated volumetric water content,  $\theta_s$ . Furthermore, the primary location of air within the pore space may strongly influence of the conductivity of the transmission zone. If air resides entirely in dead-end pore spaces, then  $K(\theta_t)$  remains close to the saturated hydraulic conductivity,  $K_s$ , of the soil. However, if air blocks channels which are continuous conduits for transmission of water deeper into the soil when filled with water, then  $K(\theta_t)$  is much less than  $K_s$ . Previous results indicate that  $K(\theta_t)$  is lower than  $K_s$  (Bower, 1966). Based on the limited data available which relates infiltration rates to hydraulic conductivities, Bower (1969) concluded that  $K(\theta_t)$  may range from  $.4K_s$  to  $.6K_s$ .

To reduce the amount of entrapped air during infiltration,  $CO_2$  has been injected into soils prior to tests.  $CO_2$  is readily soluble in water and a pretreatment of  $CO_2$  often results in complete saturation of the soil. In vented laboratory columns, Jarrett and Hoover (1985) reported at least a 50% increase in infiltration rates following  $CO_2$  injections. Stephens and others (1983a, 1983b) reported large increases in borehole infiltration and air-entry permeameter experiment after  $CO_2$  flooding. Furthermore, they found that infiltration rates, measured after  $CO_2$  flooding, corresponded well with predicted  $K_s$  values.

In the present study, the infiltration rate and the volumetric water content of the transmission zone were simultaneously measured during a series of ponded infiltration experiments in which a pretreatment of  $CO_2$  was used before half of the experiments. This was accomplished by using covered infiltrometers fitted with time-domain reflectometry probes for soil moisture content determinations. This experimental technique permitted:

- 1) measurements of the volume of air present in the transmission zone during infiltration,
- 2) measurements of the effect of this air upon infiltration rates, and
- 3) estimates of the reduction in the effective hydraulic conductivity due to air in the transmission zone.

#### EXPERIMENTAL EQUIPMENT AND PROCEDURE

A double-cap infiltrometer was used to measure the ponded infiltration rates at two field sites. A detailed description of the double-cap infiltrometer is given by Constantz (1983). Essentially, the double-cap infiltrometer (DCI) is a scaled down double-ring infiltrometer which has a permanent drive plate attached to the upper rims of two nested cylinders. The DCI is driven about 10cm into the soil and equal water heads are established in the inner and outer cylinders using constant-head reservoirs. If equal heads are carefully maintained, water flow below the outer cylinder inhibits radial flow from occurring below the inner cylinder. The cumulative outflow from the reservoir is recorded as a function of time in order to estimate infiltration rates and cumulative infiltration.

Time-domain reflectometry (TDR) was used to measure the volumetric water content in the soil beneath the inner cylinder of the DCI. A detailed description of TDR is given by Topp and others (1982). Briefly, TDR measures the apparent dielectric constant in the region between a pair of thin metal rods which have been inserted into the soil. The apparent dielectric constant can be related empirically to the soil's volumetric water content. In these experiments, a pair of 40cm long, 0.3cm diameter stainless steel rods, spaced

2.5cm apart, were driven 35cm into the soil at the center of each DCI. In this configuration, the TDR probe measured the average volumetric water content in the top 35 cm of soil. Figure 1 gives a cross-section of the DCI and TDR assembly with water ponding on the soil surface (the water supply reservoirs are not shown).

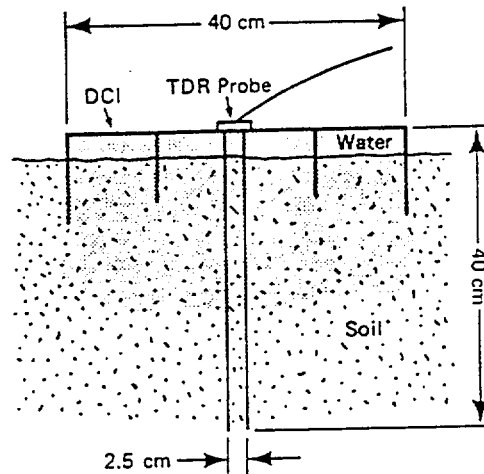


Figure 1. The double-cap infiltrometer (DCI) with the time domain reflectometry (TDR) probe inserted through the center of the inner cylinder.

Soil sites were chosen to avoid air compression during the ponded infiltration runs. Two soil sites were selected with well drained, highly porous structures which lacked any signs of erosion due to runoff. The water table was deep (>10m) and there were no impervious layers within 1m of the soil surface. The first site was located on Monte Bello Ridge in the Santa Cruz Mountain Range of Central California in a mature vineyard on Los Gatos Gravelly Loam. The soil at Site #1 is disced periodically, leaving the surface soil loose and free of vegetation. The second test site was located in the foothills to the east of Monte Bello Ridge supporting native oaks and mixed annual grasses. The soil at Site #2 is a Diablo Sandy Loam which contained desiccation cracks under a mat of dry grass at the initiation of tests. Table 1 gives several pertinent properties determined for both soils.

TABLE 1. SOME PERTINENT PROPERTIES OF THE SOILS AT EACH SITE

	Site #1	Site #2
Soil Series	Los Gatos	Diablo
Porosity	.43	.45
Gravel	18%	-
Sand	35%	62%
Silt	37%	20%
Clay	10%	18%
Class	gravelly loam	sandy loam

At both sites, two DCI units were driven about 10cm into the soil with approximately a 2m spacing between the units. To determine the effects of the TDR probes upon the infiltration rates, a preliminary infiltration experiment was run before inserting of the probes at each site. The DCI units were kept in place at the same location throughout each series of tests. Prior to each test, the soil was permitted to drain back to a specific moisture content within  $\pm 0.03 \text{ cm}^3 \text{ cm}^{-3}$ . Infiltration experiments were performed at about one week intervals, alternating between runs where a pretreatment of  $\text{CO}_2$  was used and runs where no pretreatment was used. The  $\text{CO}_2$  was injected through the inflow ports on the DCI (with the water manometers plugged) at 1.5 to 2.0 l/min for approximately 25 minutes. During experimental runs, the cumulative inflow into the inner cylinder was recorded after a constant ponding depth of 10 cm was established. The cumulative infiltration was calculated by subtracting the volume of water ponded in the inner cylinder from the cumulative inflow. The infiltration rate into the soil below the inner cylinder was recorded until a constant rate was approached or until the reservoir's water supply was exhausted. Tap water was used which had an electrical conductivity of .05 mmho of electrical conductivity, derived mainly from calcium, magnesium, and bicarbonate ions. Tap water was poured into the reservoirs a week before each test, to allow the gases in the water to equilibrate with the atmosphere prior to each infiltration run.

## RESULTS AND DISCUSSION

The use of any infiltrometer represents what has been called "fractional wetting infiltration" (Philip, 1983). Fractional wetting infiltration is simply the wetting of only a portion of the soil surfaces; it occurs in several natural and man-made situations (drip or furrow irrigation, for example). When fractional wetting infiltration occurs where no air-impermeable layer exists near the soil surface, the influence of air compression and air displacement are probably negligible compared to the influence of air entrapment. For these experiments, this contention is supported by two observations. First, during control runs (no  $\text{CO}_2$  treatment), air bubbles which were displaced vertically upward after ponding could be observed through the clear resin casing of the TDR probes. The volume of displaced air was small, amounting to no more than approximately  $5 \text{ cm}^3$  during the entire ponded infiltration period. Second, as  $\text{CO}_2$  was injected into the soil at 1.5 to 2.0  $\text{l min}^{-1}$ , the resulting back-pressure at the soil surface was only 2 to 3 cm of water pressure. These observations indicate that these soils are extremely permeable to gas flow and do not contain confining layers near the surface. This suggests that neither air displacement or compression